東海大学大学院平成 25 年度博士論文

Development of a New Strengthening Method in Short Glass Fiber Reinforced Polymer Composites

短ガラス繊維強化高分子複合体の強靭化に関する研究

Michael Christopher Faudree

ABSTRACT

In discontinuous short glass fiber reinforced polymer (SGFRP) and carbon fiber reinforced polymer (SCFRP) composites most data for unfilled FRP reports increasing fiber length increases tensile properties. However, in a highly-filled short fiber SGFRP-BMC (bulk molding compound) it has been found that decreasing fiber length to sub-millimeter can significantly increase fracture strength, strain and impact strength. Novel 'fiber end crazing' and 'fiber spacing' models for increasing tensile fracture stress and modulus as fiber length is decreased are constructed. The material under study in this dissertation is a highly-filled short glass fiber reinforced polymer (SGFRP) bulk molded compound (BMC) that is used for aerospace, automotive parts, housing for electrical wiring, and corrosion-resistant needs, hence mechanical property improvement is essential for durability and use life. The BMC is composed of a thermoset plastic resin with various inert fillers, fiber reinforcement, catalysts, stabilizers, and pigments that form a viscous paste for molding. Glass fiber reinforcement usually ranges from 5 to 30 mass% while glass fiber length ranges from about 3.2 to 12.7 mm (1/8 to 1/2 in). Fillers such as $CaCO_3$ can range from ~35 to over 50 mass%. Formulations are optimized for precise dimensional control, flame resistance, high dielectric strength, corrosion and stain resistance, and color stability. BMCs have excellent flow characteristics that make them well suited for parts requiring precise dimensions and detail. Compression and injection molding are commonly used for BMC as it can be easily produced with high productivity for mass production with a smooth and attractive surface finish. For compression molding large presses can accommodate large platen sizes making it ideal for large components. Further strengthening has always been expected to develop these lighter materials for higher durability and more efficient transports with small energy consumption for the environment. Therefore, this chapter is a literature search covering various effects on increasing the important tensile and impact mechanical properties including effect of fiber length, fiber volume fraction, toughness (of non-FRPs) by decreasing particle size, fiber spacing effects, fiber orientation effects, fiber end effects, cracking modes, fracture toughness and critical crack length. To make this dissertation well-rounded additional successful strengthening methods including increasing solidification texture angle and applying low-voltage electron beam irradiation to the SGFRP-BMC are also introduced. Prior to presenting the literature review is a preface concerning my research background.

<center>論文の内容の要旨</center>

論文題目「**Development of a New Strengthening Method in Short Glass Fiber Reinforced Polymer Composites** /短繊維強化高分子複合体の強靱化に関する研究」

<center>**Michael Christopher Faudree**</center>

キーワード：複合材、ガラス繊維、高分子、炭酸ｶﾙｼｳﾑ粉末、強靱化

　本研究では、ガラス短繊維、熱硬化性ﾎﾟﾘｴｽﾃﾙ/ｽﾁﾚﾝ-ﾌﾞﾀｼﾞｴﾝ、および炭酸カルシウム充填材の3相から構成される、ガラス繊維強化高分子（GFRP）の複合材料（GFRP-BMC）の強靱化について検討し、短尺繊維分散強化機構を明らかにした。第一の成果は集合組織短繊維配向角度の増加にともない GFRP-BMC の衝撃値の改良である。結果は第三章に記述した。第二の成果は、均一な低エネルギー電子線照射（HLEBI）処理が、GFRP-BMC の衝撃値をさらに向上させることを見出し、第四章に記述した。第三の成果は、添加する繊維の長さを、ｻﾌﾞﾐﾘﾒｰﾄﾙまでの短尺化することにより、GFRP-BMC の衝撃値、引張変形抵抗率（弾性係数）、破壊強度（引張強度）と、破壊歪が向上することであり、第五、六、七章で記述した。これは、破壊靱性値から計算出来る臨界ｸﾗｯｸ長より短い 0.44mm 長さの極短尺繊維の分散と、各繊維端で発生する圧縮応力の増加により説明でき、高分子複合材料において初めて公表された、本研究の最大の成果である。この結果の基づく短尺繊維分散強化機構を提案した。第 4 の成果は、射出成型した混合流体の数値ｼｭﾐﾚｰｼｮﾝである。GFRP-BMC の極短尺繊維配向集合組織の SEM 断面画像は、3 層（表皮-心-表皮）構造を示し、この計算と実験結果に良い相関関係を見出した。この結果から、機械的性質の再現性を高めるための製造条件に関する基礎的知見を得、第八章に記述した。

　第一章は序論で、研究背景と、寸法精度、難燃性、高絶縁性、耐食性、色彩安定性に合わせて成分配合を最適化した GFRP-BMC に関する概観を紹介し、本研究の目的を述べた。

　第二章は、GFRP-BMC 試料の作製と評価方法について述べた。試料の作製は、精密な寸法と円滑な表面仕上げで大量生産に用いられている射出圧縮成形を用いた。

　第三章は、集合組織の影響について述べた。試料切り出し前のﾏｻﾞｰﾊﾟﾈﾙ中央部は、配向角度がﾗﾝﾀﾞﾑ分布の凝固組織であり、外縁部よりﾊﾟﾈﾙ中央のｼｬﾙﾋﾟｰ衝撃値（a_{uc}）は著しく低い。そこで、短繊維の配向角度が異なる 4 種類の集合組織に分類したところ、GFRP-BMC 試料の配向角度が高いと衝撃値を高めることを見出した。さらに、これを三母数ﾜｲﾌﾞﾙ関数で計算し、下限衝撃値（a_s）を求めた。短繊維配向角度が 17.5°の試料に比較し、配向角度 68°の試料は、101%向上した。その結果、短繊維の配向角度が高い集合組織試料は、衝撃破壊抵抗が高いことを見出した。

　第四章は電子線照射（HLEBI）による GFRP-BMC 試料の衝撃値の向上について述べた。ﾏｻﾞｰﾊﾟﾈﾙ中央部は、外縁部より衝撃値が著しく低いが、中央部への HLEBI 処理により、5 から 25%程、a_{uc} を高めることを見出した。さらに、0.3MGy 照射した 45°配向集合組織試料の a_s は、未照射試料よりも約 64%向上することを明らかにした。ESR

の結果から HLEBI が高分子中の共有結合を切断することで、高分子内にﾀﾞﾝｸﾞﾘﾝｸﾞボンドを伴う終端原子を生成させ、圧縮サイトを形成することが主な強化機構である。さらに、高い衝撃値の試料では、単純な破壊から、2 次マイクロクラックの増殖や、主ｸﾗｯｸ付近の複雑な破壊機構への変換も、衝撃値向上に有効である。

　第五章は、繊維の短尺化も GFRP-BMC の衝撃値向上に寄与することを述べた。

　第六章において GFRP-BMC の弾性率の機構を説明した。この複合材料の弾性率は、ﾎﾟﾘｴｽﾃﾙ単独で2GPa、CaCO$_3$微粉末添加複合化で 4.5GPa まで向上し、市場で流通している 6.4 mm 長さの繊維による強化で 6.5GPa まで増加する。さらに、繊維長さを 0.44 mm まで短尺化すると 8 GPa まで付加的に向上することを見出した。応力―歪曲線から弾性率の指標となる変形抵抗率を求めたところ、この繊維長さの短尺化は、GFRP-BMC の初期変形抵抗率を 27%、最大変形抵抗率を 22%向上させた。これは、母材のﾎﾟﾘｴｽﾃﾙ樹脂の熱膨張係数(CTE)が、E ｶﾞﾗｽのそれより約 1 桁大きい為、成型凝固冷却時に繊維間隙の母材中に圧縮残留応力が生じ、母材分子密度が増大することによる。さらに、繊維短尺化による繊維/母材界面の面積増加が積算され、変形抵抗率向上が説明できる。

　第七章は、繊維長さの短尺化により、GFRP-BMC の引張破壊強度(σ_f)と、引張破壊歪(ε_f)の増加に関する成果である。0.44 mm 長の極短尺繊維を用いた GFRP-BMC のσ_fとε_fは、6.4mm 長の繊維試料と比べても、約 60 と 40%程度向上した。この短尺化は繊維端密度を高め、変形の際に繊維端における繊維/母材界面近傍における crazing 密度が増加する。crazing 領域はクラック伝播を抑制する圧縮場を保持する微小塑性変形と、臨界クラック長さ($0.50 < 2a_c < 5.0$ mm)以下の微小クラックを内在する。ここで、マイクロクラックが主クラック先端近傍で応力集中を抑制する理由を SEM 観察や超音波吸収の測定結果を用いて考察した。マイクロクラックが破壊エネルギーを吸収することにより、ﾏｲｸﾛｸﾗｯｸﾀﾌﾆﾝｸﾞ機構を発現する。臨界クラック長さ、繊維端の圧縮応力領域、ﾏｲｸﾛｸﾗｯｸﾀﾌﾆﾝｸﾞ、繊維の引抜き緩和効果の全てがクラック伝播を抑制し、GFRP-BMC の破壊歪の増加に寄与する可能性が高い。さらに、前章の変形抵抗率の増大も考慮すると、引張破壊強度向上や第五章の衝撃値向上も説明できる。

　第八章は、極短尺繊維、熱硬化性ﾎﾟﾘｴｽﾃﾙ/ｽﾁﾚﾝ-ﾌﾞﾀｼﾞｴﾝ、炭酸カルシウム充填材の混合流体の射出成型時における数値ｼｭﾐﾚｰｼｮﾝについて述べた。繊維集合組織の SEM 断面画像は、表皮-心-表皮の三層構造を示す。この結果と数値ｼｭﾐﾚｰｼｮﾝ結果は相関した。

　第九章は総括である。

Preface

My interest in science first started when my father bought me a telescope when I was 6 years old. We would go outside on a clear starry night, look through and gaze at the bright white topography of the Moon, details on the mysterious red surface of Mars and the faint stripes on Jupiter. Later in my junior year at university, I was lucky enough to have the adventure of being a summer intern at the NASA Kennedy Space Center in Florida working in the Chemical Analysis Laboratory. I worked with scanning electron microscopy and backscattered electrons to check there were no strange chemicals on space shuttle parts and satellites examined by the space shuttle. One day, we found silicon on a satellite and everyone was surprised, we thought it may be alien life. But we were calmed it was from sand in the blowing wind from the beach that got on the satellite before launch. On a tour for employees, we went inside the huge Vehicle Assembly Building where they built the Apollo rockets and space shuttle. We also had the great experiences of riding the elevator on the launch pad where the astronauts actually lifted off, visiting the launch pad where Apollo 11 lifted off, and greeting the astronauts as they came down the elevator in the Headquarters Building for space shuttle flights.

After graduating from a 5-year B.S./M.S program in Chemical Engineering/ Macromolecular Science at Case Western Reserve University I worked at General Dynamics, Fort Worth division. In my third year there, I had a surprising experience of a scientific discovery with composite materials of carbon fiber reinforced polymers (CFRPs) for high performance jet aircraft materials. I became project leader and soon it was known as the "Faudree Effect" by people in the industry. As a result, I wrote a publication [1.1] and the material was changed on the F-22 aircraft.

I have been interested in Japan since I met my father's friend and colleague, Mr. Kazunobu Miyatake of Noritake Company. I later obtained an MTESL (Master's in Teaching English as a Second Language) and applied for a teaching position here. I have been enjoying teaching English classes along with engineering and science classes. Since then, I have become acquainted with my advisor Professor Nishi, who is well-known and famous in a wide variety of polymer composite and metal fields. As our backgrounds are similar, I had the great and rewarding chance to conduct research in his laboratory with his students. Then I decided to pursue a Ph.D. since I have a very high interest in science. Sometimes in life, you never know what adventure is around the next corner.

To give details of the discovery with CFRPs, they are used for aircraft wingskins and other load bearing and non-load bearing parts and also for space and automobile parts. The CFRPs used on aircraft are composed of many plies of unidirectional tape of tiny (d = ~6 μm) carbon fibers impregnated in polymer matrix as shown in Figure 1.1. The matrix used was bismaleimide (BMI) which has higher aircraft and space operating temperatures than epoxy CFRP. This tape is cut then layed up in layers of different angles, called quasiisotropoic with symmetrical layup $[+25^o_4, 90^o_2]$ as shown in Fig. 1.1 followed by cure under vacuum by autoclave.

In my experiments, it was discovered that imide-linked resins in CFRPs can degrade under certain laboratory conditions involving the galvanic process [1.1], that "plastics can corrode" which up to that point had not been reported in the literature hence is has been called the "Faudree Effect". The discovery was made during solvent soak tests (Figure 1.2) on composite materials of carbon fiber reinforced polymers (CFRPs) used on the F-22 Raptor and other aircraft.
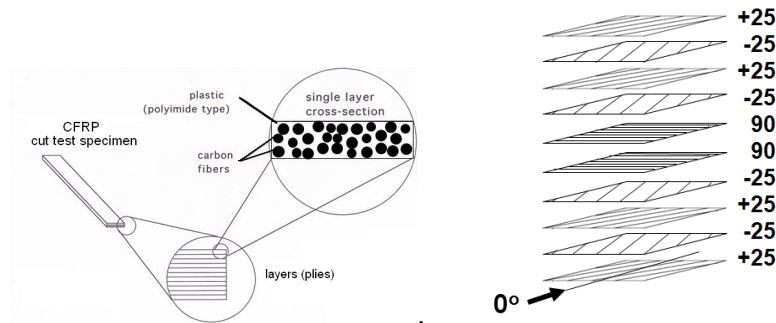
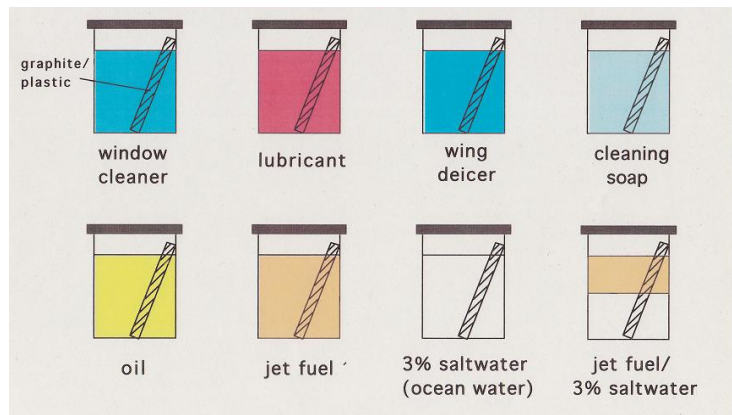**Fig. 1.1** Typical carbon fiber reinforced polymer (CFRP) composite used on aircraft.

Fig. 1.2 Graphite/bismaleimide CFRP (carbon fiber reinforced polymer):
22.9 x 25.4 x 1.35 mm specimens were immersed in different aircraft fluids.

One was an aircraft sump condition, a combination of 3% salt water (ocean water) and jet fuel illustrated in Figure 1.3. One gallon Fe/Sn cans were used as containers. After only 24 hr at 25 ^{o}C and 80°C conditions, there was resin loss with loose fibers. Degradation initiated at sample edges and bare graphite surfaces just above the salt water/jet fuel interface. Degradation was also found in the 3% salt water alone condition. The phenomena was found to occur in high temperature composites with an imide linkage including bismaleimides, triazines, condensation polyimides, thermoplastic polycyanates, high temperature PMR materials and their blends thereof.

Subsequent tests showed the BMI (bismaleimide) CFRP degradation occurrs by a galvanic process mechanism illustrated in Figure 1.4. The graphite fibers, which have a highly ordered crystal structure behave as an inert metal. When the graphite is in contact with aircraft aluminum both in salt water the CFRP corrosion occurs. Anode and cathode half reactions are shown in Fig. 1.4.
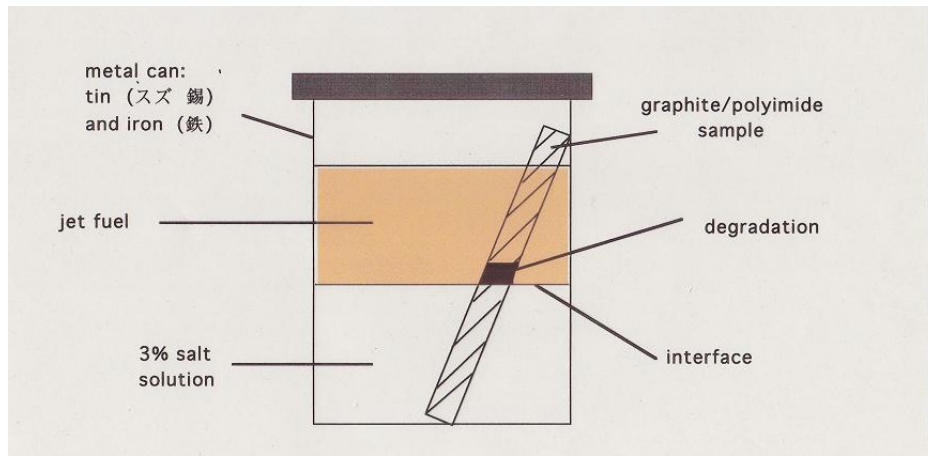
Fig. 1.3 Jet fuel/3% salt water immersion setup indicating degradation area as dissolved matrix and loose fibers after 24 hr at 25 and 80°C.
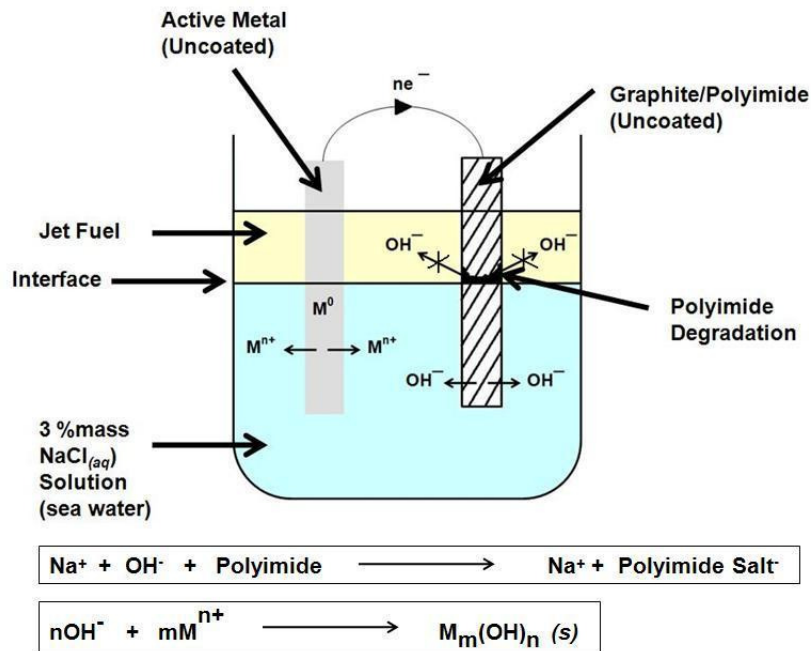

$$Na^+ + OH^- + Polyimide \longrightarrow Na^+ + Polyimide\ Salt^-$$

$$nOH^- + mM^{n+} \longrightarrow M_m(OH)_n\ (s)$$

Fig. 1.4 Jet fuel/3% salt water immersion setup showing degradation area after 24 hr at 25 and 80°C.

The high pH of the aqueous thin film that formed on the CFRP above the interface was ~13, hence OH- ions attacked the polyimide illustrated in Figures 1.4 and 1.5. These are unusually harsh conditions for aircraft since strict corrosion preventive measures such as coatings and glass scrim plies are used. However, setups according to aircraft specifications of anodized aluminum bolted to BMI-CFRP with titanium bolts covered by polysulfide sealant subjected to salt fog conditions and in jet fuel/3% salt water/80°C had polymer corrosion after 3000 hr after publication. However, examination of the F-16XL wings made of CFRP showed no damage in its service life. Since this is a concern for safety the BMI polymer was changed on the F-22 design. Now strict measures and inspection procedures are used to prevent this polyimide corrosion for maximum safety.

BMI Hydrolysis at O-C-N bond
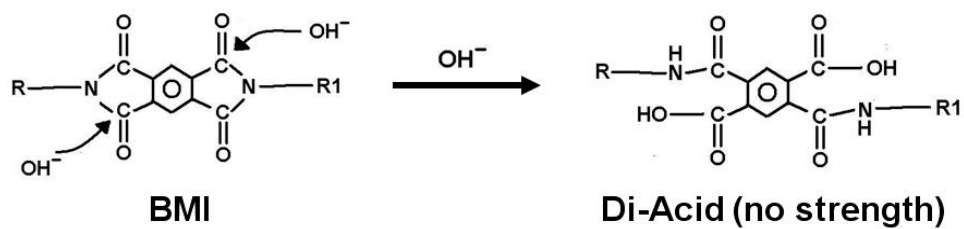
Fig. 1.5 BMI hydrolysis mechanism.

Outline

Ch. 1   Introduction

Ch. 2   Experimental

For short fiber glass fiber reinforced polymer (SGFRP) bulk molding compound (BMC) composite compression-molded panels, this dissertation focuses on:

Ch. 3   Increasing texture angle and decreasing texture angle range increases impact strength as well as the a_s at $P_f = 0$.

Ch. 4   Applying HLEBI (homogeneous low-voltage electron beam irradiation), increases impact strength in the weak center of the mother panels.

Ch. 5   Shortening fibers from commercial to sub-millimeter, increases impact strength a_{uc} at all panel solidification texture angles.

For SGFRP-BMC injection-molded specimens, this dissertation focuses on:

Ch. 6   A novel 'fiber spacing' model to describe shortening fibers from commercial 6.4 to sub-millimeter 0.44 mm increases tensile modulus.

Ch. 7   A novel 'fiber end crazing' model to describe shortening fibers from commercial 6.4 to sub-millimeter 0.44 mm increases tensile stress ~60% and its strain ~40%.

Ch. 8   To check feasibility of molding enhanced 0.44 mm paste, velocity profile in mold is obtained by fiber orientation agreeing closely with viscosity measurements.

Ch. 9   Conclusions

Acknowledgements

Table of Contents

Chapters

Chapter 1 Introduction

1.Introduction

1.1 Market and overview

According to a report by Visiongain the global GRFP composites market totals $29.4 billion (¥2,940,000,000,000 Japanese yen: $1 = 100 yen) [1.2]. They reported the enormous potential in Asian countries, particularly China and India, are likely to foster further growth in the GFRP market through the next ten years. Presently, the US and European countries are reported to be the leading regions for research and development of high performance glass fiber products while other countries are in the early stages of new product development.

Reinforcing polymers with particles has a long history and extensive literature has been written [1.3]. One main goal was to reduce cost by the addition of hard and cheap fillers. This would increase modulus but lower the toughness. Later, rubber particles were added to increase toughness, but this reduced the stiffness. Now of course, there are more rigid particle systems that have increased both toughness and stiffness such as glass or carbon fibers and fillers such as $CaCO_3$ along with novel hybrid composites of carbon and glass fiber together, carbon or glass fibers with metal fibers together, or the addition of carbon nanotubes. In addition, research is continuing on natural fibers and recycling GFRPs.

Always increasing mechanical properties is a goal for aerospace and other transport vehicles for low fuel consumption and concern for the environment, and daily articles. In addition, stronger material properties mean maximum possible safety which is always most important Next, effect of fiber length, fiber volume fraction, toughness of other composites by decreasing particle size, fiber spacing effects, fiber orientation effects, fiber end effects, cracking modes, fracture toughness and critical crack length will be covered.

1.2   Fiber length effects

Since assessing effect of l_f is difficult, most GFRP studies analyze the effect by numerical modeling. These numerical models usually predict that tensile strength and modulus increase, or have no effect with increasing fiber length. Most studies of fiber length in fiber reinforced composites report a decrease in properties such as tensile stress, strain, modulus and impact strength with decreasing fiber length. In a study of glass fiber lengths from 0.1 to 50 mm and 3 to 60 wt% Thomason and Vlug reported stiffness of glass reinforced polypropylene was reduced by shortening fibers below 0.5 mm and virtually independent of fiber length above 0.5 mm. They reported high concentrations of long fibers (>40 wt%) resulted in fiber packing problems with an increase in void formation which led to a reduction in modulus [1.4]. They also reported for glass reinforced polypropylene Charpy impact, tensile impact and high speed impact properties increased with fiber length up to 6 mm. Constructing a strain energy model, they reported an optimal length of 8 mm [1.5]. Fu and Lauke reported at small mean fiber lengths below the critical ~1.0 mm, 'fiber efficiency factor', a measure of tensile modulus and strength decreases rapidly with decreasing fiber length [1.6]. While in a model of a single fiber, Huang and Talreja predicted the same, at fiber lengths below the critical ~1.0 mm, tensile modulus and strength decreases rapidly with decreasing fiber length [1.7].

1.3   Fiber volume fraction effects

More common have been studies of effect of fiber volume fraction, V_f on mechanical properties in which the mechanical property increases to an optimum, then decreases with excess V_f. A study of the fracture behavior of polypropylene/glass fiber (GF/PP) composites focused on the effect of fiber–matrix interaction on stress distribution along fiber length. Results showed lowering glass fiber volume fractions in the GF/PP from 0.25 to 0.025, changes the variation of stress distribution along fiber length from trapezoidal to parabolic. They reported stress is concentrated at the fiber tips and leads the matrix to crazing [1.8].

As fiber volume fraction is increased in short fiber polypropylene GFRP and CFRP, tensile modulus is typically found to increase but tensile fracture stress and strain are decreased. Increasing V_f of the polypropylene GFRP from 0.08 to 0.25 increased tensile strength slightly from 49 to 51 MPa and tensile modulus from ~5.3 to ~8.5 GPa while fracture strain was reduced from ~0.75% to ~0.50% [1.9]. In short glass fiber polypropylene it was found composite stiffness increased linearly up to 40 wt% fiber. Fiber packing problems and an increase in void content resulted from high concentrations of long fibers up to 50 mm (>40 wt%) which led to a reduction in modulus [1.4]. In short glass fiber (l_f = 0.3 to 1.1 mm) reinforced polyamide 6,6 although volume fraction appeared to have little effect on observed average fiber orientation across specimen thickness ($\eta_{o,avg}$ = ~0.80, θ_{avg} = ~26.6 deg), tensile modulus was increased with volume fraction (given in wt%): 12➔ 20 ➔ 30➔ 40 ➔ 50 wt% yielding tensile mouli of ~6.5 ➔ 8 ➔ 10 ➔ 13.5 ➔ 17.5 GPa [1.10]. At 20 wt% this agrees with data for the l_f = 0.44 mm highly-filled SGFRP-BMC of this study. Other studies also predict increasing fiber volume fraction in FRPs from 0.15 to 0.30 approximately doubles fracture stress, while decreasing fracture strain about 20% [1.7].

1.4   Toughening of other composites by decreased particle size

This dissertation focuses on a new and novel finding in FRPs, that as fiber length is decreased tensile strength, and strain are increased. The toughening mechanism follows more to that in ceramics and metal-matrix composites, where as particle size is decreased, strength is increased. Figure 1.6 illustrates research for some ceramics and cemented carbide composites has shown for a given particle volume fraction, V_f as particles get smaller, strength is increased. Although in many ceramics the particle shape is different, being spherical or disc shaped, the principle is the same, that compressive stresses at increased dispersion points increase strength. This is shown in the 'fiber end crazing' model, where compressive residual stresses are generated at these points raising not only tensile strength, but also tensile strain.
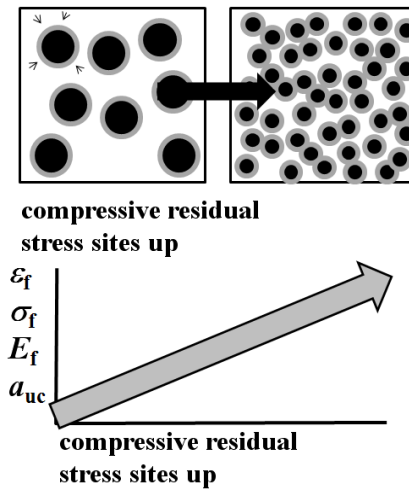
Fig. 1.6 Smaller particle size increases mechanical properties in some ceramics and metal matrix composites by increasing residual stress sites (grey areas) by CTE difference.

For example, smaller particle size accounted for higher strength in WC-Ni cemented carbide composites: strength was higher for fine WC particles of 0.5 μm as opposed to coarser 1.7 μm particles [1.11]. In Al_2O_3 dispersed ceramics, smaller disc particle size of 16μm diameter improved fracture stress 30% over 41μm diameter particles [1.12]. The researchers attributed the strength increase to residual stress increase by difference in coefficient of thermal expansion (CTE) between particles and matrix.
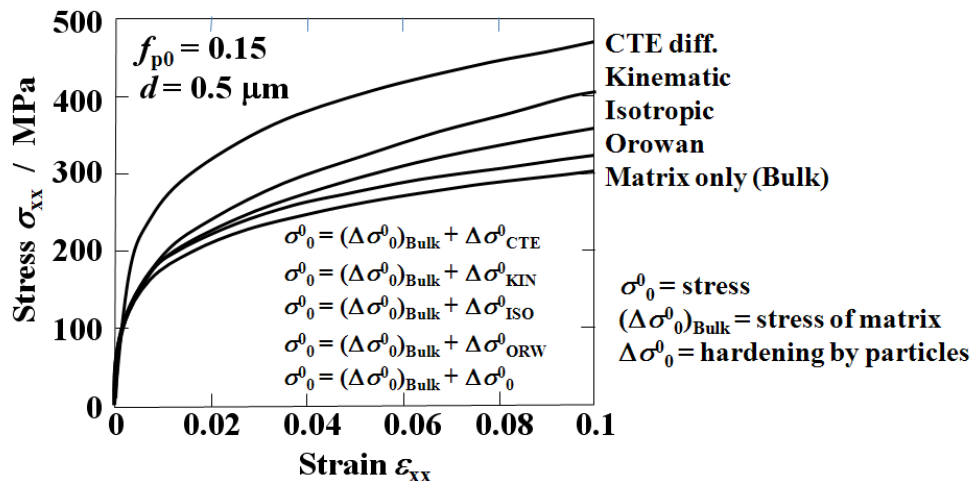
Adapted from Tohgo K., Itoh Y., Shimamura Y., Compos A, Appl Sci and Tech **41** (2009) 313-321.
Fig. 1.7 Contributions of strengthening mechanisms in reinforced composites [1.13].

Figure 1.7 shows a model of contributions of strengthening mechanisms in reinforced composites by Tohgo et al. [1.13] showing CTE difference between particle and matrix has most contribution to tensile properties, followed by Kinematic and Isotropic (effects of strain gradient plasticity related to geometrically necessary dislocations for heterogeneous dislocation around a particle), then Orowan stress for dislocation to pass through aligned particles. The model predicts tensile properties will increase with decreasing particle diameter. Since the CTE of the cured polyester resin

4

matrix (55 to 100 x $10^{-6}/^{o}K$) [1.14] is about an order of magnitude higher than that of E-glass fibers (5.4 x $10^{-6}/^{o}K$) [1.15], and fibers are observed to be generally aligned with the molding direction, it is hypothesized thermal residual stresses will be generated by the matrix on the increased fiber ends during molding, increasing the tensile and impact properties.

1.5   Fiber spacing effects

Recent fiber spacing studies of polymer composites are limited to computational modeling. The effect of inter-fiber spacing between fiber sides (not ends) on thermal residual stress and its effect on the transverse (bending) failure of unidirectional fiber composites has been modeled by finite element analysis (FEA). Yang et al. reported calculated residual stresses by FEA in general increase with increase of fiber volume fraction (50 to 60%) and decrease with minimal inter-fiber spacing. The residual stress is initiated by mismatch in coefficient of thermal expansion the matrix exerting stresses on the fibers during part cool-down and shrink. They reported matrix and interface damage may be induced during molding by the thermal residual stress, when the inter-fiber spacing between fiber sides is quite small [1.16]. For fiber spacing between fiber ends in a one-fiber thick planar array of fibers Sirivedin, S. et al. reported for epoxy CFRP the effect of fiber spacing on fiber fracture on the adjacent fibers: as fiber-spacing increases the effect on neighboring fibers is reduced while yielding of the matrix is increased [1.17].When modeling with a 3-dimensional hexagonal array 6 layers thick, FEA predicted the effect of fiber spacing on fiber fracture is less [1.18].

1.6   Fiber orientation effects

In injection molded thermosetting polyester molding compounds Corscadden et al. reported initial fiber orientation of random-in-plane (2-D) and unidirectional (1-D) reduces fiber breakage levels and significantly improves flexural and impact properties over that of the fully random (3-D) [1.19]. In injection molded polyamide 6,6 fiber orientation parameter is reported to be approximately independent of percent weight content from ~10 to 50%. [1.20].

1.7   Fiber end effects and crazing

For short fiber-reinforced polymers, stresses are known to concentrate at fiber ends. Tyson and Davies found interfacial shear stresses to be exceptionally high at fiber ends [1.21]. Lhymn and Shultz reported voiding, microcracking and crazing at fiber end sites during tensile deformation of injection-molded E-glass fiber ($d = 12$ μm) reinforced poly(ethylene terephthalate) [1.22]. Fracture mechanism at fiber ends depends on coupling agent. Samples of injection-molded short 6 mm, 20 and 30 mass% E-glass fiber reinforced polyvinyl chloride (PVC) were observed by SEM under 3-point bend by Yuan et al. [1.23] comparing well- and poorly-coupled systems. For the well-coupled, they found microcracks initiated at fiber ends when the composite was stressed. As strain level increased the cracks became more numerous in the region of maximum stress. As strain was increased further, the cracks propagated straight into the matrix. These cracks either joined other cracks at nearby fiber ends or interacted with other fibers resulting in interfacial debonding along the fiber lengths. They found numerous elongated fibrils near the fiber ends approximately 0.1 μm in

diameter about the same size as craze fibrils found in fatigue tests of the PVC [1.24]. For poorly-coupled E-glass PVC, Yuan et al. found cracks also initiated at fiber ends. At high strains, however, the cracks propagated from the fiber ends along the length interface with no propagation into the matrix as in the well-coupled system. Yuan et al. attributed it to stress reduction at the fiber end crack tips by the coupling [1.23]. Choi and Takahasi reported fracture processes of short fiber thermoplastic composites involve microcracking, microvoiding, shear-band formation and/or crazing in the matrix or interface [1.25]. Four-point bend tests of glass fiber reinforced polypropylene shown a damage zone ahead of the precrack containing crazing initiated from the glass fibers. The crazes were propagated by moving towards the interface followed by craze thickening and fiber breakage [1.26].

For injection-molded short fiber reinforced thermoplastic composite, an approximate stress analysis was performed to evaluate the microfracture behavior near a fiber end   the calculated stresses are used to explain the damage initiation and growth behavior with different fiber surface treatments [1.27]. A model of the stress state at fiber ends in short fiber polymer and metal matrix composites was constructed. The model was developed from the elasticity solution of a concentric cylinder assemblage, along with an approximate solution to the classical shear-lag problem and takes into account fiber orientations, length and types of fibers [1.28]. Starink derived a shear lag model of stress transfer between fibers and matrix based on cylindrical geometry whose predictions were found to agree well with metal matrix composites of fibers of different aspect ratios. The equations employed hyperbolic tangent (tanh) and secant   (sech) for shear lag that modeled behavior that increasing fiber aspect ratio increases Young's modulus [1.14]. A model employing shear lag was reported to predict the point-wise stresses in the fiber and the matrix and the stress state at fiber ends [1.14].
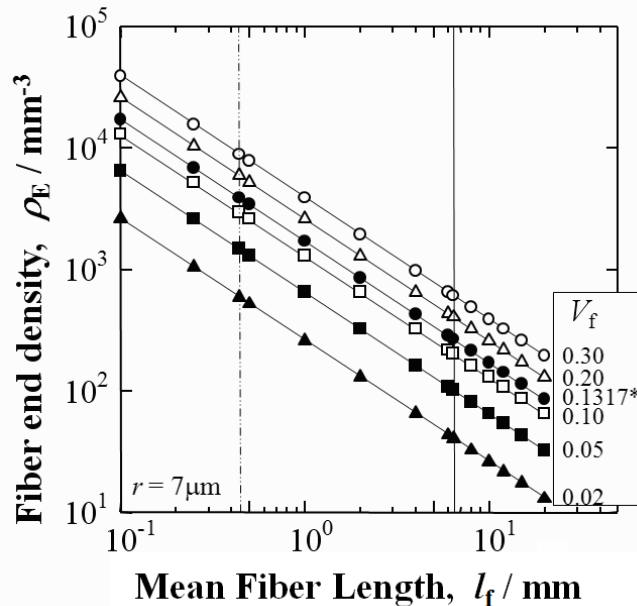
Fig. 1.8 Calculated fiber end density, ρ_E vs. fiber length, l_f for a 7 μm-radius glass fiber composite showing different volume fractions, V_f. The plot for the 20 wt.% glass fiber BMC ($V_f = 0.1317$) is indicated. Fiber lengths $l_f = 6.4$ mm (solid line) and shortened 0.44 mm (dotted line) are shown.

6

Figure 1.8 shows substantial proliferation in fiber end density, ρ_E as fiber length, l_f is shortened by eq. (1.1):

$$\rho_E = 2V_f/\pi r^2 l_f \qquad (1.1)$$

Depicted in Fig. 1.8 at $V_f = 0.1317$ when l_f is decreased from commercial 6.4 mm to submillimeter 0.44 mm, ρ_f is increased over an order of magnitude from 267 to 3888 mm^{-3} [1.29]. By shortening the fibers to sub-millimeter length, the resulting higher fiber end density, ρ_f may act to increase relaxation sites impeding crack growth above the critical length, $2a_c$.

1.8 Cracking modes (Mode I, II, III)

Mode I	Mode II	Mode III
tension, opening	shear, sliding	shear, tearing
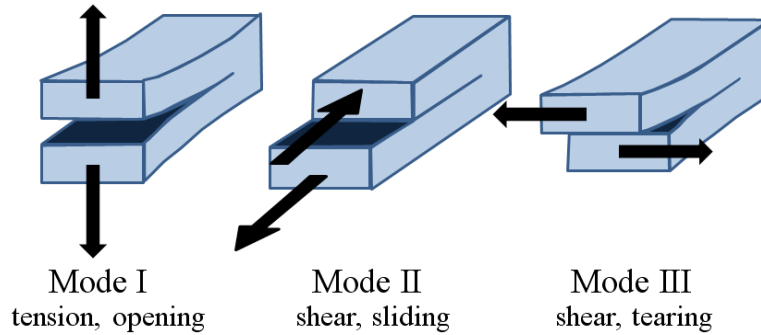
Fig. 1.9 Cracking modes.

However, as depicted in Figure 1.9 a crack occurs in 3 dimensions and occurs in three modes: Mode I (tension, opening), Mode II (shear, sliding) and Mode III (shear, tearing). It is predicted that the critical crack length, $2a_c$ (mm) is between 0.44 and 3.2 mm in the BMC. Since the fibers have been observed to be mostly aligned with the injection molding direction, the BMC is approximated as orthotropic. Williams has reported even if there is a mixed-mode or pure Mode II stress field at the crack tip, the crack propagates such that Mode I dominates at the subsequent crack front in isotropic materials [1.30]. This is also true for injection molded composites where microcracks and the main crack tend to form perpendicular to the loading direction, σ_{11} [1.23, 1.31]. Based on the fracture toughness and tensile strength of the matrix, the critical crack size of the matrix is estimated using Mode I loading in eq. (1.2): [1.32].

$$K_{IC} = \sigma_y (2\pi a)^{0.5} \qquad (1.2)$$

where K_{IC} is fracture toughness (MPam$^{1/2}$), σ_y is assumed to be the yield stress of plastic deformation of the matrix (MPa) and a (m) is the critical crack radius for propagation calculated in eq. (1.3): [1.32].

$$2a = \pi^{-1}(K_{IC}/\sigma_y)^2 \qquad (1.3)$$

Injection-molded glass fiber PET displayed a 3-layer [skin-core-skin] fiber orientation structure across the thickness. In notched tensile specimens, it was reported that approximately 75% of the cross sections of the fibers lie across the crack paths; only in the disoriented core was there easy crack propagation since fibers are parallel to the Mode I crack direction [1.33]. In injection-molded short glass fiber polypropylene

(SGFRP) subjected to notched Charpy impact tests, it was concluded that the matrix fails by crazing [1.34]. Craze initiation stress in polystyrene was found to increase with aligned molecular orientation in the polymer produced by uniaxial melt drawing [1.35].

1.9 Fracture toughness, K_{IC} and critical crack length, $2a_c$
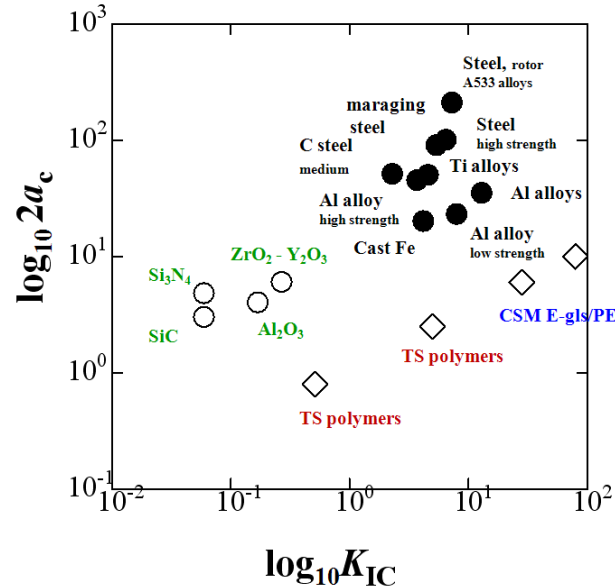
Fig. 1.10 Log10-Log10 plot of $2a_c$ vs. K_{IC} values from the literature.

From data in the literature, Figure 1.10 was constructed of logarithmic values of $2a_c$ vs. K_{IC}. Various metals and their alloys are grouped together in the upper right. In addition, ceramics and polymers, respectively, are grouped together. Glass fiber reinforced chopped strand mat (CSM) polyester with approx. 50 mm E-glass fiber length has higher performance than cured thermoset polymer resins alone.

K_{IC} for ceramics SiC, Al_2O_3, Si_3N_4, and ZrO_2-Y_2O_3 are reported to be 3.0, 4.0, 4.8, and 6.0 MPam$^{1/2}$, respectively, marking their brittle nature. On the other hand, cast iron, Al alloy, Ti alloy, and maraging steel are considerably higher at 20, 35, 50, and 90 MPam$^{1/2}$ [1.36]. K_{IC} for chopped strand mat (CSM) E-glass/polyester (no filler, fiber length approx. 50 mm) is reported to be between these ceramics and metals at approximately 6-10 MPam$^{1/2}$ [1.37].

As for critical crack lengths ($2a_c$), Si_3N_4, SiC, Al_2O_3, and ZrO_2-Y_2O_3 ceramics, are reported as 0.06, 0.06, 0.17, and 0.27 mm, respectively. The cast iron, Ti alloy, maraging steel, and Al alloy are listed as 4.2, 4.6, 5.4, and 13.0 mm [1.36]. The critical crack length $2a_c$ range for thermoset polymers was calculated to be approximately $0.50 < 2a_c < 5.0$ mm, from K_{IC} values in the literature [1.38-1.39].

1.10 Effect of homogeneous low-voltage electron beam irradiation (HLEBI)

Applying homogeneous low voltage electron beam irradiation (HLEBI) has been found to enhance long-fiber GFRPs, glasses such as silica glass, glass fibers, and a wide range of polymers [1.29, 1.40-1.45]. For GFRP with long fibers used for next-generation aircraft, HLEBI has been used to improve Charpy impact value at all fracture probabilities [1.41]. HLEBI often enhances the deformation resistivity

8

(elasticity) of polymer [1.40]. Moreover, HLEBI often induces not only hardening, high wear resistance and sterilization for practical use of polymer, but also mist resistance of transparent ceramics [1.46-1.48]. Furthermore, it is also possible to enhance the interfacial strength induced by surface activation, which is generated by charging and dangling bond formation.

Based on the radial distribution function (RDF) of silica glass, it has been found HLEBI reduces the normalized coordination number N_D/N_O, and raises the normalized mean atomic distance r_D/r_O resulting in volume expansion [1.45]. Therefore, compressive stress has been confirmed in the silica glass. Repulsive force occurs between the outer shell electrons, probably inducing compressive stress and stress relaxation similar to the role of a cushion. Therefore the effects of HLEBI on hardening, elasticity, ductility enhancements, and strengthening of ceramics, polymers and their composites can be expected.

The previous research on HLEBI has been conducted on relatively ordered one- or two- phase systems of polymers, fibers, and long-fiber reinforced polymer GFRPs and CFRPs [1.42-1.45]. This research investigates Charpy impact of a three-phase system of compression- molded short-fiber GFRP-BMC panels containing a high percentage (55 mass%) of $CaCO_3$ filler that undergoes complex flow patterns.

1.10.1 Mechanism of action of HLEBI

(a)Rational formula of thermoset polyester   (b)Rational formula of styrene-butadiene

_____

(d) styrene-butadiene showing bond dissociation energies
(c) thermoset polyester showing bond dissociation energies
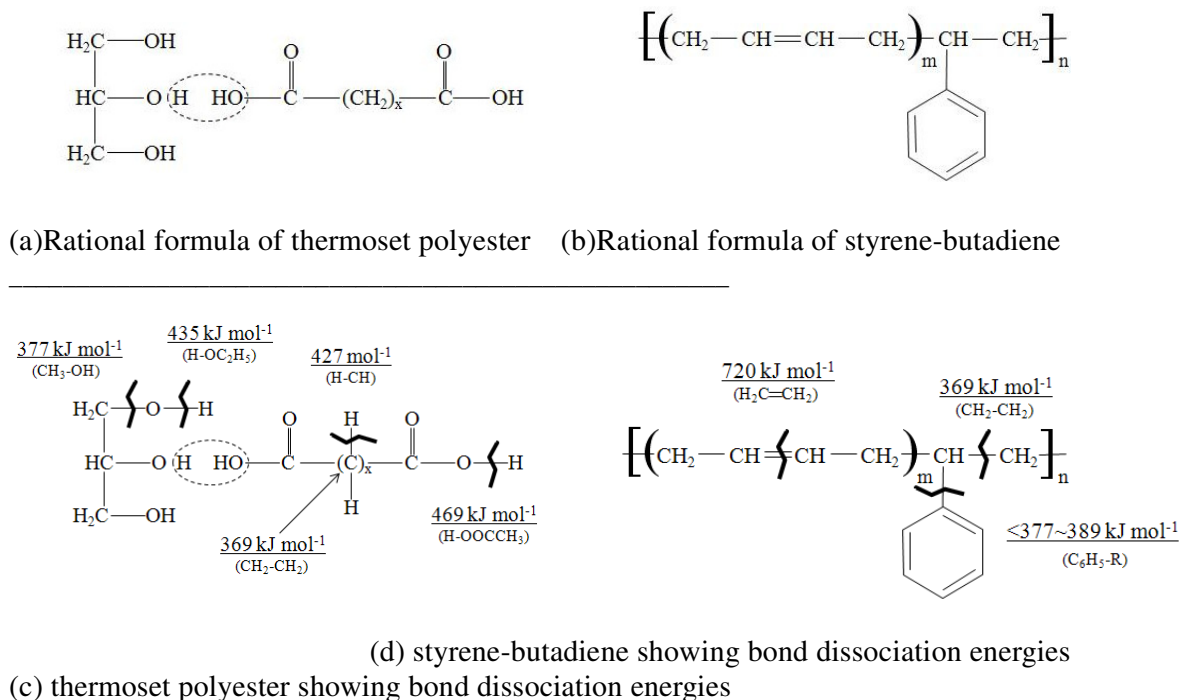
Fig. 1.11 Schematic illustration of thermoset polyester and styrene-butadiene co-polymer, respectively, before (a), (b) and after (c), (d) electron beam irradiation showing approximate bond dissociation energies and dangling bond locations [1.49-1.50].

Figure 1.11 shows the rational formulae of thermoset polyester and styrene-butadiene co-polymer, before (a), (b) and after (c), (d) HLEBI irradiation. HLEBI generally cuts the atomic bonding at weak chemical bonding sites and dangling

bonds are formed at the terminated atoms with low dissociation energy [1.42-1.44]: at methylene groups (CH_2–CH_2: 369 kJmol^{-1}), hydroxyl groups (CH_3–OH: 377 kJmol^{-1}), phenyl groups (C_6H_5–R: <377~389 kJmol^{-1} where R- is CH_3- or C_2H_5-), and free-radical hydrogens (H–CH: 427 kJmol^{-1}, H–OC_2H_5: 435 kJmol^{-1}, and H–$OOCCH_3$: 469 kJmol^{-1}), and alkene groups $H_2C=CH_2$ with the higher dissociation energy at 720 kJmol^{-1} [1.49-1.50].

Given these conditions, it is important to strengthen parts such as electrical housing that can be exposed to outside environments to withstand possible impacts and maintain long use life.

Up to now, there has been no or little research on improving mechanical properties by HLEBI of short-fiber GFRP. However, since HLEBI has been found to enhance the long-fiber GFRPs, glasses such as silica glass, glass fibers, and a wide range of polymers [1.40-1.45], it is predicted that HLEBI can enhance the Charpy impact strength 5 to 25% in the weak center region of the compression-molded BMC GFRP mother panels constructed with short glass fibers, $CaCO_3$ filler, and unsaturated polyester/ styrene- butadiene block copolymer.

1.11 Charpy Impact Test: Importance for aircraft

Impact strength of GFRP-BMC is important for durability of daily articles exposed to the environment, such as space and transport machines, construction materials, boxes for electrical wiring, and aircraft parts. Typically, to screen aircraft materials such as long-fiber quasiisotropic laminates and weaves for resistance against birdstrike, hailstone, or volcanic rock, damage by a hemispherical impactor (Figure 1.12) is initiated as a point force on the center of a square or rectangular specimen ~70 to 150 mm^2 by slow point
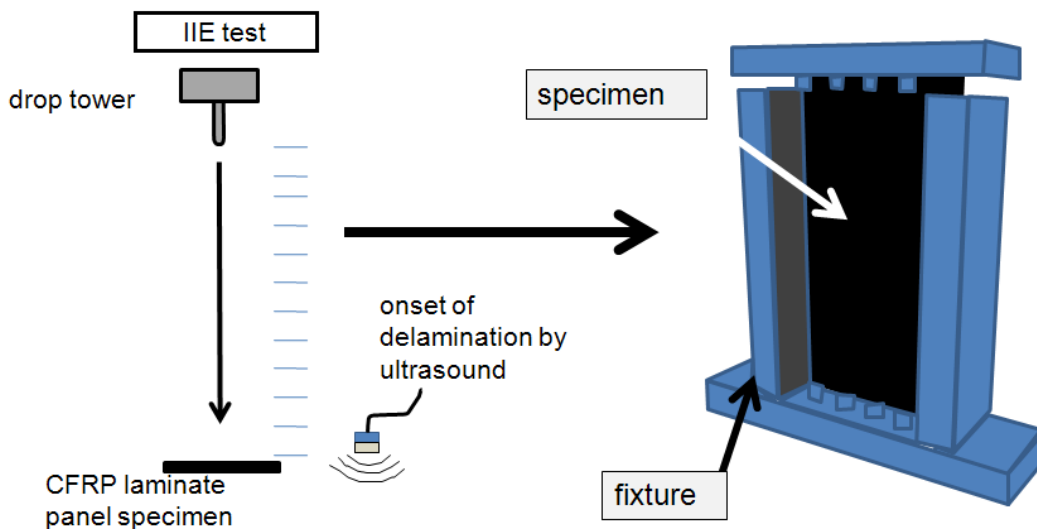
Fig. 1.12 Incipient impact energy (IIE) and compression after impact (CAI) tests.

force [1.51], drop tower, or projectile [1.52-1.54]. Initiation of damage in the form of delamination is usually assessed by non-destructive evaluation (NDE) such as an ultrasonic sensor. This is usually followed by compression after impact (CAI) tests to compare integrity and safety level of candidate materials after impact. However, the material under investigation is a non-laminate short-fiber GFRP. Therefore, we employ Charpy impact test which utilizes a drop-weight pendulum and evaluates the impact

absorption characteristics and relative impact toughness of materials often used in quality control applications employed as an inexpensive and fast way to estimate reaction to higher velocity impact. We do not claim the Charpy impact test to be a replacement for point–force tests followed by CAI. But we assert Charpy impact may be used as a preliminary method to screen for candidate materials for later evaluation by projectile and CAI.

1.12 Enhancement of tensile modulus by shortening fibers

Tensile modulus is one of the important properties for high performance and depends on the fiber volume fraction, length, orientation, and strength of coupling agent between fiber and matrix.

Up to now, the literature has reported that lengthening fibers increases tensile modulus in fiber reinforced composites [1.20, 1.57-1.64]. On the other hand, this work presents a new finding that tensile modulus is increased in a highly-filled GFRP-BMC by shortening fibers from commercial 6.4 mm to 0.44 mm, in which most of the population is below the critical length of ~1.0 mm.

1.12.1   The 'fiber spacing' model

A novel 'fiber spacing' model not previously reported in the literature is therefore constructed on the basis that the increased spacing between fibers, S_f acts as sites for action of thermal residual compressive stresses during part cool-down and shrink. Thermal residual stresses are expected to have a significant influence on mechanical properties when the CTE in the matrix is different than the dispersed particles [1.58]. CTE of typical E-glass fibers is reported to be 5.4 x 10^{-6}/K from 243 to 523 K (-30 to 250°C) [1.15], about an order of magnitude lower than that of cured polyester neat resin at 55 to 100 x 10^{-6}/ ^{o}K [1.14]. During cool-down the matrix will therefore contract more than the fibers creating compressive residual stresses on the fibers in all directions. Moreover, when fibers are in close proximity to each other thermal residual stresses reach a maximum as shown by Dragoi et al. for metal matrix composites [1.58].

1.12.2   Shear-lag models

Alternatively, there are many studies of fiber reinforced composites where lengthening fibers increases tensile modulus. They usually incorporate a 'shear lag' parameter for stress transfer efficiency between fiber and matrix [1.4, 1.11, 1.55, 1.56, 1.57]. 'Shear lag' models for tensile modulus incorporate a 'rule of mixtures' with an orientation parameter such as Hermans (η_o) accompanying the 'shear lag' factor (η_l), [1.4, 1.11, 1.55, 1.56, 1.57] for example eq. (1.4) [1.56]:

$$E_c = \eta_o \eta_l V_f E_f + (1 - V_f)E_m \qquad\qquad (1.4)$$

where E_c, V_f, E_f, and E_m are modulus of composite, fiber volume fraction, fiber and matrix modulus, respectively.
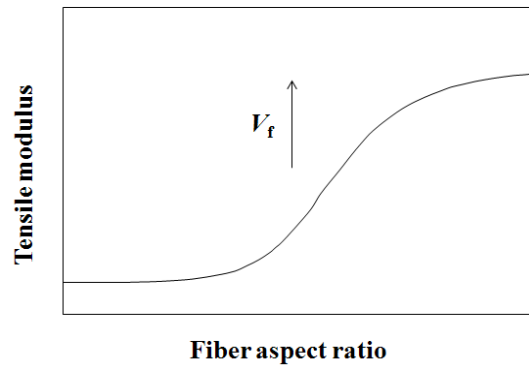
Fig. 1.13 Prevailing shear-lag models for 2-phase polymer-fiber systems modeled by a hyperbolic tangent or secant.

Shear-lag parameters are typically modeled as a hyperbolic tangent-shaped curve increasing with volume fraction, V_f where modulus increases with fiber aspect ratio leveling off at low and high aspect ratios is shown in Figure 1.13 [1.14, 1.20, 1.11, 1.55, 1.59]. The Tsai-Halpin model has been applied to variety of reinforcement geometries from a sphere to a long filament predicting stiffness increases with aspect ratio and employs shear-lag factors where increasing the fiber length increases modulus [1.59]. However, shear-lag models are reported to cover 2-phase systems of fiber and matrix [1.11, 1.55, 1.59].

1.12.3 Fiber orientation
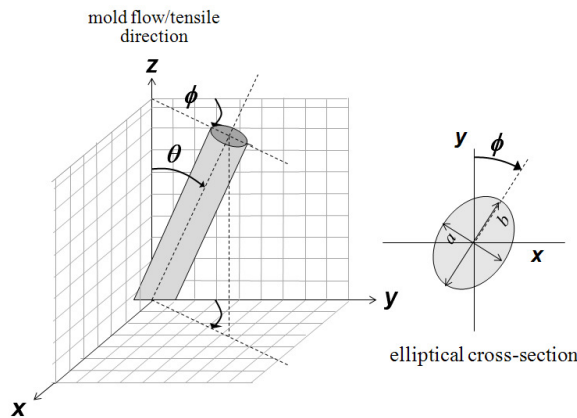
Fig. 1.14 Fiber orientation in 3 dimensions and elliptical cross section to measure fiber angle, θ with respect to molding/tensile direction.

Modulus also depends on fiber orientations. The influence of fiber orientation on mechanical properties of 2-phase polymer-fiber systems has been well reported [1.4, 1.10, 1.14, 1.55, 1.58, 1.60, 1.61]. When fiber cross-section elliptical shapes with respect to molding/tensile direction are assigned 'a' and 'b' for their short and long axes, respectively fiber orientations, θ (deg) are obtained as illustrated in Figure 1.14 [1.62, 1.63].

$$\theta = \arccos(a/b) \tag{1.5}$$

This is assuming circular fiber cross sections. Fiber orientation parameter is thus calculated as [1.55]:

$$\eta_o = [\cos^2(\theta)] = (a/b)^2 \tag{1.6}$$

and measured for fibers across the BMC thickness.

1.12.4   Fiber orientation distributions in molded polymer composites

There have been many studies of fiber orientations relating to flow in molded polymer composites in the past few decades. Recently, Thomason investigated effects of fiber orientation, length, diameter, and strength on tensile and flexural properties [1.20]; and effect of fiber orientation on tensile modulus of injection-molded short-fiber polyamide 6,6 agreeing closely with the predictive 'shear lag' models by Cox [1.55] and Krenchel [1.56].   The fiber flow pattern was 5-layered across specimen thickness [skin- shell- core- shell- skin] consisting of highly random thin skins about 4% of sample thickness with relatively thick highly oriented shell layers surrounding an inner core with near random in-plane fiber orientation. Akay and Barkley correlated longitudinal and transverse fiber flow orientations with tensile and dynamic mechanical and fracture properties [1.64].
 Taking cross sections parallel to the flow line at various depths, they found a 3- layer [skin-core-skin] fiber flow pattern appearing to transition into 5-layers with depth. The BMC also exhibits a 3-layered [skin-core-skin] fiber flow pattern with highly oriented skins ~4-8% of the thickness surrounding a parabolic-shaped core with fiber angles, θ = 40-90 degrees from the molding/tensile direction resembling classical laminar flow through a conduit. Deviations from the parabolic flow were due to fiber density gradients [1.65]. In the BMC, average θ across specimen thickness was 44 deg. In injection-molded polymer composites, core thickness has been found to increase with injection speed, melt and mold temperatures [1.64]. A novel 'fiber spacing' model is therefore constructed which predicts effect of fiber length (l_f), diameter (d), fiber volume fraction (V_f), filled-matrix (E_m) and fiber (E_f) materials on tensile modulus $(d\sigma/d\varepsilon)_o$ to be useful in BMC composite design.

1.13 'Fiber end crazing' model

Crazing in the form of whitening is reported in polymers and their fiber reinforced composites at the fiber ends. In polypropylene/glass fiber (GF/PP) stress is concentrated at the fiber tips and leads the matrix to crazing [1.8]. Lhymn and Shultz reported voiding, microcracking and crazing at fiber end sites during tensile deformation of injection-molded E-glass fiber (d = 12 μm) reinforced poly(ethylene terephthalate) [1.22]. Choi and Takahasi reported fracture processes of short fiber thermoplastic composites involve microcracking, microvoiding, shear-band formation and/or crazing in the matrix or interface [1.25].   In injection-molded short glass fiber polypropylene (SGFRP) subjected to notched Charpy impact tests, it was concluded that the matrix fails by crazing [1.39] In 3-point bend tests of GFRP PVC, Yuan et al. found numerous elongated fibrils near the fiber ends approximately 0.1 μm in diameter about the same size as craze fibrils found in fatigue tests of the PVC [1.23].
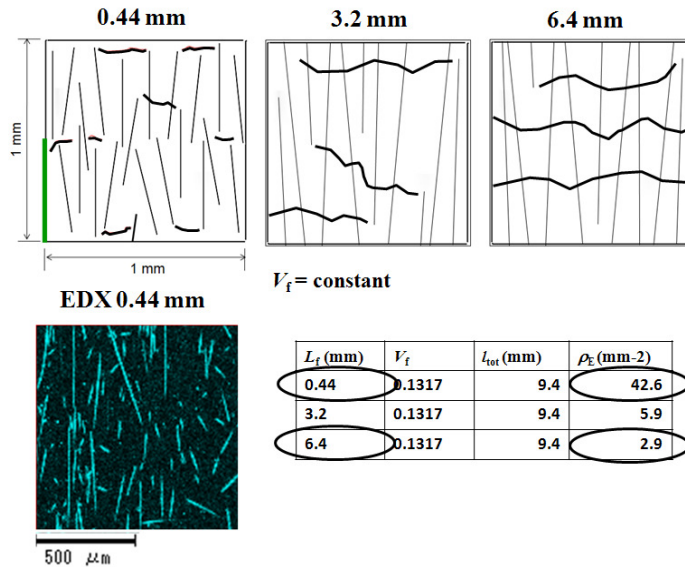
Fig. 1.15   Fiber end density affecting crack propagation in the BMC.

In the GFRP-BMC crazing was found at fiber ends in the form of whitening and incoherent interface along the lengths. A novel 'fiber end crazing' model is constructed on the basis of fiber end density vs. tensile stress and its strain. Figure 1.15 drawn proportionally according to relative fiber end density in the 0.44, 3.2 and 6.4 mm samples shows the shorter fiber 0.44 mm fiber samples have 13.5 times higher fiber end density than the 6.4 mm. Crazing sites are well-known to act as compressive sites. The model shows cracks being halted at the compressive stress sites in the shorter fiber sample. The model predicts tensile stress and strain increase linearly with fiber end density.

1.14 Velocity profile characterization of shortened-fiber BMC

To investigate the feasibility of processing using the short-fiber 0.44 mm GFRP-BMC paste in the factory, velocity profile and rheological parameters in the injection-molded sample have been investigated by means of fiber orientation mapping by SEM. This work does not claim to simulate the entire injection molding process. However, the claim is it is possible velocity profile of the paste through the mold cavity and some rheological properties can be estimated from fiber orientation mapping with respect to mold flow direction, and shot time, t_s it takes for the paste to fill the mold. This is demonstrated by the SEM mapping. This method could possibly be used as an additional evaluation to obtain a rough or better estimation of actual flow patterns and velocities to later simulate or optimize entire molding process by computer simulation. Moreover, this method is used to evaluate the excellent mold flow conditions for processing the shortened 0.44 mm fiber length BMC paste in industry.

1.14.1   Obtaining rheological properties of mold-flow in polymer composites

There is an extensive body of research and texts on numerical simulation to obtain rheological properties of injection molded resin and their GFRPs dating back until at least the 1970s, several cited by Greene and Wilkes [1.66]. However, there appears to be no or little research on estimating velocity profile and its flow parameters from fiber

orientation mapping. Some recent works at the time of this dissertation on GFRP fiber orientation include microstructure characterization [1.62-1.63],.interaction with processing parameters and mechanical properties [1.11, 1.55, 1.56, 1.57, 1.64], and mathematical modeling [1.67].

Two-phase fiber-polymer polyamide 6,6 exhibits a 5-layered flow pattern across specimen thickness [skin- shell- core –shell -skin] consisting of highly random thin skins approximately 4% of sample thickness with relatively thick highly oriented shell layers surrounding a thick inner core with a near random in-plane fiber orientation [1.11]. In short and long glass fiber polyamide injection-molded rectangular cuboid-shaped plaques, Akay and Barkley correlated longitudinal and transverse fiber flow orientations with tensile and dynamic mechanical and fracture properties [1.64]. Taking cross sections parallel to the flow line at various depths, they found a 3-layer [skin-core-skin] flow pattern appearing to transition into 5-layers with depth. Core thickness also increased with injection speed, melt and mold temperatures [1.64].

1.14.2   Hele-Shaw model

A typical model used for injection molding simulation is by Hele-Shaw [1.68] that gives simplified equations for non-isothermal, non-Newtonian, inelastic flows in a thin cavity. Normally the following assumptions are proposed by Hele-Shaw prior to mathematical modeling: 1) cavity thickness is much less than width; 2) incompressible polymer melt behaves as viscous with no elastics where viscosity is shear-dominated; 3) viscous force is much higher than inertia or gravitational forces; 4) in thickness direction, velocity and pressure gradient are zero; 5)   no fountain flow exits at flow front; 6) velocity is zero at mold walls; and 7) heat transfer between mold and paste is dominated by conduction then heat transfers into the core by convection. If we used the Hele-Shaw model, assumptions 1), 4) and 5) do not apply to the BMC since cross-sectional dimensions are 3.3 x 12.6 mm; and fountain flow is observed at the flow front. While widely used, the Hele-Shaw model does not take into account fiber orientations with velocities, therefore the new approach of flow-front mechanics is proposed.

1.14.3   Laminar creep flow

Figure 1.16 shows Reynolds numbers for various materials flowing through the 3.3 x 12.6 mm gauge section of the injection-mold pictured as a rectangular duct. Fiber angle orientation mapping shows the 3-phase GFRP-BMC has been found to exhibit a 3-layered flow pattern of [skin-core-skin] where the profile is inferred here as a solidification wavefront 3-D elliptical paraboloid resembling classical laminar flow through a conduit that can apparently be estimated by Navier-Stokes equations.
Picturing the mold cavity as a straight rectangular duct, there are factors to consider. First, the BMC is opaque and has low contrast between fiber and matrix. While the accepted transition Reynolds number (Re) from laminar to turbulent flow is ~2300 for circular pipe [1.69], the thick paste 3-phase BMC injection-molded polymer composite exhibits extremely low Re ~2.4×10^{-4} undergoing highly viscous laminar creep motion classified as Stokes Flow, and lower than 2-phase fiber-polymer systems without filler. Stokes Flow is typically accompanied by a thick boundary layer where viscous forces dominate over inertial forces [1.69].

15
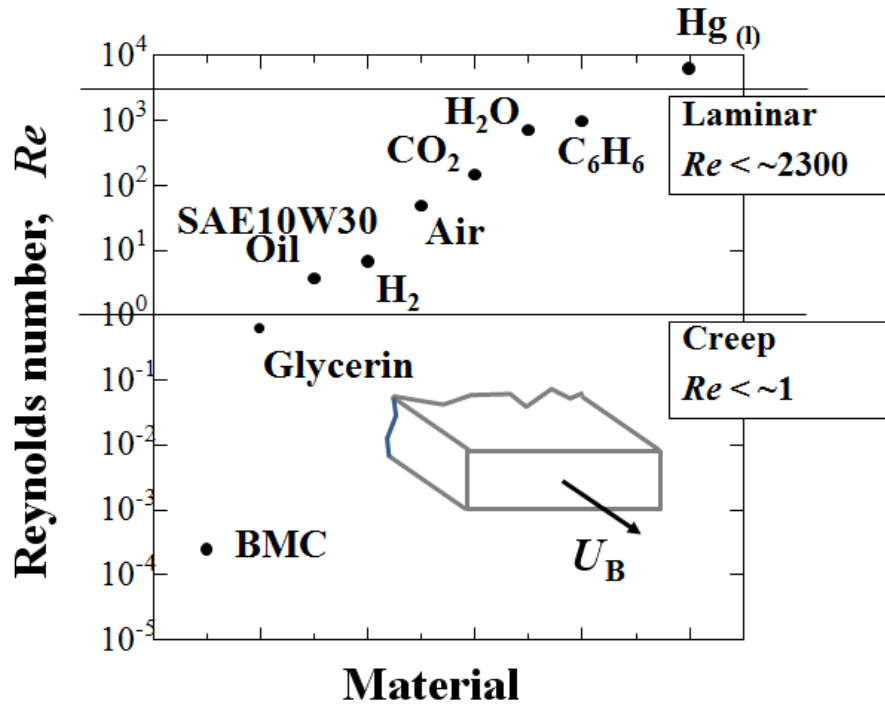
Fig. 1.16 Reynolds numbers for various materials flowing through the 3.3 x 12.6 mm gauge section of the injection-mold pictured as a rectangular duct [1.67, 1.68 - 1.69].

1.14.4 Low Reynolds number and smooth mold flow

These extremely low Re numbers act as an advantage for homogeneity of the part since entrance length, L_e at which the flow pattern and boundary layer stabilize [1.70] calculated for laminar flow [1.69, 1.71, 1.72] is nearly negligible in comparison to mold cavity length. Therefore, to characterize the GFRP-BMC flow through a conduit, the velocity profile and its flow parameters are estimated from fiber angle distribution across gauge section thickness.

1.14.5 Obtaining shear rate by the Mooney-Rabinowitsch equation

To obtain flow parameter approximations taking into account the non-Newtonian shear thinning behavior of the BMC paste, dynamic viscosity measurements of Couette flow were carried out by rheometer at Premix, Inc. A linear Arrhenius relationship between dynamic viscosity η (Pas) and shear rate $\dot{\gamma}$ (s^{-1}) was obtained at 20°C where viscosity was $9.0 \times 10^3 < \eta < 4.3 \times 10^5$ Pas for shear rates between $10^2 > \dot{\gamma} > 10^0$ s^{-1}. In the specimen, the $\dot{\gamma}$ cannot be measured directly, but can be calculated from the measured average flow (bulk) velocity, U_b by the Mooney-Rabinowitsch equation [1.73]:

$$\dot{\gamma} = 4Q/\pi R^3 = 8U_b/D_H \qquad (1.7)$$

where $\dot{\gamma}$ is referred to as "average shear rate", Q is volumetric flow rate (m^3/s), R is radius if circular pipe (m), U_b is bulk velocity (0.135ms^{-1}), D_H is hydraulic diameter (m), for a square duct equal to $4A/P$ where A is specimen cross sectional area, and P is wetted perimeter calculated as total perimeter, $2(w+th)$ [1.72], hence $\dot{\gamma}$ is 206 s^{-1}.

Interpolation of the Arrhenius relationship yields bulk viscosity η_b of 5.0 x 10^3 Pas which we will use for calculations. The polyester melt viscosity, η_{melt} is ~2 Pas at 163°C.

REFERENCES

[1.1] Faudree M., Proc. 36th Int. SAMPE (Society of the Advancement of Material and Process Engineering) Symposium, April 15-18, 1991) pp. 1288-1301.

[1.2] *World Glass Fibre Reinforced Plastic (GFRP) Composites Market 2013-2023 - Propects for Fibreglass & GRP*: Visiongain, Feb. 2013.

[1.3] Fu S-Y., Feng X-Q., Lauke B., and Mai Y., Compos. Part B. Eng **39** (2008) 933–961.

[1.4] Thomason J. and Vlug M., J.Compos. A: Appl. Sci. and Manuf. **27** (1996) 477-484.

[1.5] Thomason J. and Vlug M., J.Compos A : Appl. Sci. and Manuf. **28** (1997) 277-288.

[1.6] Fu S-Y. and Lauke B., Compos. Sci. and Tech. **56** (1996) 1179-1190.

[1.7] Huang H., and Talreja R., Compos. Sci. and Tech. **66** (2006) 2743-2757.

[1.8] Homayonifar M. and Zebarjad S., Materials and Design **28** (2007) 1386-1392.

[1.9] Fu, S-Y., Lauke B., Mader E., Yue C-Y., Hu X., Compos. A: Appl. Sci. and Manuf. **31** (2000) 1117-1125.

[1.10] Thomason J., Composites **A 39** (2008) 1732-1738.

[1.11] Seol K., Krawitz A., Richardson J., and Weisbrook., C., Mater. Sci. and Eng. **A 398** (2005) 2846-2851.

[1.12] Niihara K., Ceramics no Kyoujinka (Fracture Toughness of Ceramics) **21** (1986) 580-589.

[1.13] Tohgo K., Itoh Y. and Shimamura Y., Compos A, Appl. Sci. and Tech. **41** (2009) 313-321.

[1.14] Starink M., Syngellakis S., Mater. Sci. Eng. **A270** (1999) 270-277.

[1.15] *ASM engineered materials reference book, 2nd ed*. Bauccio M., editor. Materials Park, Ohio: ASM International, 1994.

[1.16] Yang L., Yan Y., Ma J., Liu B., Computational Matl. Sci. **68** (2013) 255-262.

[1.17] Sirivedin D., Fenner D., Nath R. and Galiotis C., Compos. A Appl. Sci. and Manuf. **34** (2003) 1227-1234.

[1.18] Sirivedin D., Fenner D., Nath R., Galiotis C., Compos. A Appl. Sci. and Manuf. **37** (2006) 1936-1943.

[1.19] Corscadden S. and Payne D., Compos. Manuf. **1** (1990) 173-182.

[1.20] Aktay L., Johnson A. and M. Holzapfel: Computat. Mater. Sci. **32** (2005) 252-260.

[1.21] Tyson W. and Davies G., Br. J. Appl. Phys. **16** (1965) 199-206.

[1.22] Lhymn C. and Schultz J., J Mater Sci. **18** (1983) 2029-2046.

[1.23] Yuan J., Hiltner A., Baer E., J. of Mater. Sci. **20** (1985) 4377-4386.

[1.24] Schinker M., Konczol L., and Doll W., J. Mater. Sci. Lett. I (1982) 475.

[1.25] Choi N. and Takahasi K. (2002) ED. By Stoyko Fakirov, *Handbook of thermoplastic polymers, copolymers, blends and composites*, Chapter 25 Fracture behavior of discontinuous fiber-reinforced injection-molded polymer composites ISBN 3-527-30113-5).

[1.26] Zebarjad S., Materials and Design **24** (2003) 531-535.

[1.27] Song D-Y., Takeda N., Shioya T., Nakata K., Compos. A: Appl. Sci. and Manuf. **27** (1996) 357-364.

[1.28] Carman G. and Reifsneider K., Compos. Sci. and Tech. **43** (1992) 137-146.

[1.29] Faudree M. and Nishi Y., Mater. Trans. **51** (2010) 2304-2310.

[1.30] Williams J., *Mixed Mode Fracture, Fracture Mechanics of Polymers*, (Ellis Horwood: Chichester, UK, **75**, 1984).

[1.31] Yuan J., Hiltner A., and Baer E., Polym. Compos. **7** (1986) 26-35.

[1.32] Griffith A., Phil. Trans. Roy. Soc. **A 221** (1920) 163-198.

[1.33] Shultz, J. and Friedrich, K., J. Mater. Sci. **19** (1984) 2246-2258.

[1.34] Karger-Kocsis J., Compos. Sci. and Tech. **48** (1993) 273-283.

[1.35] De Focatiis, D. and Buckley C., Polymer **52** (2011) 4045-4053.

[1.36] Shiba M. and Kishi T., Bulletin of Japan Institute of Metals **27** (1988) 644-649.

[1.37] Solar M. and Belzunce F., Compos. **20** (1989) 120-124.

[1.38] Sumner, M., Sankarapandian, M., McGrath, J., Riffle, J., and Sorathia, U., Polymer **43** (2002) 5069-5076.

[1.39] Xingtian,Y., Fangping,Y., Zhirong, X., and Zheng, S., Polymer **50** (2009) 4089-4100.

[1.40] Sato H., Inoue, Y., Iwata, K., Tonegawa, A. and Nishi, Y., J. Jpn. Inst. Met. **72** (2008) 520-525.

[1.41] Nishi Y., Kobayashi, H., and Salvia, M., Mater. Trans. **48** (2007) 1924-1927.

[1.42] Nishi Y., Mizutani A., and Uchida, N., J. Thermoplastic Compos. Mater. **17** (2004) 289-302.

[1.43] Nishi Y., Toriyama, T., Oguri, K., Tonegawa, A. and Takayama, K., J. Mater. Res. **16** (2001) 1632-1635.

[1.44] Nishi Y., Mizutani A, Kimura, A., Toriyama, T., Oguri, K., and Tonegawa, A., J. Mater. Sci. **38** (2003) 89-92.

[1.45] Yamaguchi N., Oguri K., Tonegawa A., and Nishi Y., J. Jpn. Inst. Met.**68** (2004) 198-201.

[1.46] Oguri K., Iwataka N., Tonegawa A., Hirose Y., Takayama K., and Nishi Y., J. Mater. Res. **16** (2001) 553-557.

[1.47] Oguri K., Fujita K., Takahashi M., Omori Y., Tonegawa A., Honda, N. Ochi, M., Takayama K., and Nishi Y., J. Mater. Res. **13** (1998) 3368-3371.

[1.48] Oguri K, Iwatani N., Izumi H., Tonegawa A., Takayama K., and Nishi Y., Proc. 2nd Japan-France Seminar on Intelligent Materials and Structures, (University of Louis Pasteur Strasbourg, France) (1998) pp. 142-144.

[1.49] James A. and Lord M., Macmillan's *Chemical and Physical Data*, London and Basingstoke, (The Macmillan Press, Ltd., 1992) pp. 484-485.

[1.50] Gordon A. and Ford R., *The Chemist's Companion: A Handbook of Practical Data, Techniques, and Reference*s, (Wiley Interscience Publication, 1972) pp. 112-113.

[1.51] ASTM D 6264-98 (1998).

[1.52] Imielińska K., Guillaumat L., Wojtyra R. and Castaings M., Compos. **B 39** (2008) 1034-1041.

[1.53] Vaidya A., Vaidya U., and Uddin N.: Mater. Sci. Eng. **A 472** (2008) 52-58.

[1.54] David-West O., Nash D. and Banks W., Compos. Struct. **83** (2008) 247-258.

[1.55] Cox H. Brit. J. Appl. Phys. 3 (1952) 72-79.

[1.56] Krenchel H. *Fibre reinforcement*. Copenhagen: Akademisk Forlag; 1964.

[1.57] Thomason J., Comp. Sci. Tech. **59** (1999) 2315-2328.

[1.58] Dragoi D., Ustundag E., Clausen B. and Bourke M., Scripta Mater. **45** (2001) 245-252.

[1.59] Halpin J. and Cardos J., Polym. Eng. and Sci. **16** (1976) 344-352.

[1.60] Rezaei F., Yunus R., Ibrahim N and Mahdi E., The Malaysian J. Anal. Sci. **11** (2007) 181-188.

[1.61] Pang J. and Fancey K., Compos. Sci. Tech. **68** (2008) 1903-1910.

[1.62] Toll S. and Andersson P., Polym. Compos. **14** (1993) 116–25.

[1.63] Toll S. and Andersson P., Composites **22** (1991) 298–306.

[1.64] Akay M. and Barkley D., J .Mater. Sci. **26** (1991) 2731-2742.

[1.65] Faudree M. and Nishi Y., Mater. Trans. **54** (2013) 1877-1883.

[1.66] Greene J. and Wilkes J., Polym. Eng. and Sci. **37** (1997) 590-602.

[1.67] VerWeyst B., Tucker C. III, Foss P. and O'Gara J., Intl. Polym. Proc. **4** (1999) 409-420.

[1.68] Hieberand C. and Shen S., J. Non-Newt. Fluid Mech. **7** (1982) 1–32.

[1.69] White F. *Fluid Mechanics*, 4th Edition, (New York:WCB/McGraw-Hill, 1999) pp. 228, 327-331, 340, 428.

[1.70] Anselmet F., Ternat F., Amielh M., Boiron O., Boyer P. and Pietri L., C.R.Mecanique **337** (2009) 573-584.

[1.71] Schlichting H., *Boundary Layer Theory*, 7th Edition (New York: McGraw-Hill, 1979).

[1.72] White F., *Viscous Fluid Flow*, 2nd Edition (New York: McGraw-Hill, 1991).

[1.73] Severs E. and Austin J., Ind. Eng. Chem. **46** (1954) 2369-2375.

Chapter 2 Experimental

2.1 Introduction

Two types of BMCs were examined 1) compression-molded [2.1] and; 2) injection molded [2.1-2.3].   The compression-molded samples had 11 wt% glass fiber and 55% CaCO$_3$ filler.   The injection-molded samples had 20 wt% glass fiber and 47.1% CaCO$_3$ filler. The formulations for both compression-molded and injection-molded samples are those used commercially fabricated by Premix, Inc. of North Kingsville, Ohio.

2.2 Fabrication of compression-molded specimens
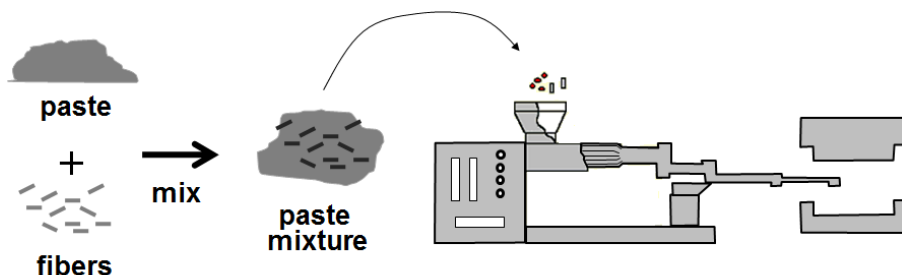
Fig. 2.1 Schematic of compression molding process.

Figure 2.1 is a schematic of the compression molding process where the paste composed of CaCO$_3$ filler and resin was mixed with glass fibers by Banbury mixer prior to molding. Compression-molded specimens were fabricated to determine the effect of texture angle, homogeneous low voltage electron beam irradiation (HLEBI), and shortening fibers to sub-millimeter on Charpy impact value. Glass fiber reinforced polymer bulk molding compound SGFRP-BMC panels 304.8 x 304.8 mm (12 x 12 in) and 2 mm thick were provided by Premix, Inc., North Kingsville, Ohio. Table 2.1 lists the components of 13.75 mass% propylene glycol maleate polyester resin (33 mass% styrene solution), 12.75 mass% styrene butadiene copolymer (70 mass% solution in vinyl toluene), 11 mass% commercial E-glass fibers with nominal length of 6 mm, 55 mass% calcium carbonate filler (CaCO$_3$), 3 mass% aluminum silicate filler (AlO)$_2$SiO$_3$, 0.5 mass% magnesium hydroxide Mg(OH)$_2$, and the balance proprietary (Table 2.1) [2.1].

COMPONENT	Mass%
propylene glycol maleate polyester	13.75
styrene butadiene copolymer	12.75
commercial E-glass fibers	11
CaCO$_3$ filler	55
aluminum silicate filler	3
magnesium hydroxide	0.5
proprietary initiators and inhibitors	4

Table 2.1 Compression-molded BMC formulation.

PARAMETER	Condition
Mold Pressure	5.5 - 6.9 MPa (800-1000 psi)
Temperature	422°K (149°C)
Cure time	2 min
Mold Type	matched metal die compression mold

Table 2.2 Processing parameters.

2.2.1 Mold flow and specimen configuration

Table 2.2 shows the processing parameters where the components were mixed in a double-arm sigma blade mixer for 20 min at room temperature prior to molding at 5.5-6.9 MPa (800-1000 psi) pressure in a matched-metal die compression mold at 422°K (149°C). A single charge mass of paste was placed in the center of the mold, compressed and cure time was 2 min [2.1]. Poisson's ratio of the molded product is given by the manufacturer to be $\nu = 0.30$. Volume fractions, V_f of glass fiber, $CaCO_3$ filler, and remaining polymer mixture were calculated to be 0.080, 0.377, and 0.543, respectively.

To investigate the effect of shortening fiber length to sub-millimeter, additional panels were manufactured with extended mix of 30 min (50 min mix total) prior to compression molding.
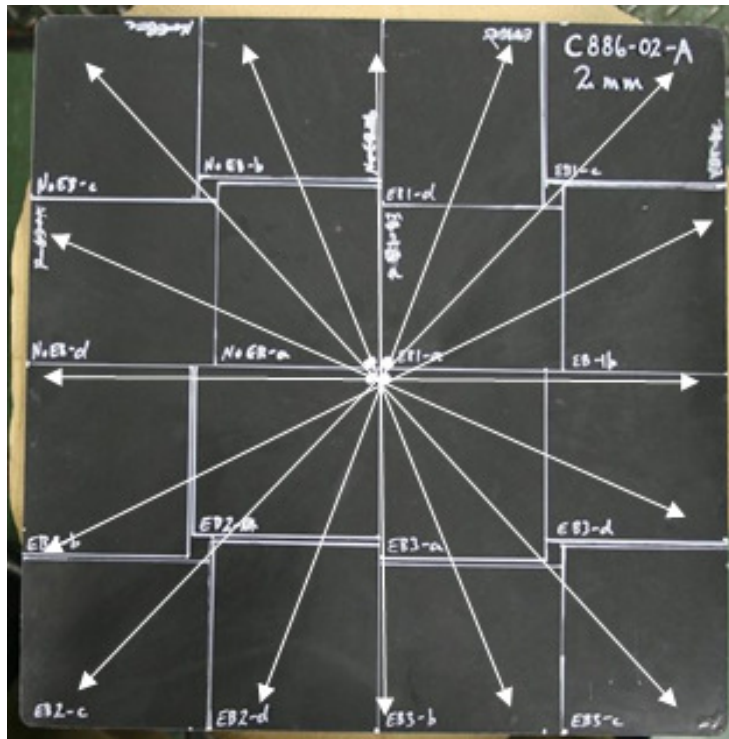
Fig. 2.2 Photo of Compression molded GFRP-BMC panel with approximate paste flow lines drawn outward from center.

As depicted in Figure 2.2 panel mold flow direction was outward from center. The material is orthotropic, where material properties in three perpendicular axes: axial, circumferential and radial are different, similar to wood. For simplicity, isotropy was assumed across the axial 2 mm thickness. The panel was sectioned into 4 quadrants which were further sectioned into 4 smaller sub-quadrants cut in spiral configuration into 'section-a', 'section-b', 'section-c', and 'section-d', respectively since flow is approximately radially outward during the compression molding process. This is in accordance with ASTM D 6110-02 (2002) which calls for specimens to be cut in both lengthwise and crosswise directions from anisotropic panels [2.4].
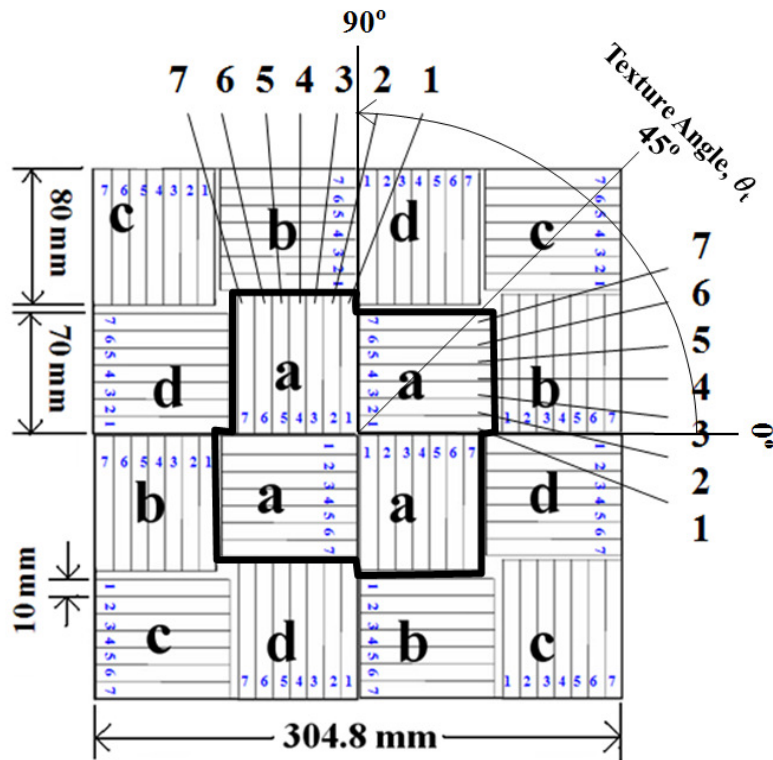
Fig. 2.3 Schematic of compression molded GFRP-BMC panel showing specimens cut in spiral configuration according to ASTM.

Figure 2.3 shows each sub-quadrant 'a', 'b', 'c', and 'd' is assumed to have equal flow conditions with their counterparts since they are the same positions and orientations relative to the center. For consistency, each sub-quadrant has specimens 1–7 counted outward from the position closest to panel center (for example in section-a in Fig. 2.2). Specimens were cut to size for Charpy impact tests with dimensions length, width and thickness [l x w x t] of 80 x 10 x 2 mm according to US standard Japan industrial testing standard JIS K 7077 [2.5].

2.2.2 Texture angles

section	θ_t (deg)	θ_t range
a	0 to 90	Random
b	68	+/- ~7
c	45	+/- ~10
d	17.5	+/- ~17.5
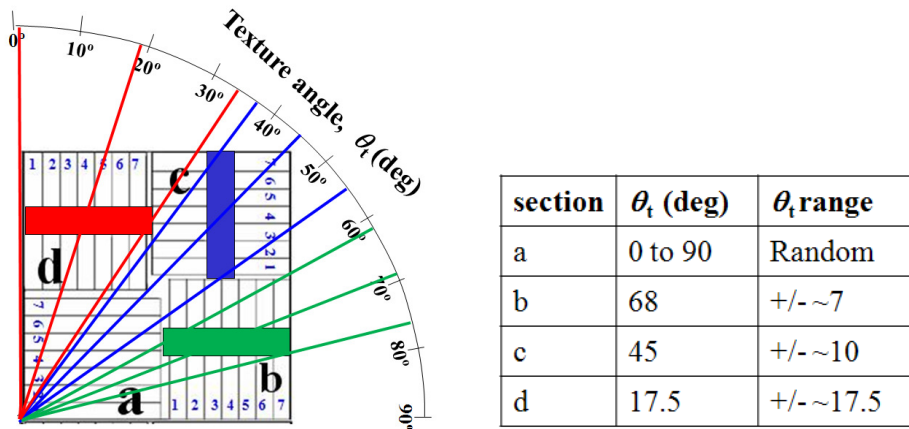
Fig. 2.4 and Table 2.3 Schematic of a panel quadrant showing texture angle, θ_t and their range, $\Delta\theta_t$ designations in the areas of Charpy impact in the specimen centers.

Figure 2.4 shows the mean texture angles, θ_t (deg) with respect to longitudinal direction of testing samples of each sub-quadrant, 'a', 'b', 'c', and 'd' where center lines are drawn through the center of center-specimen number 4 in each case. The θ_t range encompasses the shaded center of the specimens where the impact test will be applied. Hence, the θ_t listed in Table 2.3 are 45° +/- 45° (0° to 90°) for section-a, 68° +/- 7° for section-b, 45° +/-10° for section-c and 17.5^o +/- 17.5^o for section-d, respectively.

2.3 Non-destructive test at very low deformations

Fig 2.5 Photo of non-destructive laser bending test setup.
Fig 2.6 Sequence of tests.

Figure 2.5 shows the bending setup. Prior to and after HLEBI irradiation, non-destructive bending test standard JIS K 7074-1998 [2.6], was carried out on the Charpy impact specimens [l x w x t] = 80 x 10 x 2.0 mm at very low deformations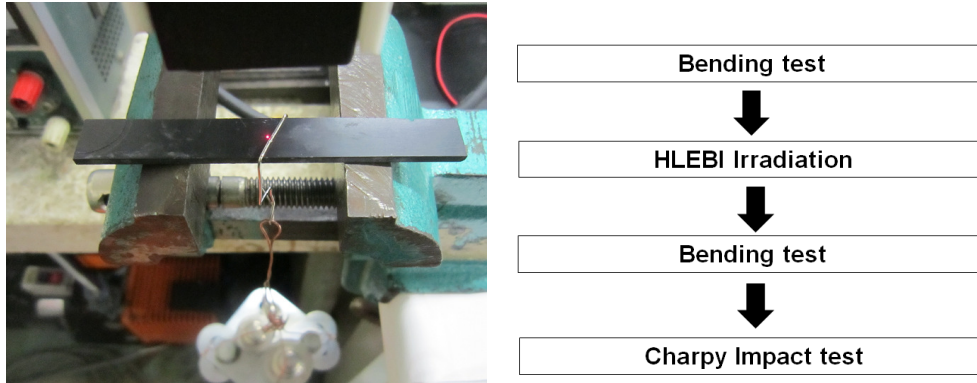 measuring displacement by red laser shown Fig. 2.5. Warm-up time of the laser setup was 1 hr. Weights of 100, 200 and 400g were suspended from the center of the sample with a homemade hook device. A voltmeter recorded the displacement where 1mA = 1μm. Carefulness was heeded to prevent any external vibrations. The bending stress (σ) and strain (ε) are expressed by eqs. (2.1 and 2.2) [2.6]:

$$\sigma \quad = \quad (3PL) \, / \, (2wt^2) \qquad\qquad (2.1)$$

$$\varepsilon = (6td) \, / \, L^2 \qquad\qquad (2.2)$$

Here, σ, P, L, w, t, ε, and d are bending stress (MPa), load (N), distance between supporting points (32 mm), sample width, sample thickness, bending strain, and amount of deflection (mm), respectively.

The flexural modulus, E_f (GPa) is expressed by eqn. (2.3) [2.6]:

$$E_f = (1/4)[L^3/(wt^3)] \, (P/d) \qquad\qquad (2.3)$$

The test sequence of testing is shown in Figure 2.6.

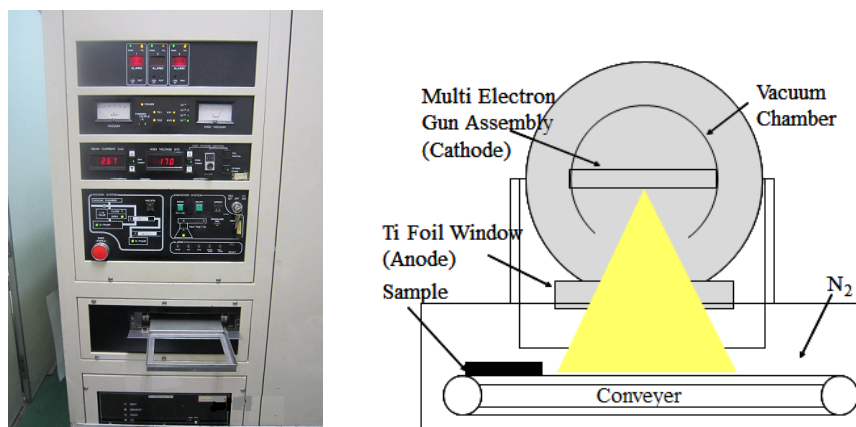## 2.4   Homogeneous low-voltage electron beam irradiation (HLEBI)

Fig 2.7 Photo of HLEBI equipment (Iwasaki)
Fig 2.8 Schematic of curtain processor of HLEBI equipment

Homogeneous low-voltage electron beam irradiation (HLEBI) was applied to compression-molded samples prior to Charpy impact. The HLEBI equipment is shown in Figure 2.7. Samples were homogeneously irradiated using an electron-curtain processor (Type LB250/15/180L), Energy Science, Inc., Woburn, MA, Iwasaki Electric Group, Ltd., Tokyo) [2.7-2.12] as illustrated in Figure 2.8 with the electron beam through a titanium thin film window attached to a vacuum chamber, ~240 mm in diameter. A tungsten filament in the vacuum was used to generate the electron beam at an acceleration potential of 170 kV and irradiating current of 2.68 mA. To prevent oxidation, the samples were kept in a 1 atm N_2 atmosphere with a residual O_2 concentration below 300 ppm. The N_2 gas molar flow rate was 89 N/min. The distance between sample and Ti window was 30 mm.

Acceleration voltage	170 kV
Irradiating current	2.68 mA
Irradiation environment	N_2 gas atmosphere
Residual O_2 conc.	< 300 ppm
Conveyor speed	10 m /min
EB dose /sweep	0.0432 MGy
Sweep time (one way)	0.20 s
Gap interval bet. sweeps	20 s
EB yield calc.	FWT Nylon dosimeter

Table 2.4 HLEBI parameters.

Samples were transported in a 200 x 150 mm aluminum plate holder on a conveyor at a speed of 10 m/min. One sweep going one way was 0.0423 MGy for the short time of 0.20 s to avoid excess heating of the sample. Repetitive applications to both side surfaces were applied to achieve the desired dose of HLEBI, with a gap interval of 20s between each sweep. The parameters are summarized in Table 2.4. The resulting EB dosage was proportional to the yield value determined from the irradiation current, I (mA) conveyor speed, S (mmin^{-1}), and number of irradiations, N [2.1]:

$$D = 0.216(I/S)N \qquad (2.4)$$

The yield value was calibrated by FWT nylon dosimeters (Far West Technology, Inc. 330-D South Goleta, CA 93117).

2.4.1 Penetration depth, D_p of HLEBI

Penetration depth by the electron beam irradiation (HLEBI) is one of the important factors for dominating productivity and material thickness choice to apply for practical use. Based on the sample density, ρ (kgm^{-3}) and irradiation voltage, V (MeV), the EB-irradiation depth, D_p (m) can be obtained by assumptions of Christenhusz and Reimer [2.13],

$$D_p = 66.7V^{5/3}/\rho \tag{2.5}$$

The surface electrical potential (130 keV) can be determined from the electrical potential (170 keV) the 10 μm Ti thickness (ρ = 4.54 Mgm^{-3}) and the 30 mm distance between the sample and window in the $N_{2(g)}$ atmosphere (1.1 kgm^{-3}). Since the calculated density of the short fiber compression-molded (11 wt% E-glass fibers) GFRP-BMC samples is ρ = 1.92 Mgm^{-3} the HLEBI depth, D_p estimated from eq. (2.2) is 116 μm when the densities of E-glass fiber, $CaCO_3$ filler, and remaining polymer mixture are 2.62, 2.80, and 1.20 Mgm^{-3}, respectively.

Using the volume fractions, V_f of the short glass fibers (0.080), filler (0.377) and polymer (0.543) along with the densities, estimated D_p by the Christenhusz and Reimer assumption for E-glass fiber, $CaCO_3$ filler, and remaining polymer mixture are 84.5, 79.1, 185 μm respectively.

Another common practice is the assumption by Libby [2.14] which relates D_p to mass thickness, l_o (gm^{-2}) and irradiation voltage, E (170 keV) in eq. (2.6) where:

$$l_o = E^{5/3}/150 \tag{2.6}$$

yielding l_o = 347.8 gm^{-2}. Since the electron beam has to travel through the Ti foil (l_o = 11.6 gm^{-2}) and $N_{2(g)}$ (l_o = 8.38 gm^{-2}) before hitting the sample, the mass thicknesses, l_o hitting the sample is reduced from 347.8 to 328 gm^{-2}. Therefore, by eqn. (2.4) the voltage at the sample surface, E is calculated by:

$$E = (150 \, l_o)^{3/5} \tag{2.7}$$

where E =164 keV. Therefore, estimated D_p by the assumption of Libby [2.14] for E-glass fiber, $CaCO_3$ filler, and remaining polymer mixture are 125, 117, 273 μm respectively.

By both assumptions, estimated irradiated depth is (143 +/- 28 μm) at both side surfaces (5-9% of 2.0 mm sample thickness) of composite sheet with 2.0 mm thickness [2.13-2.14], it is expected that the HLEBI improves the impact value of the short fiber GFRP-BMC.
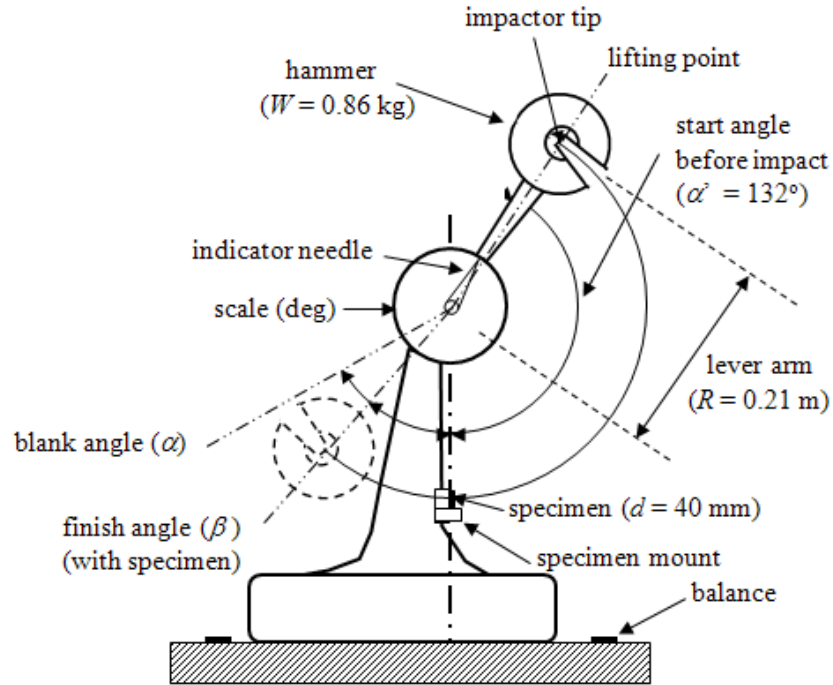
2.5 Charpy impact

Fig 2.9 Schematic of Charpy impact machine (Shimadzu Corporation No.51735). Angles α and β are exaggerated for clarity.

Charpy impact test utilizes a drop-weight pendulum and evaluates the impact absorption characteristics and relative impact toughness of materials often used in quality control applications employed as an inexpensive and fast way to estimate reaction to impact.

To evaluate dynamic fracture toughness, Charpy impact values for GFRP samples with and without HLEBI were measured. Unnotched Charpy impact samples were cut with a diamond cutter (MC-201, MARUTO) to dimensions 80 x 10 x 2 mm conforming to JIS K 7077-1991 testing standard [2.5, 2.15].

A standard impact fracture energy measurement system depicted in Figure 2.9 and photo in Figure 2.10 (Shimadzu Corp. No. 51735) was employed according to JIS K 7077-1991 [2.5, 2.15] to obtain impact fracture energy, E (kJ) absorbed by the specimen, calculated from the difference in height the hammer reaches between the blank test and specimen test calculated in eq. (2.8) [2.5, 2.15]:

$$E = WR[(\cos\beta - \cos\alpha) - (\cos\alpha' - \cos\alpha)(\alpha + \beta)/(\alpha - \alpha')] \qquad (2.8)$$

where, W is hammer mass (W=0.86 kg), R is length of hammer

Fig 2.10 Photos of Charpy impact machine.
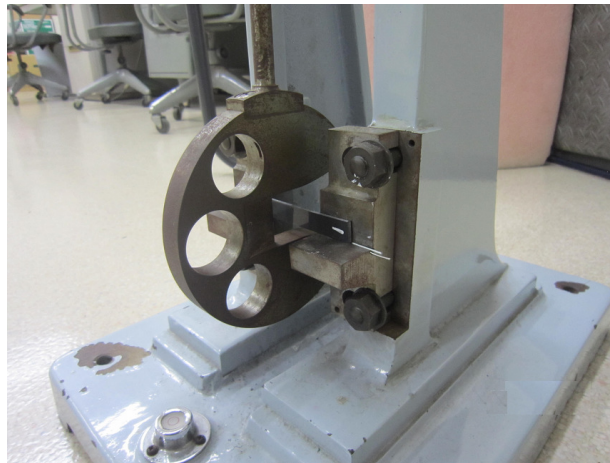
weight point from pivot center (R=0.21 m), β is maximum angle after impact (Radians), α is start angle before impact (α=2.3 Radians) or 132°, and α' is maximum angle of a blank test, respectively. The Charpy impact machine is first calibrated for temperature, humidity and air currents by the blank angle test which can vary 1-3° from summer to winter. Therefore, carefulness is recommended to run 3 blank tests before testing the samples. The hammer impacts the sample across its entire width with a hemispherical tip approximately 1.5 mm in diameter. When the Charpy impact test impact velocity, v hitting the sample is calculated as [2.16]:

$$v = [2gR(1 - \cos\alpha)]^{0.5} \qquad\qquad (2.9)$$

where g is gravitational constant (9.8 ms^{-2}), then v of the hammer hitting the specimen

is ~1.74 ms^{-1} (~3.89 mi/hr). The surface area, A of the impactor hitting the sample is small so KE/A is large.

Charpy impact value, a_{uc}, (kJ/m^2) is calculated by the following equation [2.5, 2.15]:

$$a_{uc} = E/(bt) \qquad\qquad (2.10)$$

where b and t were sample width and thickness (mm), respectively. The distance, d between supporting points was 40 mm. Evaluating the probability of fracture (P_f) has been a convenient method of quantitatively analyzing experimental values relating to fracture, often used in industry to determine manufacturing reliability in quality control. P_f is expressed by the following equation which is a generalized form of the median rank method [2.17]:

$$P_f = (I - 0.3)/(N_s + 0.4) \qquad\qquad (2.11)$$

where N_s and I are total number of samples and the ascending strength order of each sample, respectively. Impact tests were carried out 30+/-0.5 hr after EB irradiations.
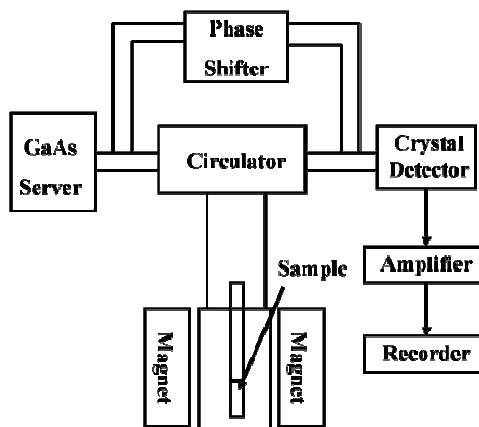
2.6 Electron spin resonance (ESR)

Fig 2.11 Photo of ESR equipment
Fig 2.12 Schematic of ESR equipment

To obtain more precise information on atomic-scale structural changes in the BMC-GFRP, the dangling bond density was obtained using an electron spin resonance spectrometer (ESR, JES-FA2000, Nippon Denshi, Ltd., Tokyo) [2.9, 2.18]. ESR is utilized to detect unpaired electrons by their spins (m_s = +/- 1/2) since electrons have a magnetic moment and spin quantum number. The unpaired electrons' magnetic moments either align themselves parallel or anti-parallel to an induced magnetic field producing a peak at a particular magnetic field, B. The photo and schematic are shown in Figures 2.11 and 2.12. ESR analysis of polymers demonstrated spectra are affected by coexistence of several kinds of radicals, effect of state of aggregation of polymer, and effect of irradiation dose and dose rate [2.12]. The microwave frequency range used in the ESR analysis was the X-band at 9.0374 ± 0.0005 GHz with a field modulation of 100 kHz. The microwave power was 1 mW. The magnetic field was varied from 297.000 to 347.000 mT. The electron spin density was calculated using a Mn^{2+} standard sample. Only ESR spectra, instead of spin densities, were given.

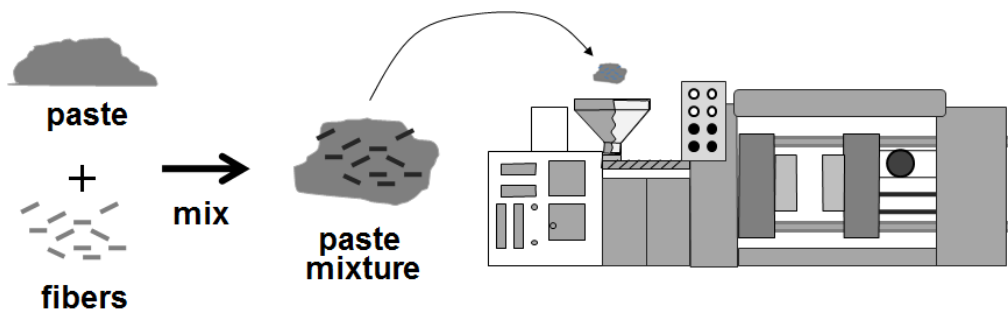## 2.7 Fabrication of injection-molded specimens

Fig. 2.13 Schematic of injection molding process.

Injection-molded specimens were fabricated to determine the effect of shortening fibers to sub-millimeter on tensile properties and mold flow behavior. Premix, Inc. of North Kingsville, Ohio provided the injection molded BMC (bulk molding compound) consisting of: 13.95 mass% propylene glycol maleate polyester (33 mass% styrene solution), 13.95 mass% styrene butadiene copolymer (70 mass% styrene solution), 20.00% mass% Owens and Corning OCF-405 E-glass fibers, 47.10 mass% calcium carbonate filler ($CaCO_3$), 0.35 mass% t-butyl perbenzoate, 0.10 mass% t-butyl peroctoate, 0.25 mass% carbon black pigment, 1.20 mass% calcium stearate, 3.00 mass% aluminum silicate, and 0.10 mass% magnesium oxide (Table 2.5). A matrix composite without glass fibers was made for comparison and had an identical composition as the fiber-containing samples omitting the fibers [2.2, 2.3]. The schematic of the injection molding process is illustrated in Figure 2.13.

The Injection-molded GFRP-BMC processing parameters are listed in Table 2.6. For all pastes, the components were mixed in a double-arm sigma blade mixer for 20 min. at room temperature. The paste was allowed to stand for several hours and then injected molded into an ASTM D-638 family mold for dogbone specimens with a 3.03 x 10^5 N (75 ton) New Britain with the following processing parameters: mold temperature 436°K (163°C), barrel temperature RT, injection pressure 3.50-6.90 MPa, shot time ~2.0s, hold time 15s, and cure time 1.5–2.0 min [2.2, 2.3].

INGREDIENT	Weight %
Propylene Glycol Maleate Polyester (33% Styrene solution)	13.95
Styrene-Butadiene Copolymer (70% Styrene solution)	13.95
t-Butyl Perbenzoate	0.35
t-Butyl Peroctoate	0.10
Carbon Black Pigment	0.25
Calcium Stearate	1.20
Calcium Carbonate	47.10
Aluminum Silicate	3.00
Magnesium Oxide	0.10
Glass Fibers	20.00

Table 2.5 Injection-molded GFRP-BMC ingredients.

PARAMETER	
Clamp Pressure	75 tons
Mold Temperature Stationary Movable	163°C 436°K 163°C 436°K
Barrel Temperature	Room Temperature
Injection Pressure	3500-6900 kPa
Hold Time	15s
Cure Time	1.5 to 2min
Press Type	75 Ton New Britain
Mold Type	ASTM D-647 Family Mold

Table 2.6 Injection-molded GFRP-BMC processing parameters.

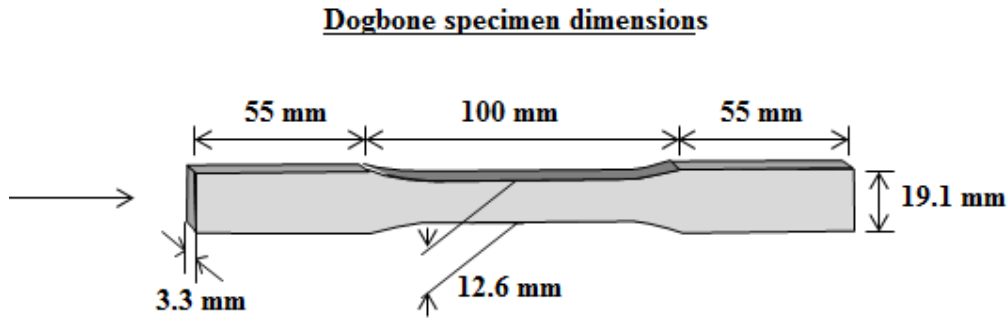### 2.7.1 Fiber length, l_f

Fig. 2.14 Dogbone specimen dimensions. Mold flow is indicated by the arrow.

Fiber length, l_f (mm) was varied including 6.4 mm, 3.2 mm, and masticated (0.44 mm) in the GFRP while fiber volume fraction, V_f was held constant at 0.1317. Nominal fiber diameter was 14–15 μm. The masticated samples were prepared by crushing the finished paste containing 3.2 mm fibers with a large sigma-blade Banbury mixer for an additional 30 min. The fibers in the matrix were shortened considerably and were not observed to be broken in the longitudinal direction. The $CaCO_3$ filler was not affected. The masticated paste was then left to stand overnight with the rest of the pastes before injection molding.

Average fiber length, l_f of about 1,000 fibers in the masticated samples was measured to be 0.44 mm with a standard deviation of 0.203 mm by SEM [2.3]. In general, two standard deviations comprise approximately 95% of the population, which is 0.04 mm $< l <$ 0.85 mm indicating a wide distribution from the additional mixing but still much shorter than the next average highest length tested of 3.2 mm. Fiber lengths were measured from the polished surface near the mold walls where fibers were observed to be aligned with the injection molding direction.

For the glass fiber containing samples, volume fractions V_f of the E-glass fibers, $CaCO_3$ filler, and polymers with remaining components were 0.1317, 0.2902 and 0.5781, respectively. The matrix composite without glass fibers had $V_f = 0.3330$ and 0.6670 of $CaCO_3$ filler and polymers. As shown in Figure 2.14, sample dimensions total length, gauge length, width, and thickness were ~210, 100, 12.6, 3.3 mm, respectively, with cross-sectional area of 42.0 mm^2 in the gauge length. For this study, the masticated samples will be referred to as the "0.44 mm samples". The matrix composite without glass fibers will be referred to as the "0% glass samples".

2.7.2 Fiber coupling agent

Owens Corning OCF-405 coupling agent was 1.2 mass% of the finished product. Fiber treatment began with preparing a water-epoxy resin emulsion, which is approximately 70 mass% by weight water and 30 mass% resin. The interfacial adhesion promoter, γ-methacryloxypropyltrimethoxysilane was approximately 1 mass% of this emulsion. The fibers were then coated with this emulsion and cured. The composition which remained on the fibers is proprietary [2.3].
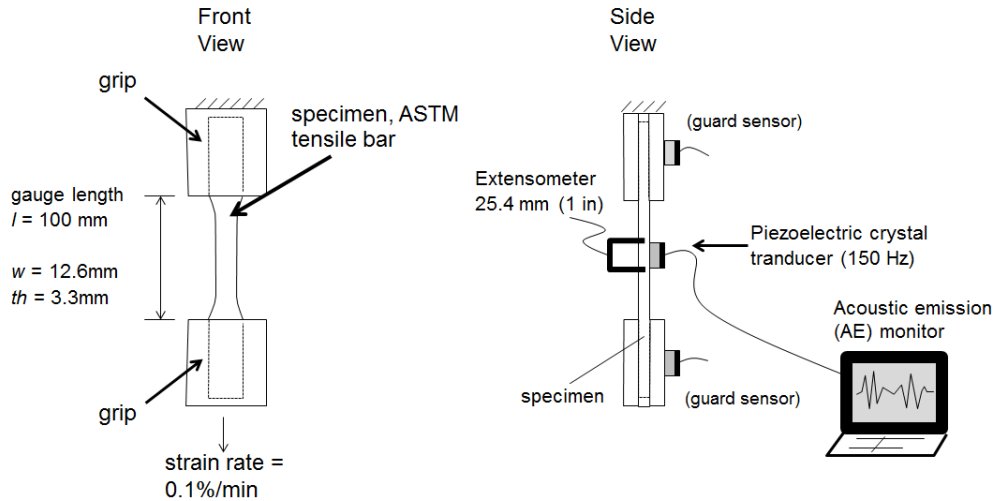
2.8 Tensile test

Fig. 2.15 Diagram of tensile test setup with AE.

Tensile specimens were also tested to determine the effect of shortening fibers. Figure 2.15 illustrates the specimen dimensions, tensile and acoustic emission (AE) setup. Experiments were carried out with an Instron® testing machine at a strain rate of 0.1%/min. At least 5 runs each were made for the 6.4, 3.2 and 0.44 mm samples, respectively while 3 runs were made for the 0% glass samples. Samples used for all tests had a gauge length of 100 mm, a width of 12.6 mm and a thickness of 3.3 mm, hence the cross-sectional area was 42.0 mm^2.

Strains were measured with a 25.4 mm (1.000 in) extensometer while stresses were measured with the Instron® testing machine
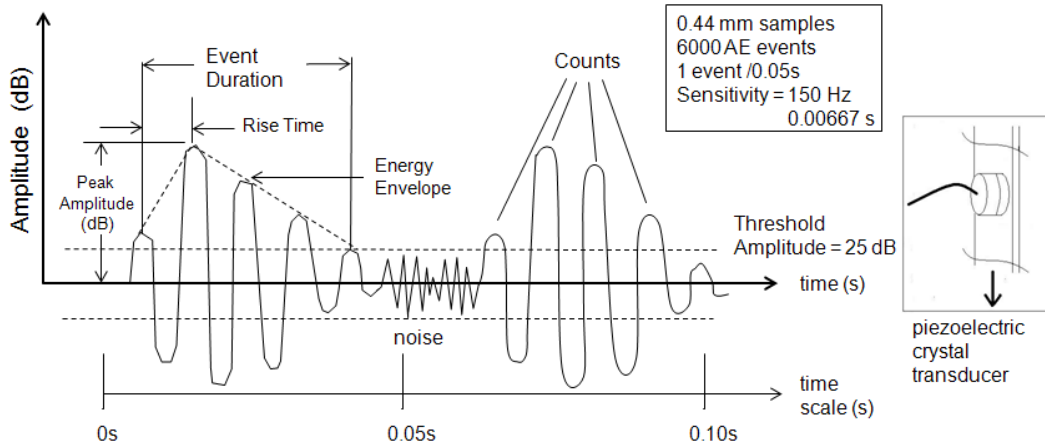
2.9 Acoustic emission (AE)

Fig. 2.16 Schematic of AE signal amplitude (dB) vs. time (left).
Fig. 2.17 Piezoelectric sensor mounted on the sample (right).

Figure 2.16 is a schematic of AE signal output during the tensile deformation process. Figure 2.17 shows the piezoelectric transducer coupled with the specimen. The threshold amplitude was set at 25 dB (dotted horizontal lines). Acoustic emission (AE) during tensile testing was monitored using a PAC R-15 piezoelectric crystal transducer with a maximum sensitivity of 150 Hz supplied by the Physical Acoustics Corporation. To insure efficient signal transmittance, an acoustic couplant was applied between the sensor and tensile specimens. AE signals were amplified and recorded by a PAC 3000/3004 system. The threshold amplitude was set at 25 dB to filter out extraneous background noise. Guard sensors were applied to both specimen grips. AE event distribution in dB was assessed. The 0.44 mm samples recorded about 6000 AE events during deformation at a crosshead displacement of 0.1 mmmin^{-1}. With a fracture strain of about 0.50 mm the sample deformed for about 5 min emitting 20 AE events s^{-1}. Therefore the transducer sensitivity of 150 Hz (resolution = 0.00667 sec) was much less than the AE average event measuring time of 0.05 sec (Fig. 2.14) indicating reliable measurement.

2.10 Scanning electron microscopy (SEM) and electron backscattering (EDX)

A Jeol JSM-35CF scanning electron microscope was used to observe polished and fracture surfaces of the injection-molded composite to correlate damage mechanism with the sequence of acoustic emission (AE) events. Specimens were polished with alumina powder and sputtered with Pt. A three-point bending apparatus was employed to examine the progression of damage events at increasing discrete deformations in the SEM. Specimens were cut and tested along the longitudinal direction to conform with the tensile tests. A detailed description of the three-point bending apparatus is given in Sato et al. [2.19].

To determine fiber spacing in the 0.44 mm samples at low magnification, Si-Kα and Ca-Lα1 energy levels were scanned by a Robinson Model BSE (backscattering electron) detector with the Jeol JSM-35CF SEM at measurement time of 150s;

acceleration voltage of 20.00kV; pulse processing time of P4; electron beam angle of incidence of 90 deg; dead time of 21%; X-Ray take-off angle of 35.0 deg; and probe electric current of 0.300 nA.

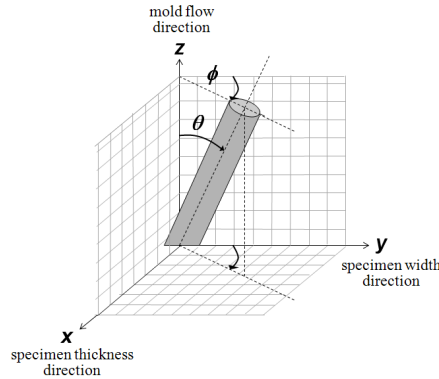## 2.11 Characterization method of velocity profile of the 0.44 mm fiber length SGFRP-BMC paste

Fig. 2.18 Fiber orientation in spherical coordinates as a function of θ and ϕ: angles (deg) with respect to the molding direction z-axis and width direction y-axis of sample, respectively.

A mosaic of SEM photos was taken of a 0.44 mm fiber length specimen across the 3.3 mm thickness normal to the tensile testing direction to obtain fiber orientations. The specimen was polished with alumina polishing paper with successive finesses and sputtered with Pt [2.21].

Velocity profile of the paste through the mold cavity was estimated from a fiber orientation mapping with respect to mold flow direction, and shot time, t_s it takes for the paste to fill the mold. Figure 2.18 depicts fiber orientation angle, θ (deg) with respect to tensile/molding direction and angle ϕ with respect to specimen width direction. To obtain the fiber orientations, θ power point computer program was used to meticulously position ellipses over 1,200 fiber cross sections across the specimen thickness at the center of the gauge section. Since this took much time, only one cross section could be examined.

Figure 2.19 shows an elliptical projection by which the orientation angle θ is calculated. As shown in Fig. 2.19 when fiber cross section elliptical shapes are assigned 'a' and 'b' for their short and long axes, respectively fiber orientations, θ (deg) with respect to mold flow direction are obtained from eq. (2.12) [2.20, 2.21]:

$$\theta = \arccos(a/b) \tag{2.12}$$

This is assuming circular fiber cross sections. The 2-D schematic to the right of Fig. 19 shows calculation for $a/b = 1/1.5 = 48$ deg.
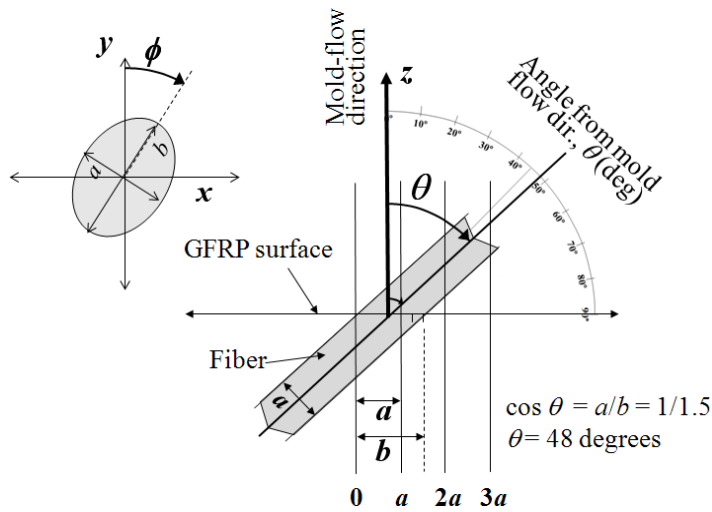
Fig. 2.19 Diagram of fiber angle with respect to mold-flow direction, θ.

Measurement accuracy of fiber cross-sections depends on computer screen size, resolution of computer program in positioning ellipses, and resolution of SEM photomicrographs. For the conditions of this experiment, ellipses could be sized in 650 nm increments, therefore error was within +/-650 nm. Hence, the error in measuring ellipse short axis, a (fiber diameter) was within +/-5.7% since average fiber diameter (a_{avg}) was measured to be 11.36 μm. Likewise, the average long axis of the ellipses, b_{avg} was 23.19 μm, thus percent error for long axes was within +/-2.8%.
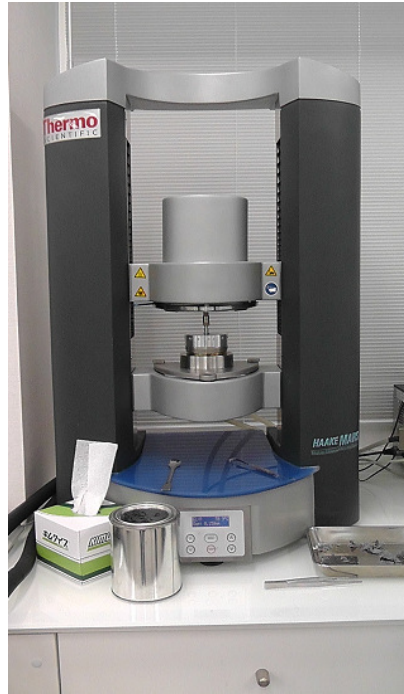
2.12 Viscosity measurements

Fig. 2.20 Photo of rheometer with parallel-plate fixture.

Viscosity measurements were carried out on the BMC paste: 1) without E-glass fibers and $CaCO_3$ filler, and 2) with both E-glass fibers and filler by a HAAKE MARS Modular Advanced Rheometer System a parallel-plate rheometer, Model Number 3 (Figure 20) at EKO Instruments Trading Company, Ltd. in (Shibuya) Tokyo, Japan. The top parallel plate had a 1-4 deg incline angle while the bottom plate was flat. Temperature was controlled by a CTC temperature control flow chamber. The heater consisted of a 150W heater on the outer perimeter with 100W radiation heater coils close to the specimen. The cooler was by water flow. The experimental conditions are listed in Table 2.7. For each temperature (deg C) one specimen was tested ramping the shear rate, $\dot{\gamma}(s^{-1})$ up then down. For the paste+fiber+filler recipe at $20^{o}C$ the shear rate was only ramped up.

Paste only
T = 20°C, 60°C, 100°C
$\dot\gamma$ = 1 ➔ 2 ➔ 5 ➔ 10 ➔ 20 ➔ 50 ➔ 100 ➔ 200 ➔ 100 ➔ 50 ➔ 20 ➔ 10 ➔ 5 ➔ 2 ➔ 1s^{-1}
Paste + Fibers + Filler
T = 20°C
$\dot\gamma$ = 1 ➔ 2 ➔ 3 ➔ 5 ➔ 10 ➔ 20 ➔ 30 ➔ 50 ➔ 100 s^{-1}
T = 170°C
$\dot\gamma$ = 3x10^{-5} ➔ 7.5x10^{-5} ➔ 1x10^{-3} ➔ 8x10^{-2} ➔ 0.1 ➔ 0.2 ➔ 0.3 ➔ 0.5 ➔ 1➔ 2 ➔ 3➔ 5 ➔ 10➔ 20 ➔ 30➔ 50 ➔ 100➔ 200 ➔ 100 ➔ 50 ➔ 30 ➔ 20 ➔ 10 ➔ 5 ➔ 2➔ 1 ➔ 0.5 ➔ 0.3 ➔ 0.2 ➔ 0.1 ➔ 6x10^{-5} ➔ 2.5x10^{-5} ➔ 3 x10^{-5} s^{-1}

Each temperature was a separate specimen.

Table 2.7 Viscosity measurement parameters.

REFERENCES

[2.1] Faudree M., Nishi Y. and Gruskiewicz M., Mater. Trans. **53** (2012) 1412-2310.

[2.2] Faudree M. and Nishi Y., Mater. Trans. **51** (2010) 2304-2310.

[2.3] Faudree M., Hiltner A., Baer E. and Collister J., J. Compos. Mater. 22 (1988) 1170-1195.

[2.4] ASTM D 6110-02 (2002).

[2.5] JIS K 7077 (1991).

[2.6] JIS K 7074 (1998).

[2.7] Nishi Y., Mizutani A. and Uchida N., Thermoplastic Compos. Mater. **17** (2004) 289-302.

[2.8] Nishi Y., Toriyama T., Oguri K., Tonegawa A. and Takayama K., J. Mater. Res. **16** (2001) 1632-1635.

[2.9] Nishi Y., Mizutani A., Kimura A., Toriyama T., Oguri K. and Tonegawa A. J. Mater. Sci. **38** (2003) 89-92.

[2.10] Mizutani A. and Nishi. Y., Mater. Trans. **44** (2003) 1857-1860.

[2.11] Takei H., Iwata K., Salvia M., Vautrin A. and Nishi. Y., Mater. Trans. **51** (2010) 2259-2265.

[2.12] Ohnishi S., Ikeda Y., Kashiwagi M. and Nitta I., Polymer **2** (1961) 119-141.

[2.13] Christenhusz R. and Reimer L., Z. Angew. Phys. **23** (1967) 396-404.

[2.14] Libby W., Anal. Chem., **19** (1947) 2-6.

[2.15] Nishi Y. and Salvia M., Mater. Trans., **47** (2006) 2846-2851.

[2.16] Splett J., Iyer H., Wang C. and McCowan C., National Institute of Standards and Technology (NIST) Recommended Practice Guide, Comparing Uncertainty for Charpy Impact Test Machine Test Results; Special publication 960-18, US Department of Commerce Boulder, Colorado (2008) pp. 2729.

[2.17] Nishida T. and Yasuda E., Evaluation of Dynamic Properties of Ceramics (Ceramics no rikigaku tokusei hyouka in Japanese), (Nikkan Kogaku Shimbun Sha, Tokyo, 1986) pp. 5051.

[2.18] Sato H., Inoue Y., Iwata K., Tonegawa A. and Nishi Y., J. Jpn. Inst. Met. **72** (2008) 520-525.

[2.19] Sato N., Kurauchi T., Sato S. and Kamigaito O., J. J. Mater. Sci. Lett. **2** (1983) 188.

[2.20] Thomason J., Composites **A39** (2008) 1732-1738.

[2.21] Faudree M., Nishi Y. and Gruskiewicz M., Mater. Trans. **54** (2013) 1877-1883.

Chapter 3

Compression-molded BMCs: Improving Charpy impact value of short glass fiber (GFRP) samples by increasing solidification texture angle, θ_t

ABSTRACT

In the compression-molded GFRP-BMC mother panels, when increasing the solidification texture angle with respect to specimen length direction, θ_t from 17.5 to 68 deg was found to raise the statistically lowest impact value (a_s) used in quality control for safety and reliability of parts 101%. Moreover, the increase from 17.5 to 68 deg apparently increased Charpy impact value, a_{uc} 34% at mid-fracture probability calculated by the median-rank method ($P_f = 0.50$). Likewise, in the typically weaker center panel sections that have random solidification texture angle distribution from 0 to 90 deg, the increased θ_t to 68 deg raised the a_{uc} 50% at mid- $P_f = 0.50$. In both cases, the a_{uc} was increased at all P_f. In addition, the 2-parameter Weibull coefficient (n) was increased 47% by increasing texture angle, θ_t from 17.5 to 68 deg. SEM revealed glass fibers in the 68 deg samples had higher density and aligned orientation.

3.1 Results
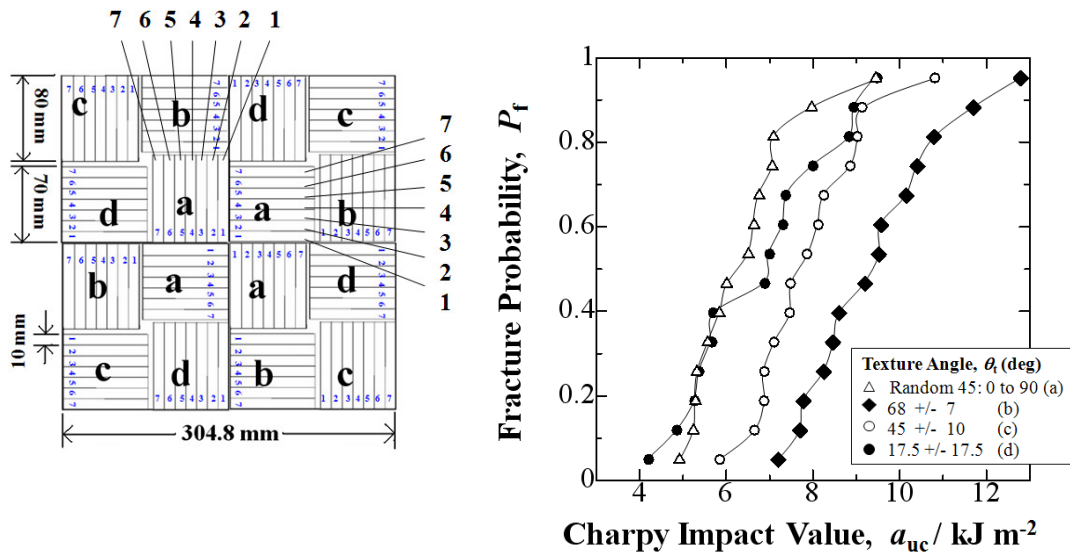**3.1.1 Effect of texture angle on Charpy impact strength**

Fig. 3.1 Sub-quadrants a, b, c, d in compression-molded panel [3.1].

Fig. 3.2 Charpy impact values (a_{uc}) vs. fracture probabilities, P_f for compression molded BMC panels as a function of solidification texture angle, θ_t, between mold flow and longitudinal direction of testing sample (corresponding to sections a,b,c and d, respectively).

To characterize resistance to impact by possible birdstrike, hailstone or volcanic rock, impact strength, a_{uc} (kJm^{-2}) of GFRP-BMC panels were evaluated at different solidification texture angles, θ_t (deg) in Figure 3.1 (Fig. 2.3) for convenience here to determine strength on position and flow behavior in the BMC panel. Figure 3.2 shows location of specimens in sections 'a', 'b', 'c', and 'd' whose texture angle is described in Chapter 2.

Fig. 3.1 shows the experimental a_{uc} values where the Charpy impact value was increased with increasing texture angle. Each data set goes from the strongest to the

47

weakest sample. Fracture probabilities, P_f are calculated by the median-rank method, a statistical analysis often applied for quality control (QC) in industry described in Chapter 2 and referenced in this chapter [3.2, 3.3, 3.4].

Increasing θ_t from 17.5 to 68 deg increased the Charpy impact value at mid-fracture probability ($P_f = 0.50$) 34% from 6.96 to 9.36 kJm^{-2}. Moreover, in the typically weaker center section (section-a) of the mother panels that have random solidification texture angle distribution from 0 to 90 deg, the increased θ_t to 68 deg raised the a_{uc} 50% from 6.25 to the 9.36 kJm^{-2} at mid- $P_f = 0.50$.

Fig. 3.1 shows the impact values of the 68 deg samples were increased at all fracture probabilities, P_f over the lower angle (45 and 17.5 deg) and random samples. In addition, impact values of the 45+/-10 deg samples were increased at all P_f over the 17.5 deg and random samples. The 17.5 deg samples had slightly higher impact values than the random samples at low- $P_f < 0.20$ and all $P_f > 0.40$ except for the strongest sample at $P_f = 0.95$ where their impact vales were about equal.
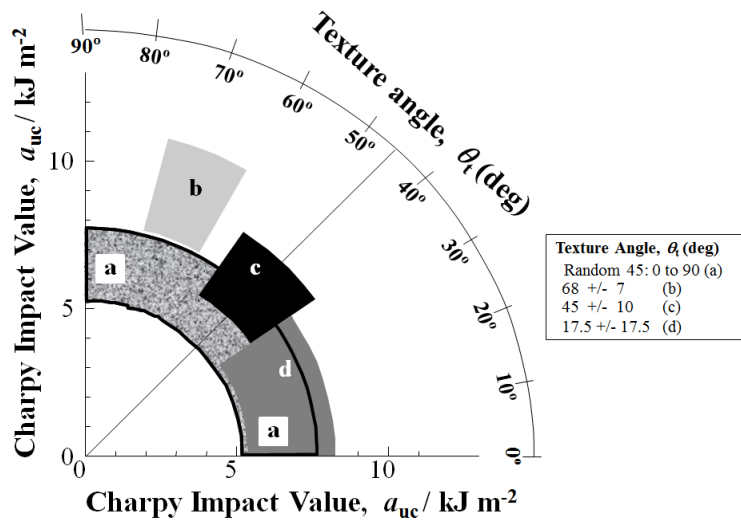
3.1.2 New circular plot

Fig. 3.3 Circular plot of Charpy impact value (a_{uc}) data spanning the angle ranges from Fig. 3.2. The upper and lower a_{uc} values are standard deviations.

Figure 3.3 shows a circular plot I thought of by the rounded architecture of Building 1 at Tokai University. Charpy impact values are depicted as arcs whose centers are the average a_{uc} spanning their standard deviations for samples of each texture angle. You can see the clear trend: a_{uc} is increased as texture angle is increased from sections d ➔ c ➔ b. The random a-section specimens span the entire 0 to 90 deg range. Average a_{uc} were 9.43, 7.89 and 6.78 and 6.41 kJm^{-2} for θ_t of 68, 45, 17.5 deg and random samples, respectively. The increase in θ_t from 17.5 to 68 deg raised the average a_{uc} 39%. Moreover, he increase in θ_t from random to 68 deg raised the average a_{uc} 50%. This type of plot may be useful to describe other types of phenomena.

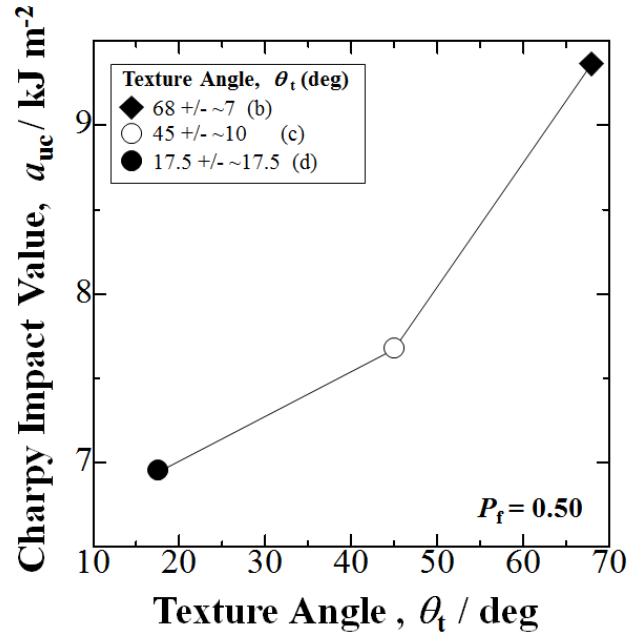### 3.1.3 Improvement at mid-fracture probability, $P_f = 0.50$

Fig. 3.4 Charpy impact values (a_{uc}) at $P_f = 0.50$ for θ_t. Although the section-a samples have mean texture angle of 45 deg, they were not included due to their random nature.
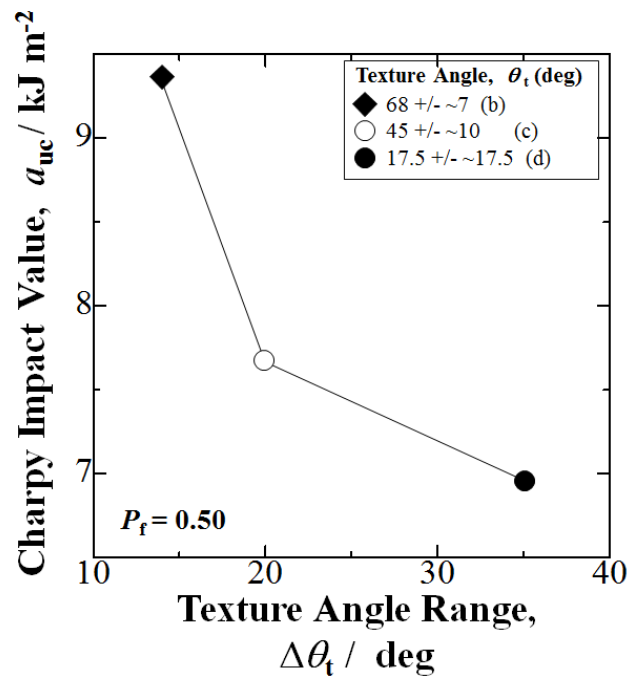

Fig. 3.5 Charpy impact values (a_{uc}) at $P_f = 0.50$ for texture angle range $\Delta\theta_t$. The random a-section sample is not included.

   Figures 3.4 and 3.5 show the increase in impact value with increasing texture angle and decreasing texture angle range more clearly. Section-a samples were not included due to their random texture flow structure.

3.2 Discussion
3.2.1 Weibull analysis: 2-parameter

The 2–parameter Weibull coefficient (n) is one of the standard parameters to compare with other structural materials [3.3] and is often used in quality control (QC). When a_{uc} is the measured Charpy impact value and is a constant, the fracture probability (P_f) as a function of risk of rupture (a_{uc}/a_o) is expressed by the following equation [3.5]:

$$P_f = 1 - \exp[-(a_{uc}/a_o)^n] \tag{3.1}$$

The linear relationship can be obtained by the following equation:

$$\ln[-\ln(1 - P_f)] = n\ln a_{uc} - n\ln a_o \tag{3.2}$$

Slopes of Weibull coefficients, n are shown in Figures 3.6 and 3.7. Increasing texture angle, θ_t from 17.5 to 68 deg raised the Weibull coefficient 47% from 4.50 to 6.61; and by increasing θ_t from 17.5 to 45+/-10 n was raised 55% from 4.50 to 6.96. Interestingly the random samples had a comparatively decent n value at 5.81 indicating the weak a-sections have decent reliability of part strength. Fig. 3.7 shows overall, as texture angle range ($\Delta\theta_t$) was decreased the n value increased. This is expected since a more ordered flow structure will increase part consistency and reliability.
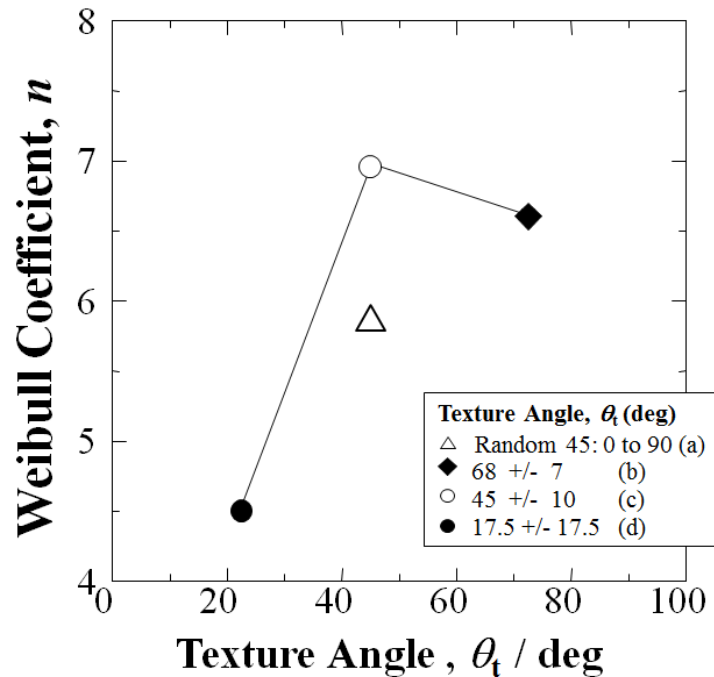

Fig. 3.6 2-parameter Weibull coefficient, n vs. texture angle. The random section-a is included.
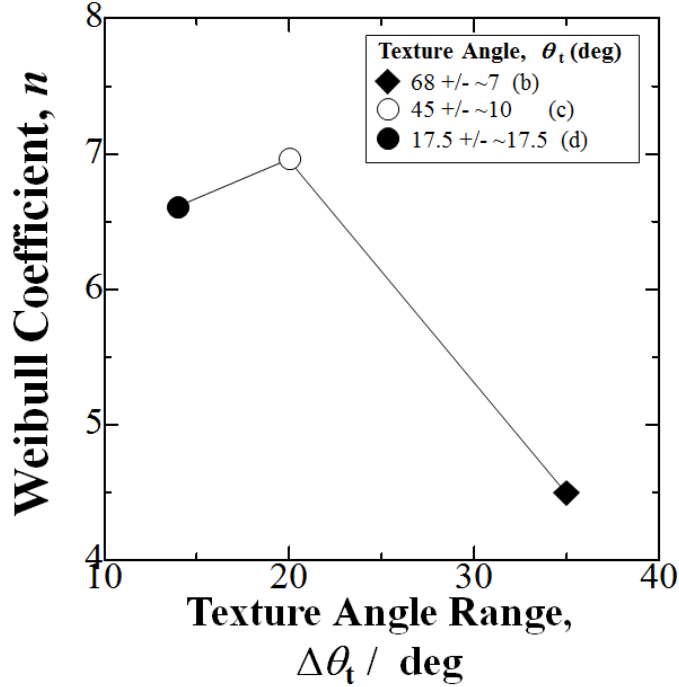
Fig. 3.7 2-parameter Weibull coefficient, *n* vs. texture angle. range. The random section-a is not included.

3.2.2 Weibull analysis: 3-parameter: Improvement in statistically lowest impact value, a_s by increasing texture angle

Three-parameter Weibull analysis yields the statistically lowest impact value, a_s (kJm^{-2}) at $P_f = 0$ for a given data set.   Therefore, it is useful for quality control of mass produced parts. If the statistical equation is assumed to be applicable to the measured a_{uc} value, the P_f depends on the risk of rupture [3.3, 3.6]. In predicting the required value for a new structural material, the a_s, the coefficient, *m* and constant (a_{III}) are key parameters. The equation is:

$$P_f = 1 - \exp[-([a_{uc} - as]/a_{III})^m] \qquad (3.3)$$

Figure 3.8 shows the plots for the linear form. As shown in Figure 3.9 when the linear form of eq. (3.3) is iterated for the highest correlation coefficient, *F*, the a_s is obtained.
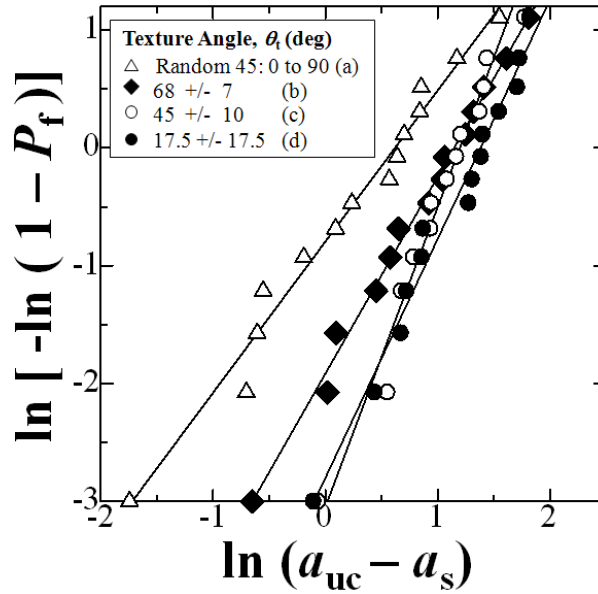
Fig. 3.8 Plot of $\ln[-\ln(1 - P_f)]$ vs. $\ln(a_{uc} - a_s)$ of 3-parameter Weibull equation.
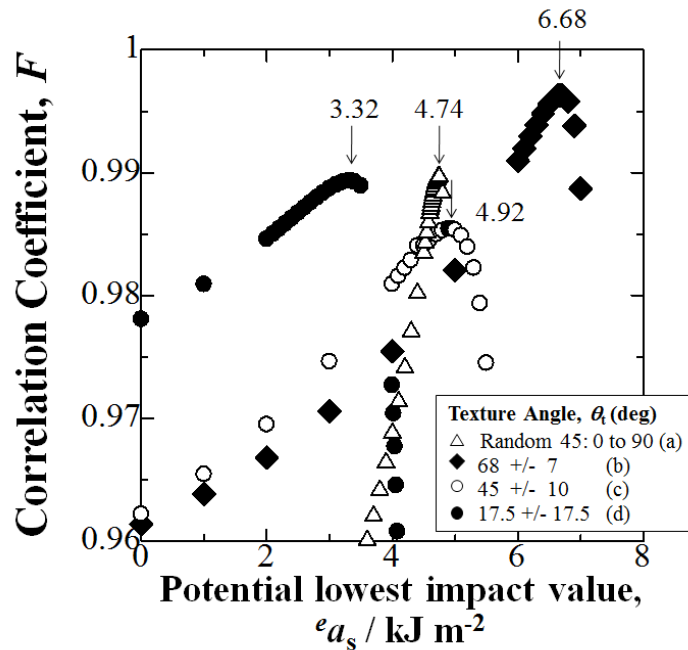

Fig. 3.9 Changes in correlation coefficient (F) versus potential a_s value ($^e a_s$) for $P_f = 0$. The lowest impact value (a_s) was determined at maximum F.

Figs. 3.8 and 3.9 show the results of the 3-parameter Weibull analysis, i.e. the improvement in statistically lowest impact value, a_s at fracture probability, $P_f = 0$ by increasing texture angle. Mainly, increasing the texture angle from 17.5 to 68 deg raised the lowest impact value a_s 101% from 3.32 to 6.68 kJm^{-2}. In addition, there was a 41% increase in a_s by increasing texture angle from the random 45 to 68 deg. This data indicates part safety and reliability enhancement is possible.

52

3.2.3 SEM of 'a' and 'b' sections

θ_t = Random: 0 to 90 deg (a-section)
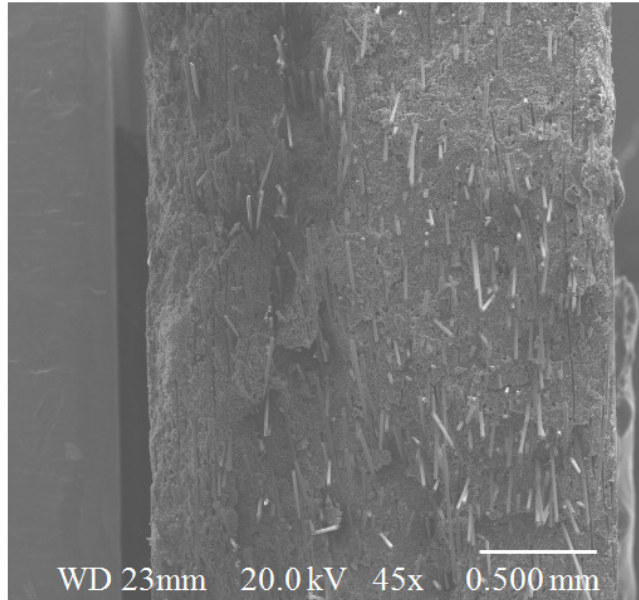a_{uc} = 6.01 kJm^{-2} P_f = 0.47

Fig. 3.10 SEM photomicrograph of fracture surface from Charpy impact test. Specimen texture angle is Random: 0 to 90 deg (a-section).

θ_t = 68 +/- 7 deg (b-section)
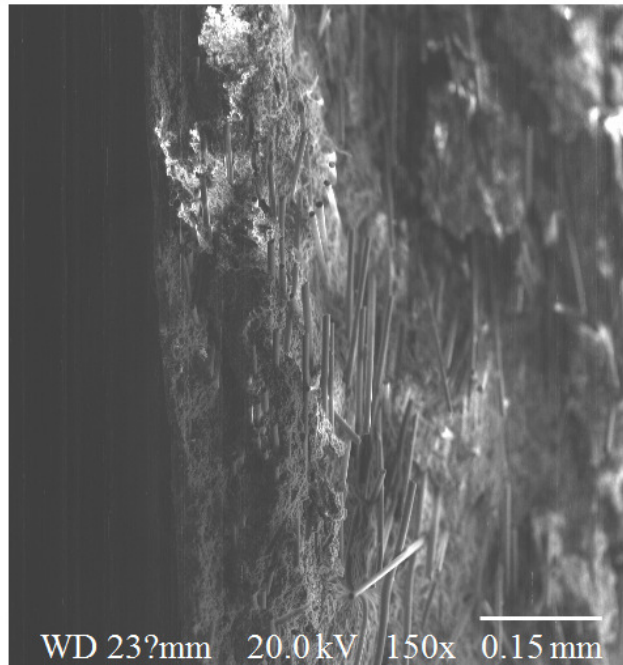a_{uc} = 9.20 kJm^{-2} P_f = 0.47

Fig. 3.11 SEM photomicrograph of fracture surface from Charpy impact test. Specimen texture angle is 68 +/-7 deg (b-section).

To assess damage mechanism, SEM photomicrographs were taken of fracture surfaces of the Charpy impact samples from the strongest (b-section) and weakest (a-section) data sets.

Figure 3.10 shows a low density of fibers at random angles normal to the fracture surface in the a-sections (θ_t = Random 0 to 90 deg). In comparison, Figure 3.11 shows a higher density of fibers aligned perpendicular to the specimen length in the b-sections (θ_t = 68 +/- 7 deg). This is evidence that fibers flow more parallel to the outward radial flow direction during compression molding in the 68 deg samples. Both SEM photos were taken of samples at mid-P_f = 0.47 where a_{uc} of the random, and 68 deg samples were 6.01 and 9.20 kJm-2, respectively. The increased θ_t from random (45 deg) to 68 deg raised the a_{uc} 50% at mid- P_f = 0.50.

It may be possible to adjust for the maximum solidification texture angle for the strongest specimens. The paste starts out as a charge in the center of the square panel mold. As the paste is compressed, it flows approximately radially outward from the center to the mold edges where fibers are pushed in the radial direction at the flow front with possible backflow and increased fiber concentration at the mold edges. The flow front itself may have a higher concentration of fibers. This is supported by specimen 7 at the panel edge in the b and c-sections (Fig. 3.1) often having higher impact values than specimens 1 - 6. The higher fiber density along with higher fiber alignment orientation in the b-sections appeared to raise the impact values.

3.3 Conclusions

1) In the compression molded GFRP-BMC mother panels, when increasing the solidification texture angle, θ_t with respect to specimen length direction, θ_t from 17.5 to 68 deg was found to apparently raise the statistically lowest impact value (a_s) used for quality control 101%.

2) Moreover, the increase in θ_t from: [Random 0 to 90 deg] and [17.5 deg] to 68 deg evidently increased Charpy impact value, a_{uc} 50% and 34%, respectively at mid-fracture probability (P_f = 0.50) calculated by the median-rank method. Furthermore, a_{uc} was increased at all P_f with increasing θ_t = 17.5 ➔ 45 ➔ 68 deg.

3) Results of this data indicate increased reliability and safety in space, aircraft and sports applications.

REFERENCES

[3.1] Faudree M., Nishi Y. and Gruskiewicz M., Mater. Trans. **53** (2012) 1412-2310.

[3.2] JIS K 7077 (1991).

[3.3] Nishi Y. and Salvia M., Mater. Trans., **47** (2006) 2846-2851.

[3.4] Nishida T. and Yasuda E., Evaluation of Dynamic Properties of Ceramics (Ceramics no rikigaku tokusei hyouka in Japanese), (Nikkan Kogaku Shimbun Sha, Tokyo, 1986) pp. 5051.

[3.5] Weibull W., Ingeniörs vetenskaps aka akademien, nr. 151 (Generalstabens litografiska anstalts förlag, Stockholm, 1939) pp. 1214.

[3.6] Nishi Y., Kobayashi H. and Salvia M., Mater. Trans. **48** (2007) 1924-1927.

Chapter 4

Compression-molded BMCs: Improving Charpy Impact value and bending modulus of short glass fiber reinforced polymer bulk molding compound (SGFRP-BMC) samples by homogeneous low-voltage electron beam irradiation (HLEBI)

[*Effects of Electron Beam Irradiation on Charpy Impact Value of short glass fiber (GFRP) with Random Distribution of Solidification Texture Angles from Zero to 90 Degrees*]

ABSTRACT

During manufacturing process, compression-molded short-fiber GFRP-BMC panels have random distribution of solidification texture angles from zero to 90 degrees in the center of the mother panels resulting in significantly lower impact strength in than that of the outside. On the other hand, experimental results showed homogeneous low voltage electron beam irradiation (HLEBI) applied to the center region apparently enhances the Charpy impact values (a_{uc}) 5 to 25%. Fracture mechanism was observed to convert at $a_{uc} > \sim5.4 \sim 6.7$ kJm^{-2} from clean to secondary microcrack proliferation and/or bends near the main crack, with increasing fracture surface area as a_{uc} increased. SEM observation revealed 0.86 MGy HLEBI treated GFRP had much more polymer adhering to fibers than the untreated. This increased matrix adhesion can be explained by electron spin resonance (ESR) peaks indicating dangling bonds are generated creating repulsive forces between outer shell electrons in the polymer matrix, apparently exhibiting increased compressive stress on the fibers increasing adhesion force. Moreover, the lone pair electrons generated in the matrix may have bonded with the fibers more efficiently. In addition, HLEBI improves the Charpy impact value and lowest impact value for quality control 64% of samples with solidification texture angle, $\theta_t = 45+/-10$ deg (c-sections) at the outside corners of the mother panel. These results show applying HLEBI to aircraft, automobile, sports and other short fiber GFRP-BMC components can have benefit in industry.

4.1 Introduction

In the center a-sections of the compression-molded panels (see Chapter 2), the impact values are much lower (10 to 70%) than the outer sections b,c,d [4.1] due to highly turbulent flow and a slower onset of cure where chains probably have a harder time moving to different configurations. Hence, to increase the impact strength, effects of EB-irradiation were investigated for samples of section-a (Fig. 2.3 thick lines).
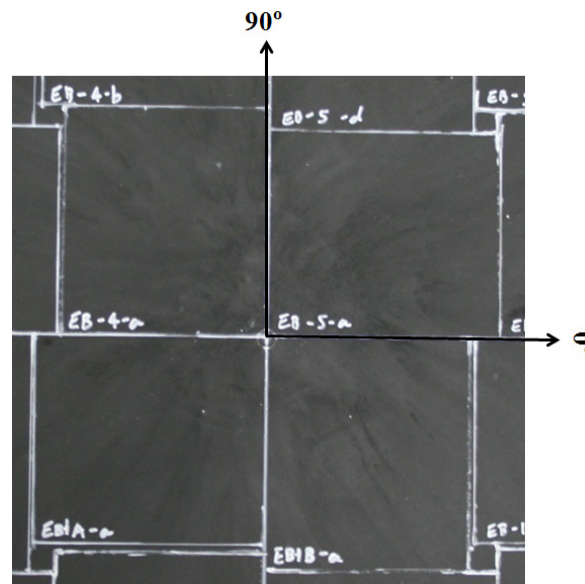

Fig. 4.1 Photograph of GFRP panel a-sections showing typical mold flow pattern.

Figure 4.1 shows the center section-a where the charge of paste is first compressed characterized by rough texture with weak resin-rich areas, anisotropy of fiber and filler density gradients that exhibit high flaw sensitivity. This anisotropy can result in higher variance in impact values of section-a from panel-to-panel and at different areas within each panel. Given these conditions, it is important to strengthen parts in space vehicles, aircraft, automobiles and electrical housing that can be exposed to outside environments to withstand possible impacts and maintain long use life.

4.1.1 Charpy impact test of center a-sections

To evaluate dynamic fracture toughness, Charpy impact values for GFRP samples from the center a-sections (Figs. 2.2, 2.3 and 4.1) with and without HLEBI were measured. Concerning variability in the a-sections, Charpy impact tests were conducted according to two data sets as shown in Table 4.1, where each 7-letter group represents specimens 1 – 7 in Fig. 2.3 and symbols 'A', 'α', and 'a' are 0.86, 0.30 EB irradiated, and untreated samples, respectively. In Data Set 1 (uniform) all specimens 1 – 7 are given the same treatment. In Data Set 2 (alternating) specimens are given alternating treatments, for example in the first line 1,3,5,7 are untreated and 2,4,6 are EB irradiated.

Table 4.1 Designation of the two data sets.

Data set 1		Data set 2	
aaaaaaa	aaaaaaa	aAaAaAa	AaAaAaA
ααααααα	ααααααα	AaAaAaA	aAaAaAa
AAAAAAA	AAAAAAA	aAaAaAa	

4.2 Results: center a-sections (θ_t = random 0 to 90 deg)
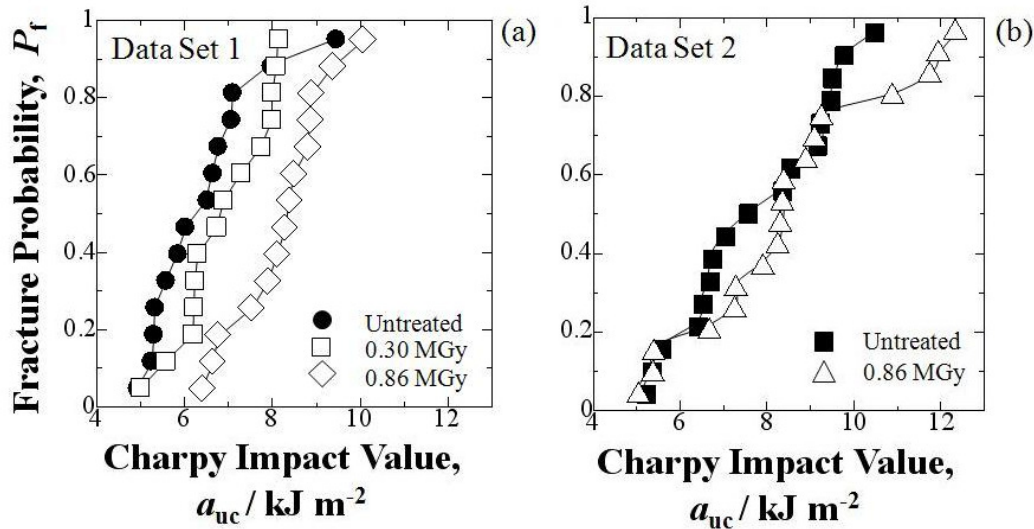### 4.2.1 Effect of HLEBI on impact values, a_{uc}: Data Set 1

Fig. 4.2 Relationships between Charpy impact value and fracture probability at each EB irradiation dose for GFRP a-sections for Data Set 1 (a) and Data Set 2 (b) [4.1].

Experimental results from Data Set 1 in Figure 4.2 (a), show applying 0.86 and 0.30 MGy HLEBI apparently enhances the Charpy impact values (a_{uc}) of the GFRP near the center of the mother panel (a-sections) at all fracture probabilities (P_f) except in one sample where the high P_f of 0.94 (9.45 kJm^{-2}) was higher than that of the 0.30 MGy. Moreover, HLEBI apparently enhanced a_{uc} 33% and 8.7% at mid-fracture probability ($P_f = 0.50$) at 0.86 (8.33 kJm^{-2}) and 0.30 (6.81 kJm^{-2}) MGy over the untreated (6.26 kJm^{-2}).

Moreover, in Data Set 1 HLEBI of both 0.86 and 0.30 MGy doses apparently raises the average $\underline{a_{uc}}$ (8.17 and 6.88 kJm^{-2}, respectively) of the GFRP 27.5% and 7.3%, over the untreated samples (6.41 kJm^{-2}). Standard deviations are 1.06 (13%), 1.02 (14.8%), and 1.24 (19.3%) kJm^{-2}, for the 0.86, 0.30 MGy EB, and untreated samples, respectively. EB at the additional dose of 0.86 MGy results in the lowest standard deviation of the Data Set 1.

4.2.2 Effect of HLEBI on impact values, a_{uc}: Data Set 2

Experimental results from Data Set 2 in Figure 4.2 (b), show although HLEBI does not readily enhance the a_{uc} from $P_f = 0$ to 0.2 and 0.55 to 0.75, the 0.86 MGy HLEBI apparently enhances a_{uc} remarkably at the high values of $P_f = 0.79$ from 9.48 to 10.88 kJm^{-2}, to $P_f = 0.96$ from 10.49 to 12.33 kJm^{-2}, and slightly at the mid- P_f from 7.58 to 8.33 kJm^{-2}. From the Data Set 2, 0.86 MGy HLEBI apparently improved a_{uc} 9.9% at mid-fracture probability ($P_f = 0.50$) (8.33 kJm^{-2}) over the untreated (7.58 kJm^{-2}), although not as high as the Data Set 1 enhancement.

For Data Set 2, HLEBI of 0.86 MGy dose apparently raises the average a_{uc} (8.57 kJm^{-2}) of the GFRP 10.5%, over the untreated samples (7.75 kJm^{-2}). Although standard deviations are higher for the 0.86 MGy irradiated samples 2.22 (25.9%), than the untreated 1.69 (21.7%) kJm^{-2}, HLEBI raises the average a_{uc}.

4.2.3 Data Sets 1 and 2 combined

For both Data Sets 1 and 2 combined average a_{uc} is 8.33 (1.77) and 7.15 (1.63) kJm^{-2} (standard deviations in brackets) for the 0.86 MGy EB and untreated samples, respectively with a 16.7% increase by the HLEBI.

4.2.4 Effect of random solidification texture of untreated samples

Figs. 4.2 (a) and (b) show the a_{uc} of the untreated samples taken from the center a-sections of the two Data Sets, 1 and 2. The Data Set 1 had significantly lower average a_{uc} (6.41kJm^{-2}) than Data Set 2 (7.75 kJm^{-2}) for untreated samples. Since there is a highly random distribution of solidification texture angles from zero to 90 degrees in the a-sections, the high difference in average a_{uc} can be explained. The a_{uc} difference is an affect of the anisotropy, rather than difference between uniform and alternating samples of the two data sets.

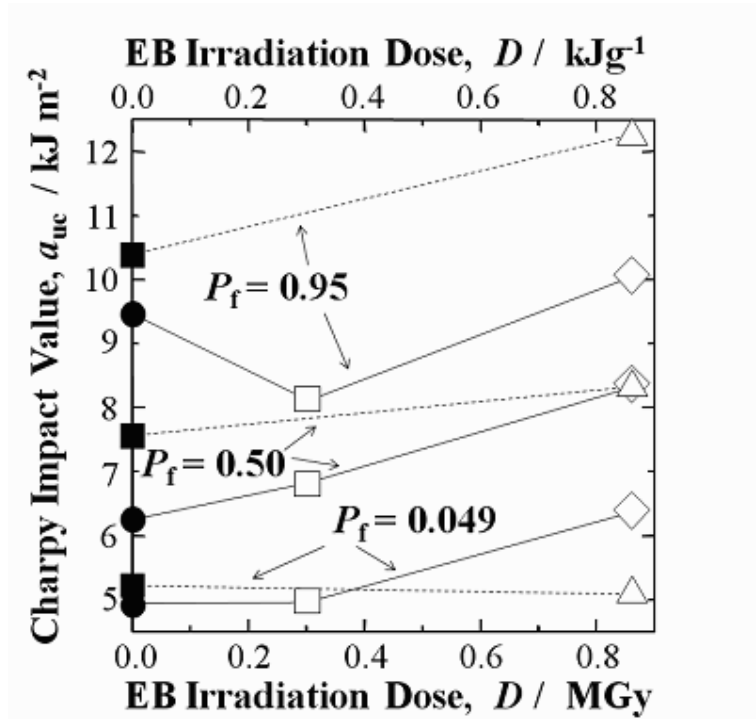**4.2.5 Effect of HLEBI at each fracture probability, P_f**

Fig. 4.3 Effect of EB irradiation dose on experimental impact values (a_{uc}) at low (P_f = 0.049), mid- (0.50) and high (0.95) fracture probabilities of GFRP-BMC samples from Data Set 1 (solid lines) and 2 (dotted lines).

Figure 4.3 shows effect of EB irradiation dose on experimental impact values (a_{uc}) from Fig. 4.2 at low (P_f = 0.049), mid- (0.50) and high (0.95) fracture probabilities of GFRP-BMC samples from Data Set 1 (solid lines) and 2 (dotted lines). Overall, applying HLEBI at the higher dose of 0.86 MGy increases the a_{uc} of the GFRP samples at all fracture probabilities with the exception of Data Set 2 at P_f = 0.049. Although a_{uc} at the highest experimental fracture probability of P_f = 0.95 is reduced from 9.45 to 8.14 kJm^{-2} by the 0.30 MGy EB in Data Set 1, the 0.86 MGy irradiation increases the a_{uc} from 9.45 to 10.05 kJm^{-2} in Data Set 1 and from 10.49 to 12.31 in Data Set 2.

4.3 Discussion
4.3.1 Effect of HLEBI on Weibull analysis of impact values
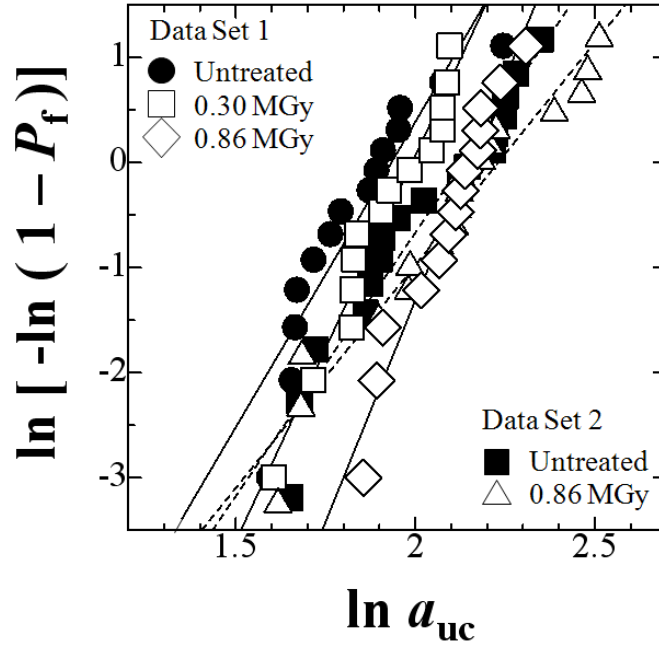

Fig. 4.4 Weibull plots of GFRP irradiated by electron beam at each dose for Data Set 1 (solid lines) and 2 (dotted lines).

The Weibull coefficient (n) is one of the standard and traditional factors to compare with many other structural materials [4.2]. When a_{uc} and a_o are the measured Charpy impact value and a constant, the fracture probability (P_f) as a function of risk of rupture (a_{uc}/a_o) is expressed by eq. (4.1) [4.3]:

$$P_f = 1 - \exp[- (a_{uc}/a_o)^n] \qquad (4.1)$$

where n is the 2-dimensional Weibull coefficient. The linear relationship is expressed as the following equation.

$$\ln[-\ln(1 - P_f)] = n\ln a_{uc} - \ln a_o \qquad (4.2)$$

Figure 4.4 shows the resulting Weibull plots for each EB irradiation level and untreated for Data Sets 1 and 2. The n value corresponds to the slopes of the Weibull plot relations. Figure 4.5 shows the n obtained for each irradiation dose. In Data Set 1, the EB irradiations of 0.30 and 0.86 MGy raised the Weibull coefficient from 5.81 (untreated) to 7.33 and 8.43, respectively. Although, in Data Set 2 the Weibull coefficient was reduced from 5.01 to 4.24 by the 0.86 MGy EB, the impact values were increased 9.9%.
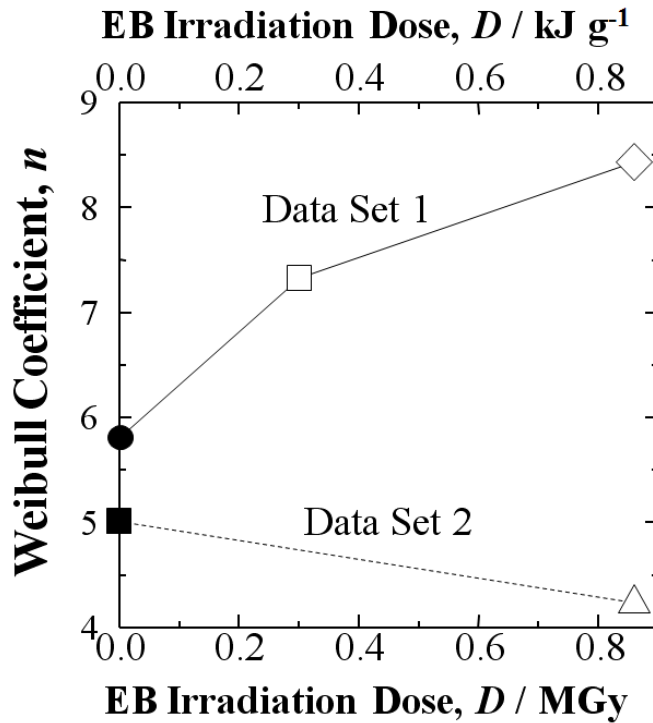
Fig. 4.5 Changes in Weibull coefficient (n) versus EB irradiation dosages.

   The differences in n for Data Sets 1 and 2 are probably due to rough texture with weak resin-rich areas, and anisotropy of fiber and filler density gradients. Thus, the high variance in impact values of section-a from panel-to-panel and at different areas within each panel can be explained. Overcoming this, the impact values are apparently raised by applying HLEBI of 0.86 MGy.

4.3.2   Electron spin resonance (ESR) signals
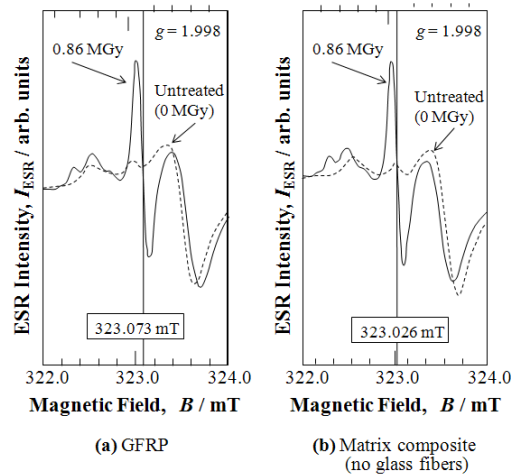
Fig. 4.6 ESR signals of GFRP (a) and matrix composite (b), respectively before (dotted line) and after 0.86 MGy (solid line) HLEBI.

Figure 4.6 shows HLEBI produces detectable ESR signals in the GFRP (a) and matrix composite without fibers (b). In both cases, a signal peak is generated from 0.86 MGy EB (solid line). In contrast, no sharp peak is observed in the untreated GFRP samples (dotted line) [4.1]. For the GFRP and matrix composite the signal peaks are generated at inflection points of 323.073 and 323.026 mT, respectively, indicating an increase in unpaired electrons in the EB irradiated GFRP-BMC, which are probably dangling bonds. ESR signals of the GFRP and matrix composite are similar in shape and magnetic field value, thus it is possible the dangling bonds observed are from the polyester styrene- butadiene polymer.

The signal magnetic fields, B of 323.073 and 323.026 mT correspond closely to that of studies of Si-glass network (323.7 mT, g-factor = 2.001) [4.4] and close to EB-irradiated polypropylene (PP) film at 321-322 mT, polydimethylsiloxane (PDMS) at 322.7 mT [4.5], and novolak-type phenol resin at 322.8 mT [4.6]. Therefore, dangling bonds are detected in the polymer.

Upfield between 323.4 and 324 mT, there is a dip in the signal which is the same in both untreated and treated samples so is not considered to be dangling bonds.
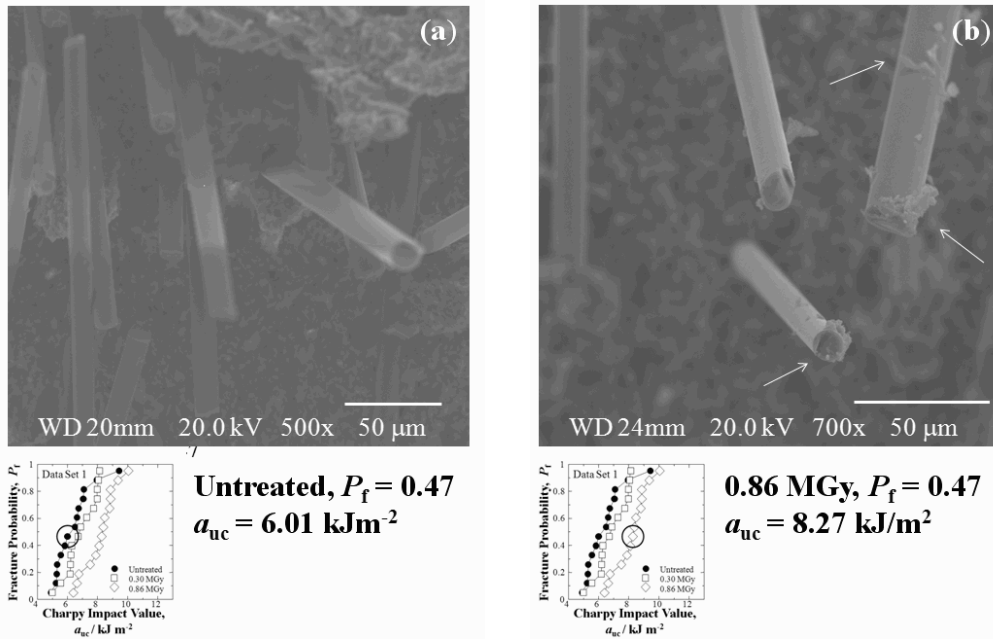
4.3.3   SEM results

Fig. 4.7 SEM micrograph showing untreated GFRP (a) and 0.86 MGy HLEBI treated (b) having more polymer adhering to glass fibers (arrows) than the untreated.
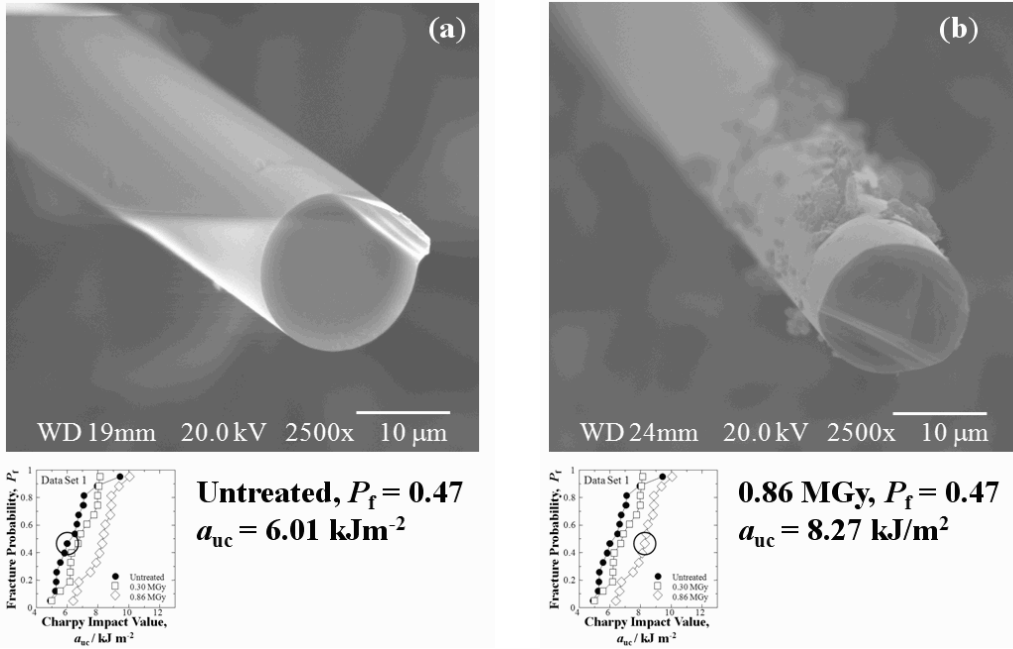
Fig. 4.8 SEM micrograph at high magnification of single fibers showing untreated GFRP (a) and 0.86 MGy HLEBI treated (b) having more polymer adhering to a fiber than the untreated.

SEM observation of entire fracture surfaces seem to show 0.86 MGy HLEBI treated GFRP has much more polymer adhering to the glass fibers than the untreated although very little is observed in the untreated. Figures 4.7 and 4.8 show SEM of fracture surfaces for the untreated (a) and 0.86 MGy treated (b) samples at lower and higher magnifications, respectively, showing the 0.86 MGy HLEBI treated GFRP has more polymer adhering to fibers (arrows) than the untreated. Figs. 4.7 and 4.8 show fracture surfaces of two Data Set 1 samples selected at $P_f = 0.47$, the most improvement in a_{uc} (a_{uc} = 6.01 and 8.27 kJm^{-2} for untreated and 0.86 MGy, respectively). SEM observations of two additional fracture surfaces of Data Set 2 selected at $P_f = 0.96$ (a_{uc} = 10.49 and 12.33 kJm^{-2} for untreated and 0.86 MGy, respectively) yield the same results. SEM observation shows the increased fiber-matrix adhesion seen in the 0.86 MGy samples appears to assist for more internal matrix cracking, or more energy for a higher a_{uc}. Since the fibers get stronger adhesion along the sides, the composite structure is held together more efficiently, hence cracks have to twist and branch out avoiding the compressive sites increasing impact resistance.

This increased matrix adhesion can be further explained by the ESR peaks (Fig. 4.6), where dangling bonds are generated creating repulsive forces between outer shell electrons in the polymer matrix. The matrix would therefore, impart increased compressive stress on the fibers increasing adhesion force. Moreover, the lone pair electrons in the matrix may bond with the fibers more efficiently.

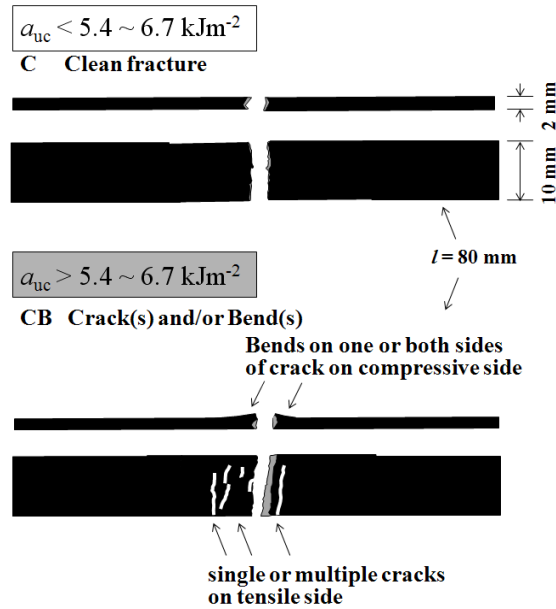## 4.3.4 Effect of HLEBI on fracture mechanism

Fig. 4.9 Illustration showing dominant fracture mechanisms of the GFRP undergoing impact tests were a clean fracture (C) for samples with $a_{uc} < 5.4 \sim 6.7$ kJm^{-2}; and single or multiple bends or cracks (CB) for samples with $a_{uc} > 5.4 \sim 6.7$ kJm^{-2}. The trend followed independent of EB dose or untreated.

Furthermore, while all Charpy impact specimens fracture completely, as a_{uc} increases fracture surface area is observed to increase. For example, Figure 4.9 illustrates the two main fracture mechanisms for Data Sets 1 and 2 combined. At low a_{uc}, samples exhibit a clean straight fracture perpendicular to the specimen length. At $a_{uc} > \sim 5.4 \sim 6.7$ kJm^{-2} fracture mechanism is
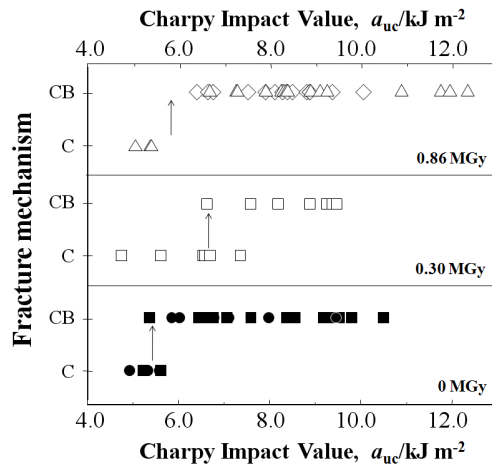

Fig. 4.10 Schematic diagram of main fracture mechanisms in Fig. 4.9 as a function of impact value for 0.86 and 0.30 MGy EB irradiated, and untreated GFRP samples for Data Sets 1 and 2 combined.

observed to transform from the clean fracture (C), to secondary microcrack proliferation and/or bends (CB) near the main crack. The microcracks, branching from or occurring ~0.5 to 3 mm from the main crack, and bends are generated on the tensile and compressive sides, respectively, and are single or multiple. The trend seems to follow independent of EB dose or untreated as shown in Figure 4.10 where conversions occur at ~5.8, 6.7, and ~5.4 kJm^{-2} for 0.86 and 0.30 MGy EB irradiated, and untreated GFRP samples, respectively. Above $a_{uc} > $ ~5.4 ~ 6.7 kJm^{-2} up to the maximum a_{uc} obtained at 12.33 kJm^{-2}, fracture surface area is observed to increase in the form of more jagged shape and increasing secondary cracks visible on the tension side. For these reasons, increased fiber-matrix adhesion seen in the 0.86 MGy samples appears to assist for more internal cracking, increasing resilience to impact of the GFRP-BMC, raising the a_{uc}.

4.3.5 Non-destructive bending test at low deformations (a-sections) to obtain Young's bending modulus, *E*

Figure 4.11 shows results of laser bending tests to obtain Young's bending modulus, *E* at extremely low deformations of compression molded panel specimens with solidification texture angle random from zero to 90 deg (a-sections). Each point is the average of tension and compression moduli using the 400g weight. Two 7-specimen quadrants of a-sections consisting of 14 specimens total were tested, however one specimen was omitted since it its width (~6.5 mm) was much smaller than the others (10 mm).

As shown in Fig. 4.11, applying the 0.30 MGy HLEBI apparently increased Young's modulus (*E*) at all cumulative probabilities (P_E). At mid- $P_E = 0.50$ the *E* was increased from 6.68 to 6.80 GPa; at the low P_E of 0.05 the *E* was raised from 6.13 to 6.49 GPa; in addition at high P_E of 0.95 the HLEBI increased the *E* from 7.17 to 7.53 GPa.
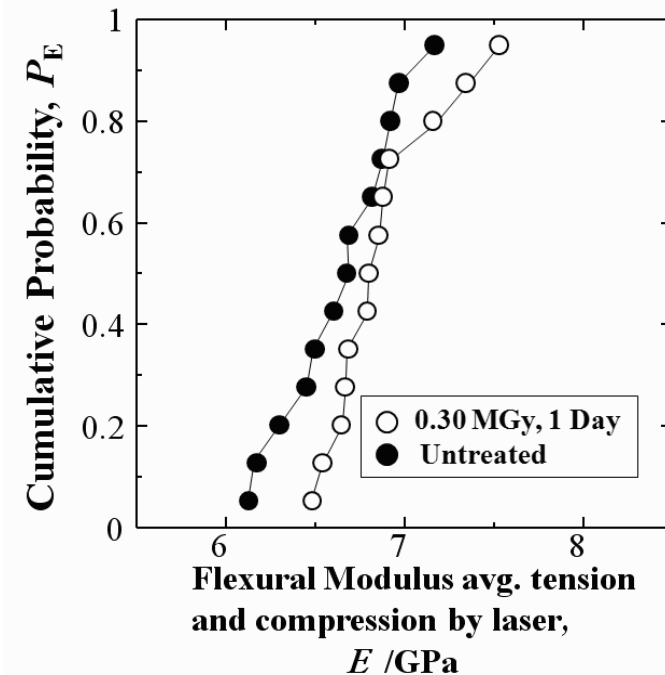

Fig. 4.11 Relationships between flexural modulus value and cumulative probability for untreated and at 0.30 MGy EB irradiation dose for GFRP a-sections.
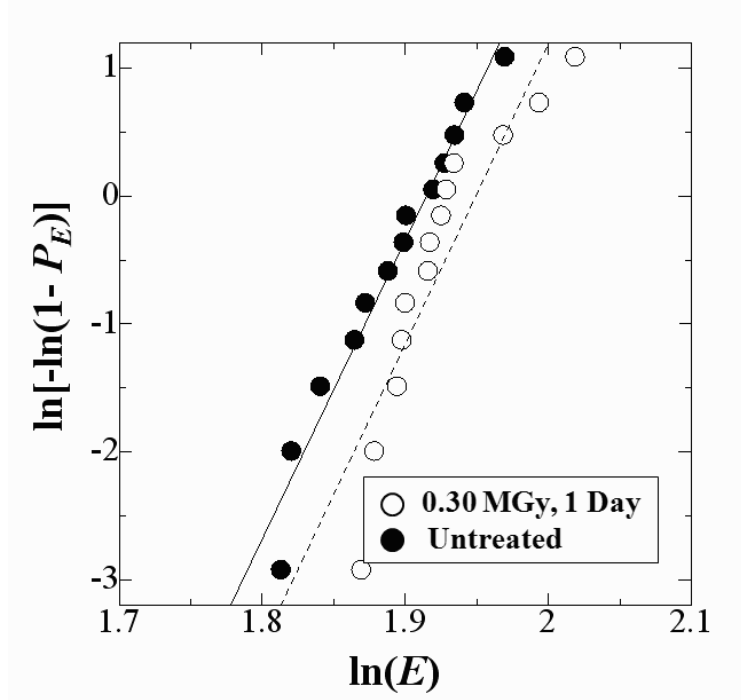
4.3.5.1 Weibull Analysis: 2-parameter

Fig. 4.12 Weibull plots of GFRP irradiated by electron beam at 0.30 MGy.

To determine consistency in Young's modulus of the manufactured parts, 2-parameter Weibull analysis was conducted. When E and E_o are the measured Young's modulus value and a constant, the cumulative probability (P_E) as a function of risk of rupture (E/E_o) is expressed by eq. (4.3) [4.3]:

$$P_E = 1 - \exp[-(E/E_o)^n] \tag{4.3}$$

where n is the 2-dimensional Weibull coefficient. The linear relationship is expressed as the following equation.

$$\ln[-\ln(1-P_E)] = n\ln E - \ln E_o \tag{4.4}$$

Figure 4.12 shows the resulting Weibull plots for data in Fig. 4.11. The n value corresponding to the slopes of the Weibull plot relations is apparently about the same for the specimens before ($n=23.36$) and after the 0.30 MGy EB dose ($n = 23.47$) showing the EB does not change the consistency.
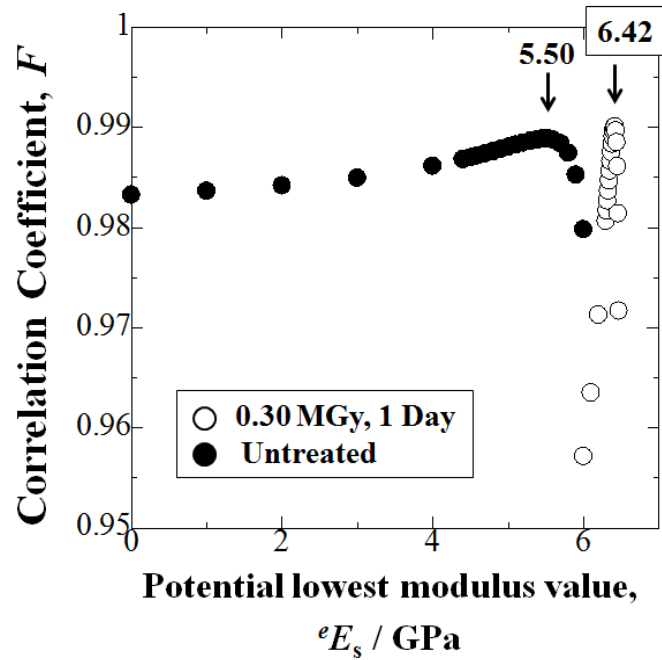
4.3.5.2 Weibull Analysis: 3-parameter

Fig. 4.13 Changes in correlation coefficient (F) versus the potential E_s value (^eE_s) for $P_E = 0$. The lowest modulus value (E_s) was determined at maximum F.

If the statistical equation is assumed to be applicable to the measured Young's modulus E, the P_E value depends on the risk of rupture, ($[E - E_s]/E_{III}$) [4.3]. The 3-dimensional Weibull equation is employed:

$$P_E = 1 - \exp[-([E - E_s]/E_{III})^m] \qquad (4.5)$$

While the E_{III} is the E value when the term ($\ln[-\ln(1 - P_E)]$) is zero, the E_s value is defined as the potential ^eE_s value when $P_E = 0$ and represents the statistically lowest possible Young's modulus for safety considerations and deems valuable for quality control (QC). The iteration is performed using the linear form of eq. (4.5) to obtain the largest correlation coefficient, F from iteration using eq. (4.6):

$$\ln[-\ln(1 - P_E)] = m\ln(E - E_s) - m\ln E_{III} \qquad (4.6)$$

Results in Figure 4.13 show applying the 0.30 MGy EB dose increases the lowest possible Young's modulus (E_s at $P_E = 0$) 17% from 5.50 to 6.42 GPa indicating the statistically weakest sample is strengthened by the EB. This shows applying the 0.30 MGy EB dose to the typically weak center a-section samples of the compression-molded GFRP-BMC can be a beneficial method to use in industry.
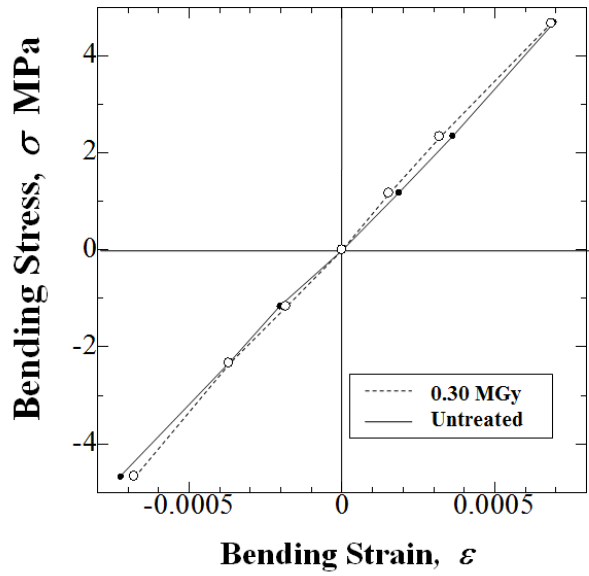
Fig. 4.14 Flexural stress-strain curves for untreated and at 0.30 MGy EB irradiation dose for GFRP a-sections.

Figure 4.14 shows the stress-strain curves by the 100, 200 and 400g weights slightly strengthens the tensile and compression Young's modulus of the a-section samples. Since the same samples were tested before and after EB, the stresses are the same. Specimen thicknesses were measured before and after EB, but no significant differences were found.
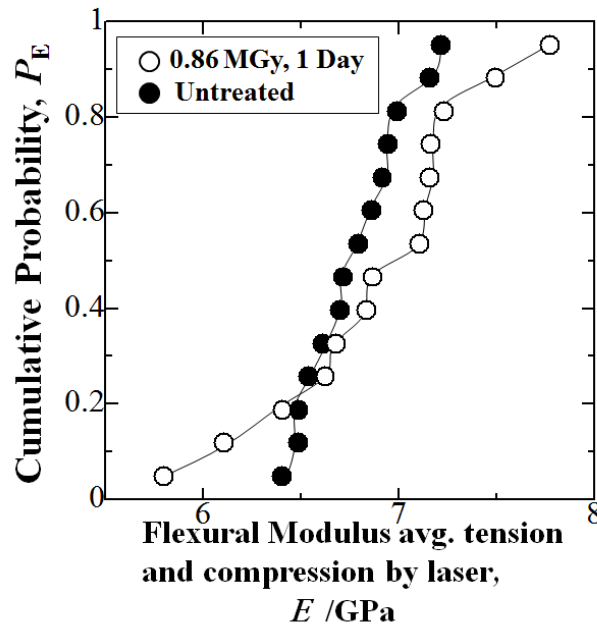

Fig. 4.15 Relationships between flexural modulus value and cumulative probability for untreated and at 0.86 MGy EB irradiation dose for GFRP a-sections.

69

Figure 4.15 shows effect of a higher HLEBI dose of 0.86 MGy on Young's modulus where the E was reduced at low $P_E < 0.25$. However, at mid- $P_E = 0.50$ the modulus was raised slightly from 6.76 to 6.92 GPa. In addition, at high $P_E = 0.95$ the modulus was raised 7.77% from 7.21 to 7.77 GPa. The stress-strain curves are shown in Figure 4.16 where the modulus was increased slightly in the compression region. Figure 4.17 shows E was increased by both the 0.30 and 0.86 MGy HLEBI dose at mid-fracture probability, $P_f = 0.50$. With the E values being reduced at low-P_E by the higher HLEBI dose of 0.86 MGy, 2 and 3-dimensional Weibull plots yielded lower values for n, m and E_s, therefore carefulness is recommended when adjusting EB dose for aircraft and other parts.
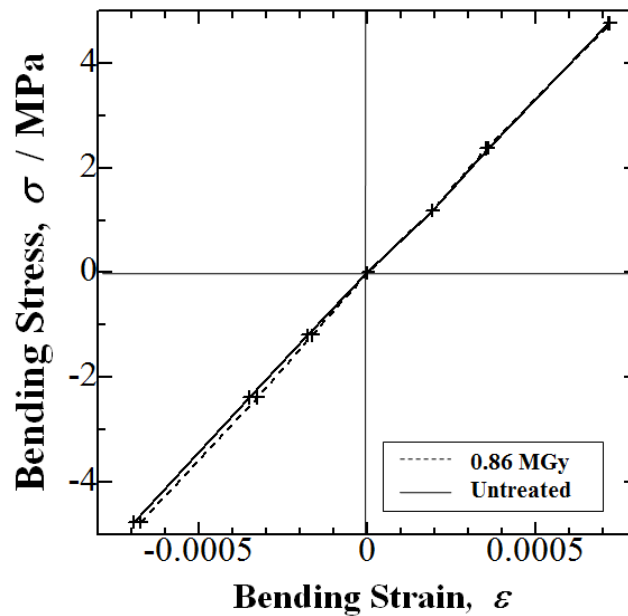

Fig. 4.16 Flexural stress-strain curves for untreated and at 0.30 MGy EB irradiation dose for GFRP a-sections.
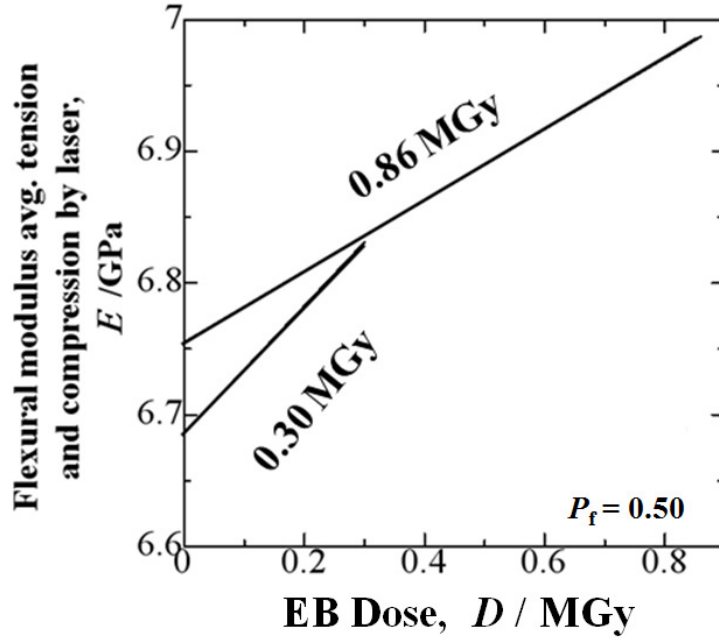
Fig 4.17 Effect of EB dose on average of tensile and compression flexural moduli (E) by 3-point bend under 400g load measured by laser. The same samples were measured before and after EB.
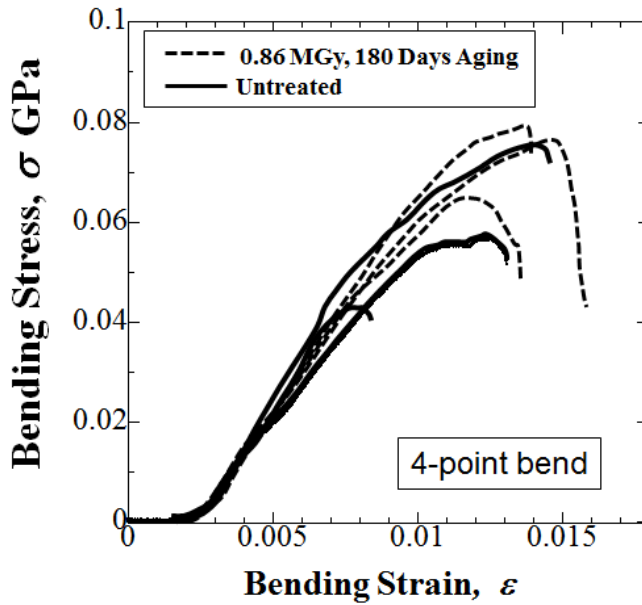
4.3.5.3 4-point bending fracture test

Fig. 4.18 Flexural stress-strain curves for untreated (solid lines) and at 0.86 MGy EB irradiation dose (after 180 days aging) (dotted lines) for GFRP a-section Charpy halves.
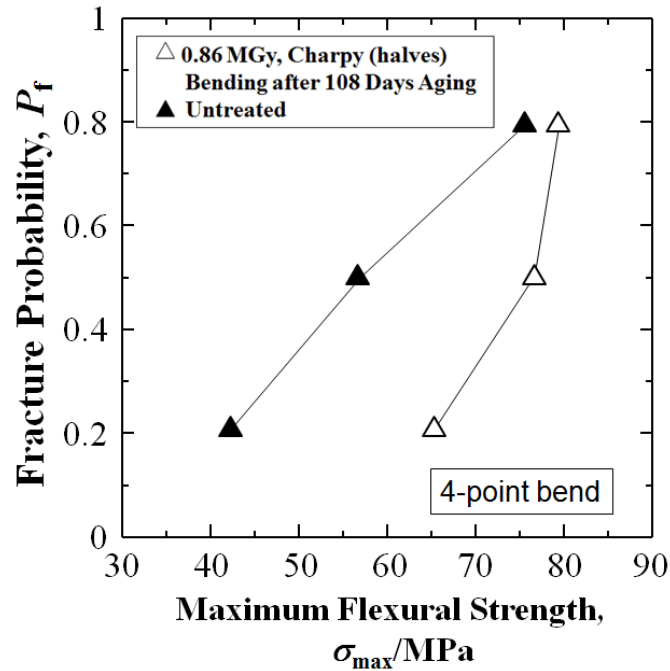
71

Fig. 4.19 Relationships between flexural strength, σ_{max} and fracture probability for untreated and at 0.86 MGy EB irradiation dose (after 180 days aging) for GFRP a-sections.

Figures 4.18 and 4.19 shows results of a 4-point bend test of untreated and 0.86 MGy irradiated a-section (texture angle random zero to 90 deg) samples. The EB samples were aged 180 days. Samples selected were halves ($l = \sim 40$ mm) that had already been Charpy impacted where damage in the form of surface cracks from the impact was not observed in the length of the half specimen. Untreated and treated samples were taken from identical sections of a quadrant within the panels to obtain equal solidification flow patterns. Figure 4.18 shows the HLEBI probably increased the bending flexural stress and strain. Figure 4.19 shows applying the 0.86 MGy HLEBI followed by 180 days aging apparently increased the flexural strength $\sim 35\%$ at $P_f = 0.50$ from 56.7 to 76.6 MPa.

4.4 Results (Charpy impact of diagonal solidification texture angle: $\theta_t = 45+/-10$ degrees) c-sections
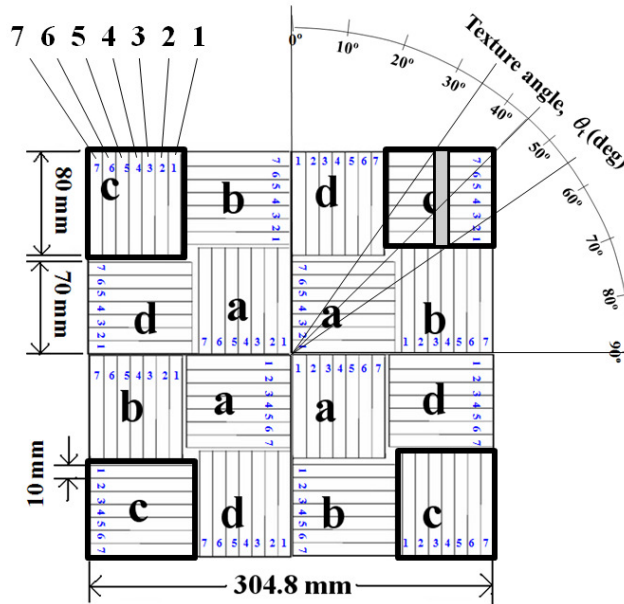

Fig. 4.20 Samples of "c-sections" at corners were tested that have diagonal dstribution of solidification texture angles (from longitudinal direction of sample) of 45 +/- ~10 degrees.
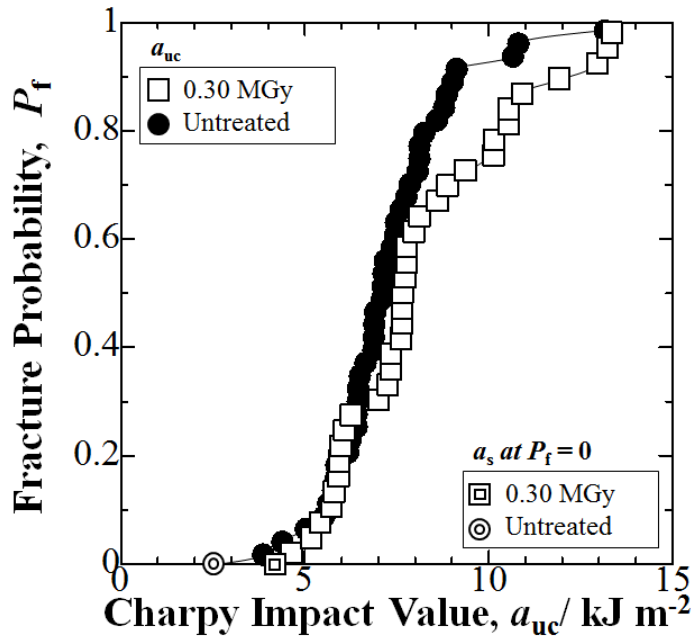

Fig. 4.21 Relationships between Charpy impact value, a_{uc} and fracture probability, P_f for c-sections 45 +/- 10 deg samples of GFRP panels before and after 0.30 MGy HLEBI. Lowest impact values a_{uc} at $P_f = 0$ (a_s) are included.

Although tests of HLEBI irradiation decreased impact values of compression-molded panel b-sections (solidification texture angle, θ_t = 68+/-7), and had little or no effect on the d-sections (θ_t = 17.5+/-17.5) (see diagram Figure 4.20), applying 0.30 MGy irradiation increased the impact values, a_{uc} of the c-sections.

Interestingly, the samples enhanced by the HLEBI, in sections 'a' and 'c' have average θ_t of 45 deg, section-a is 0 to 90 random. This may be due to average positions and flow patterns of fibers.

Figure 4.21 shows at P_f = 0.50 applying 0.30 MGy HLEBI increased Charpy impact value 12% over the untreated.
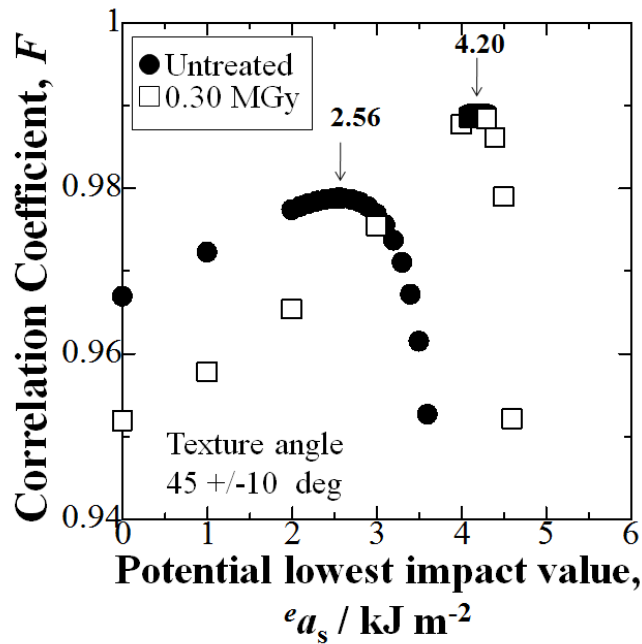

4.4.1 Weibull analysis: 3-parameter

Fig. 4.22 Changes in correlation coefficient (F) versus the potential a_s value ($^e a_s$) for P_f = 0 for c-sections 45 +/- 10 deg samples. The lowest impact value (a_s) was determined at maximum F.

Moreover, although the 2-dimensional Weibull coefficient, n for consistence was reduced by the HLEBI, Figure 4.22 shows the lowest impact value, a_s at P_f = 0 was increased 64% from 2.56 to 4.20 kJm^{-2}, demonstrating the statistically weakest possible sample is strengthened by applying the 0.30 MGy EB dose. This result can contribute to industry by increasing safety and reliability of aircraft, automobile and other parts.

4.5   Conclusions

1) By using homogeneous EB irradiation Charpy impact strength was apparently improved 5 to 25% in the typically weaker center region of compression-molded BMC GFRP panel "a-sections" with solidification texture angle with respect to the longitudinal direction of sample, θ_t = random: zero to 90 degrees. In addition, the HLEBI appeared to increase the flexural modulus at low strains in the θ_t = random: zero to 90 degree samples. Moreover, results indicate it is possible to increase flexural strength of the θ_t = random: zero to 90 degree samples by 4-point bend.

2) Fracture mechanism was observed to convert at a_{uc} > ~5.4 ~ 6.7 kJm^{-2} from clean to secondary microcrack proliferation and/or bends near the main crack, with increasing fracture surface area as a_{uc} increased.

3) SEM observation revealed 0.86 MGy HLEBI treated GFRP had much more polymer adhering to fibers than the untreated. ESR peaks indicated dangling bonds are generated creating repulsive forces between outer shell electrons in the polymer matrix, apparently exhibiting increased compressive stress on the fibers increasing adhesion force. Moreover, the lone pair electrons generated in the matrix may have bonded with the fibers more efficiently.

4) Charpy impact strength and lowest statistical impact value, a_s at P_f = 0 was apparently improved in the "c-sections" with solidification texture angle with respect to the longitudinal direction of sample, θ_t = 45+/-10 degrees. These results shows applying HLEBI to aircraft, automobile, sports and other short fiber GFRP-BMC components can have benefit in industry.

REFERENCES

[4.1] Faudree M., Nishi Y. and Gruskiewicz M., Mater. Trans. **53** (2012) 1412-2310.

[4.2] Weibull W., *Ingeniörs vetenskaps akademien*, nr. 151, (Generalstabens litografiska anstalts förlag, Stockholm, 1939) pp. 12-14.

[4.3] Weibull W., *Ingeniörs vetenskaps akademien*, nr. 153, (Generalstabens litografiska anstalts förlag, Stockholm, 1939) pp. 16-22.

[4.4] Iwata K., Kobayashi H. and Nishi Y., J. Jpn. Inst. Met. **69,** (2005) 1016-1020.

[4.5] Nishi Y., Kawazu H., Takei H., Iwata K., Kudoh H. and Mitsubayashi K., Mater. Trans. **52,** (2011) 1943-1948.

[4.6] Takei H., Iwata K., Salvia M., Vautrin A, and Nishi Y., Mater. Trans. **51,** (2010) 2259-2265 (2010).

Chapter 5

Compression molded BMCs: Improving Charpy impact value of short glass fiber (GFRP) samples of solidification texture angles of Random 0 to 90, 17.5+/-17.5, 45+/-10, and 68+/-7 degrees by extended mix shortening the fibers to sub-millimeter

ABSTRACT

5.1 Results

5.1.2 Effect of shortening fibers on impact strength of panel at all texture angles, θ_t cumulative

5.1.3 Effect of shortening fibers on impact strength as a function of texture angle

    5.1.3.1   a-section [θ_t = Random (45) 0 to 90 deg]

    5.1.3.2   b-section [θ_t = 68+/-7 deg]

    5.1.3.3   c-section [θ_t = 45+/-10 deg]

    5.1.3.4   d-section [θ_t = 17.5+/-17.5 deg]

5.2 Discussion

5.2.1 Comparing impact strength of texture angles in the shortened fiber panels

5.3 Conclusions

References

ABSTRACT

Shortening fibers by 30 min extended mix appears to be a good method to increase the impact values, a_{uc} in all sections (solidification texture angles, θ_t) of the orthotropic compression molded BMC-GFRP. For all θ_t cumulatively in the panel: random 0 to 90, 68, 45, and 17.5 deg of the 'a', 'b', 'c', and 'd' sections (see Chapter 2) shortening fibers by extended mix apparently improved Charpy impact value a_{uc} 29%, at mid-fracture probability $P_f = 0.50$. Moreover, at high $P_f = 0.88$, a_{uc} of the cumulative sections was improved 40% from 9.57 to 13.38 kJm^{-2}. For the specific panel sections the a_{uc} at mid-$P_f = 050$ was improved 25%, 18%, 35%, and 20% in the random 0 to 90, 68, 45, and 17.5 deg samples, respectively. Optical microscopy showed the extended mix formulation had much shorter fibers than the commercial. Within the short fiber panel, the experimental data follows the same trend as the commercial 6 mm samples in Chapter 3: the hierarchy of impact strength is $\theta_t = 68 \rightarrow 45 \rightarrow 17.5$ deg, with the random 0 to 90 deg samples having the lowest impact values.

5.1 Results
5.1.1 Effect of shortening fibers on impact strength of panel at all texture angles, θ_t cumulative
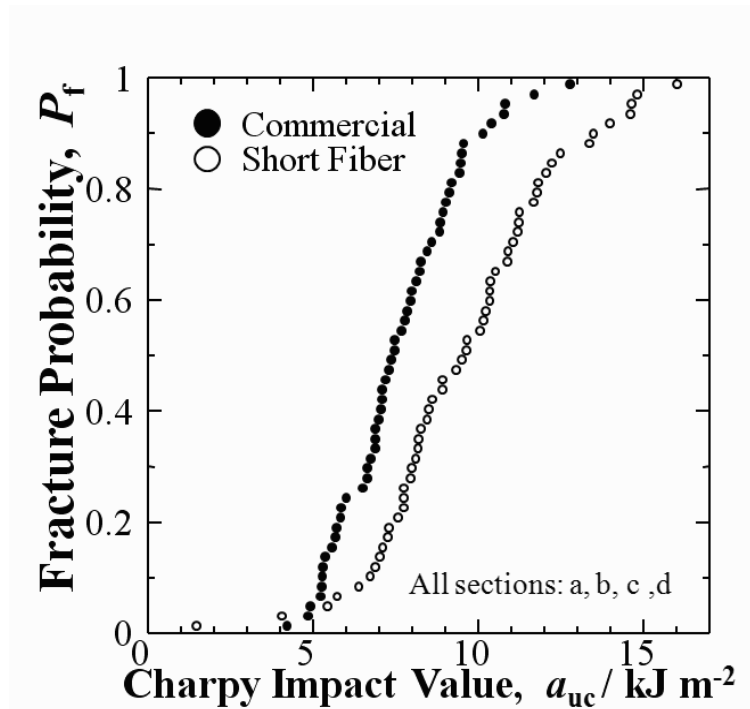

Fig. 5.1 Relationships between Charpy impact value、a_{uc} and fracture probability, P_f for commercial and shortened fiber (by extended mix) GFRP-BMC compression-molded panel: all sections cumulative: a,b,c,d.

To assess effect of shortening fibers of the GFRP-BMC mother panels, the BMC paste was mixed an additional 30 minutes by the Banbury mixer prior to compression

molding. Figure 5.1 shows the results for all solidification texture angles, θ_t cumulatively in the panel: [Random (45) 0 to 90 deg], [68+/-7 deg], [45+/-10 deg], and [17.5+/-17.5 deg] of the 'a', 'b', 'c', and 'd' sections (see Chapter 2). There were 14 specimens tested for each texture angle equaling 56 specimens each for the short and long fiber samples, respectively.

Fig. 5.1 shows shortening fibers by extended mix apparently improved Charpy impact value a_{uc} 29%, from 7.43 to 9.59 kJm^{-2} at mid-fracture probability $P_f = 0.50$. Moreover, at high $P_f = 0.88$, a_{uc} was improved 40% from 9.57 to 13.38 kJm^{-2}. The test procedures and statistical analyses are mentioned in Chapters 2, 3 and 4 and are referenced here [5.1-5.4].

However, the impact values were decreased at low P_f less than 0.05, in two specimens out of the total population of 56. Nevertheless, the other 54 samples were improved and average a_{uc} was raised 26% over the commercial.

5.1.3 Effect of shortening fibers on impact strength as a function of texture angle
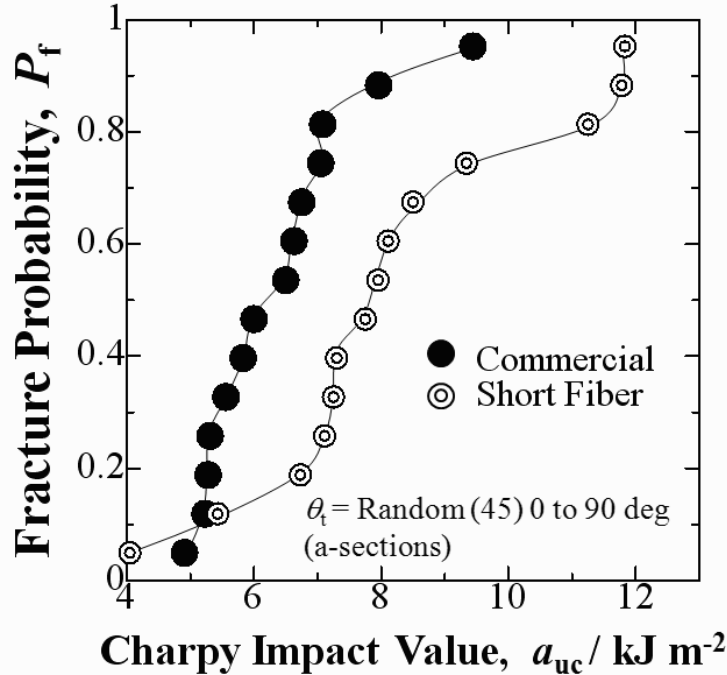### 5.1.3.1   a-section [θ_t=Random (45) 0 to 90 deg]

Fig. 5.2 P_f vs. a_{uc} for commercial and shortened fiber (by extended mix) GFRP-BMC panel a-sections (solidification texture angle, θ_t = Random: 0 to 90 deg).

Figures 5.2-5.5 show effect of shortening fibers on impact strength for each texture angle section 'a', 'b', 'c', 'd' of the mother panels separately. Fig. 5.2 shows for the typically weakest center of GFRP panel with texture angle: Random (45) 0 to 90 deg (a-sections), shortening fibers by extended mix improved the Charpy impact value a_{uc} 25%, from 6.26 to 7.86 kJm^{-2} at mid-fracture probability $P_f = 0.50$. Moreover, at high $P_f = 0.88$ a_{uc} was improved 48% from 7.97 to 11.79 kJm^{-2}. Furthermore, average a_{uc} was improved 28% over the commercial.
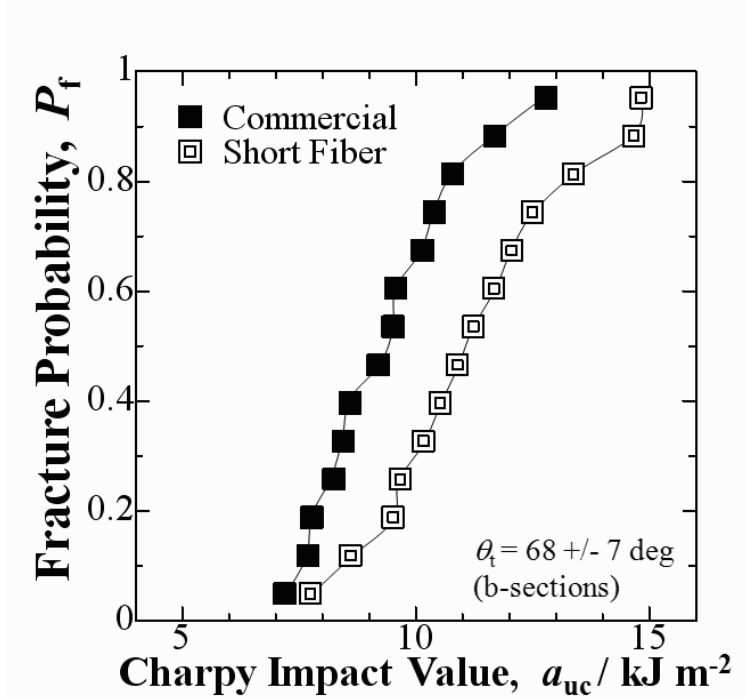
5.1.3.2 b-section [θ_t=68+/-7 deg]

Fig. 5.3 P_f vs. a_{uc} for commercial and shortened fiber GFRP- BMC panel b-sections (θ_t = 68+/-7 deg).

Fig. 5.3 shows for the highest texture angle of 68 deg (b-sections) of the GFRP panel, shortening fibers by extended mix evidently improved Charpy impact value a_{uc} 18%, from 9.36 to 11.07 kJm^{-2} at mid-fracture probability P_f = 0.50. Moreover, at high P_f = 0.88 a_{uc} was improved 25% from 11.70 to 14.67 kJm^{-2}. Furthermore, average a_{uc} was improved 19% over the commercial. The a_{uc} was improved at all fracture probabilities, P_f.

5.1.3.3   c-section [θ_t=45+/-10 deg]
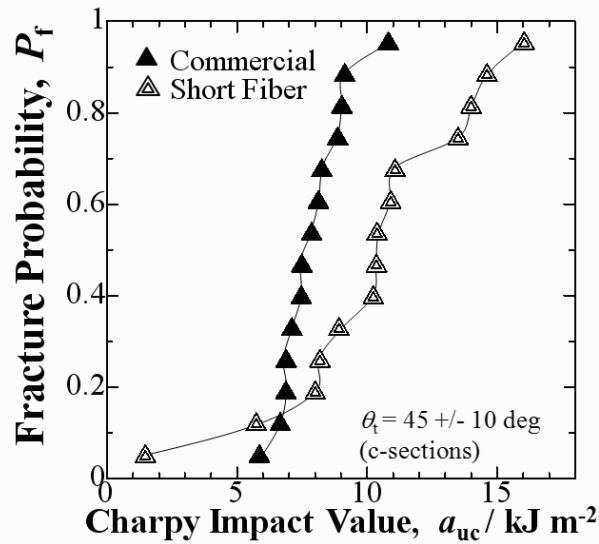
Fig. 5.4 P_f vs. a_{uc} for commercial and shortened fiber GFRP- BMC panel c-sections (θ_t = 45+/-10 deg).

Fig. 5.4 shows for the diagonal texture angle of 45 deg (c-sections) of the GFRP panel, shortening fibers by extended mix evidently improved Charpy impact value a_{uc} 35%, from 7.68 to 10.37 kJm^{-2} at mid-fracture probability P_f = 0.50. Moreover, at high P_f = 0.88 a_{uc} was improved remarkably 60% from 9.14 to 14.61 kJm^{-2}. Furthermore, average a_{uc} was improved 30% over the commercial.

5.1.3.4   d-section [θ_t=17.5+/-17.5 deg]
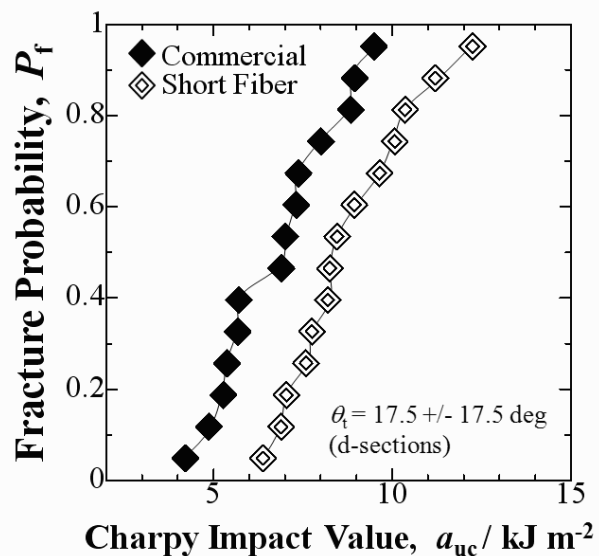
Fig. 5.5 P_f vs. a_{uc} for commercial and shortened fiber GFRP- BMC panel d-sections (θ_t = 17.5+/-17.5 deg).

81

Fig. 5.5 shows for the texture angle of 17.5 deg (d-sections) of the GFRP panel, shortening fibers by extended mix evidently improved Charpy impact value a_{uc} 20%, from 6.96 to 8.36 kJm^{-2} at mid-fracture probability $P_f = 0.50$. Moreover, at mid-$P_f = 0.40$ a_{uc} was improved 44% from 5.71 to 8.20 kJm^{-2}. Furthermore, average a_{uc} was improved 29% over the commercial. The a_{uc} was improved at all fracture probabilities, P_f.

Interestingly, the highest increase in impact value, a_{uc} was at high-$P_f = 0.88$ for a, b, and c sections (48, 25, 60%) as well as the cumulative texture angles at 40%. Moreover, in the commercial data sets the highest a_{uc} were much higher than the others. This could be explained by a radial fiber density gradient where fiber density increases with radial distance from the panel center point. SEM photos of the commercial formulation in Chapter 3 (Figs. 3.10 and 3.11) showed higher fiber density in the outside b-sections compared to the center a-sections.

As shown in the panel layout in Fig. 2.3 (Chapter 2) specimen number 7 of the 'b' and 'c' sections are at the panel edge and fibers could accumulate in that locale due to backflow. Moreover, specimen 7 of the a-sections would have the largest texture angle with respect to longitudinal direction of sample compared to samples 1-6 and may have higher fiber densities since it is farther from the center point. On the other hand, the d-section samples exhibit low texture angles with respect to longitudinal distance of specimen for all specimens 1 to 7.

Figure 5.6 shows optical microscope photos of commercial and shortened fiber formulations from center a-sections. Fibers appear much shorter in the extended mix (bottom) photo.
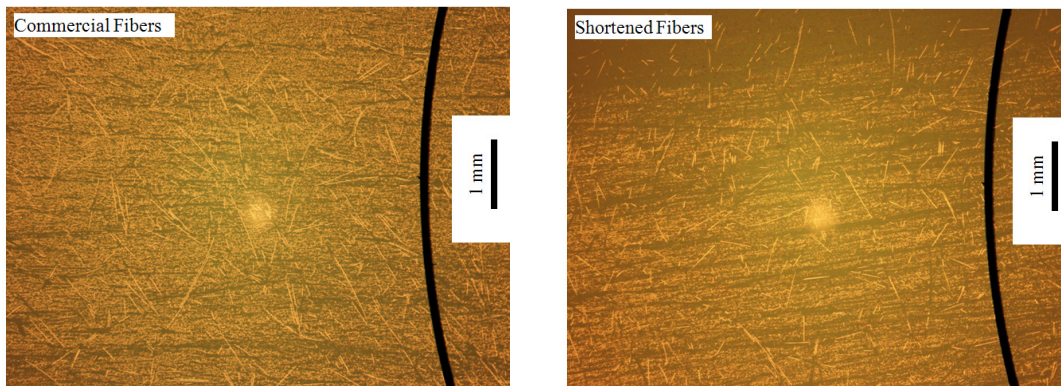

Fig. 5.6 Optical microscope photos of commercial and shortened fiber formulations from center a-sections.

5.2 Discussion
5.2.1 Comparing impact strength of texture angles in the shortened fiber panels
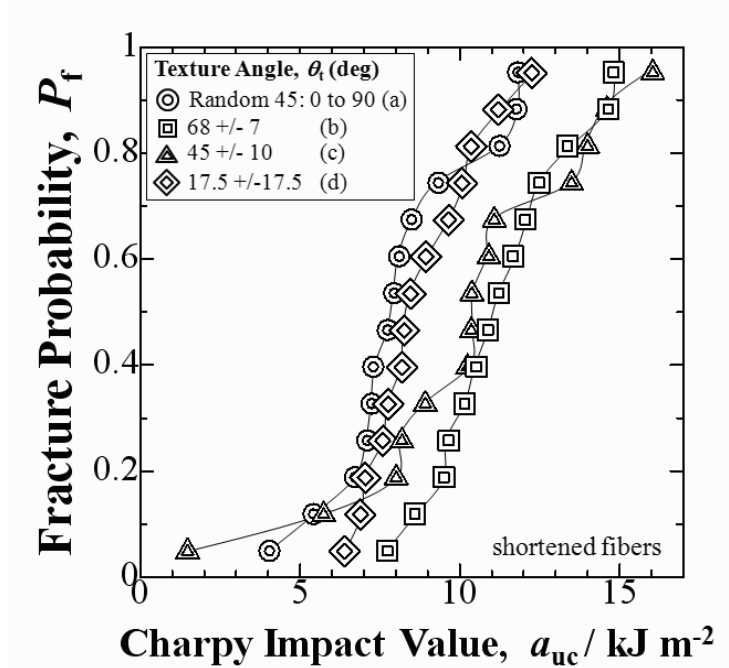

Fig. 5.7 P_f vs. a_{uc} for shortened fiber GFRP-BMC panels comparing a_{uc} for texture angles of a, b, c, and d-sections.

Figure 5.7 shows a comparison of impact strength for the different texture angles in the shortened fiber panels. From Fig. 5.6 it is apparent the data follows the same trend as the commercial 6 mm samples in Chapter 3: the hierarchy of impact strength is $\theta_t =$ 68 ➔ 45 ➔ 17.5 deg, with the random 0 to 90 deg samples having the lowest impact values. The a_{uc} values at $P_f = 0.50$ were 11.07, 10.37, 8.36, and 7.86 kJm^{-2} for the $\theta_t =$ 68, 45, 17.5 deg samples, followed by the random samples at the lowest value, respectively. Increasing the texture angle in the shorter fiber samples from 17.5 to 68 deg appeared to raise the a_{uc} remarkably at 32%. Moreover increasing a_{uc} in the shorter fiber samples from the random (45) to 68 deg raised the a_{uc} remarkably at 41%.
At $P_f = 0.88$, the a_{uc} were 14.67, 14.61, 11.10, and 11.79 kJm^{-2} for the 68, 45, 17.5 deg samples, followed by the random samples at the lowest value, respectively. In the 45 deg (c-section) and random 0 to 90 deg (a-section) data sets , one sample each displayed low impact values therefore carefulness is recommended when manufacturing parts in industry. However, shortening fibers from 6 mm commercial by 30 min extended mix appears to be a good method to increase the impact values, a_{uc} in all sections (solidification texture angles, θ_t) of the compression-molded BMC-GFRP. Shortening fibers to sub-millimeter has also been found to increase fracture strength and strain in injection molded SGFRP-BMCs [5.5, 5.6] which has not been reported in the literature prior to these studies and will be discussed in Chapters 6, 7 and 8.

5.3 Conclusions

1) Shortening fibers by extended mix apparently improved Charpy impact value a_{uc} 29%, at mid-fracture probability $P_f = 0.50$ of the compression molded GFRP-BMC panels.

2) For the specific panel sections the a_{uc} at mid-$P_f = 050$ was improved 25%, 18%, 35%, and 20% in the random 0 to 90, 68, 45, and 17.5 deg samples, respectively.

3) Shortening fibers by 30 min extended mix appears to be a good method to increase the impact values, a_{uc} in all sections (solidification texture angles, θ_t) of the orthotropic compression molded BMC-GFRP.

REFERENCES

[5.1] Faudree M., Nishi Y. and Gruskiewicz M., Mater. Trans. **53** (2012) 1412-2310.

[5.2] JIS K 7077 (1991).

[5.3] Nishi Y. and Salvia M., Mater. Trans., **47** (2006) 2846-2851.

[5.4] Nishida T. and Yasuda E., Evaluation of Dynamic Properties of Ceramics (Ceramics no rikigaku tokusei hyouka in Japanese), (Nikkan Kogaku Shimbun Sha, Tokyo, 1986) pp. 5051.

[5.5] Faudree M. and Nishi Y., Mater. Trans. **51** (2010) 2304-2310.

[5.6] Faudree M., Hiltner A., Baer E. and Collister J., J. Compos. Mater. **22** (1988) 1170-1195.

Chapter 6

A novel 'fiber spacing' model and tensile modulus enhancement in an injection-molded GFRP-BMC

[*Enhancement and 'fiber spacing' model of tensile modulus as a function of shortening fibers in a highly-filled GFRP-BMC composite*]

ABSTRACT

Up to now, increasing modulus of fiber reinforced polymers (FRPs) by shortening fibers has not been reported however, shortening fiber length from commercial 6.4 to 0.44 mm by additional mixing of paste prior to injection molding was found to increase initial and maximum tensile modulus 5 to 25% in a 3-phase fiber-filler-polymer system, highly-filled 20.0 mass% E-glass fiber reinforced thermoset polyester/styrene-butadiene polymer bulk-molding compound (GFRP-BMC). The increased number of spaces between fibers appears to allow for action of coefficient of thermal expansion (CTE) difference between fibers and matrix to increase thermal compressive residual stress sites during shrink and cool-down. A novel 'fiber spacing' model is constructed which predicts effect of fiber length (l_f), diameter (d), fiber volume fraction (V_f), filled-matrix (E_m) and fiber (E_f) materials on tensile modulus $(d\sigma/d\varepsilon)_o$ to be useful in BMC composite design. The model fits well with the experimental data and some data for 2-phase polymer systems in the literature, although behavior of the BMC is opposite: modulus is increased with decreasing l_f.

6.1 Results
6.1.1 Effect of fiber length on initial slope of stress – strain curves at $\varepsilon = 0$

Data points of stress (σ) as a function of strain, ε were obtained graphically using power point computer program by magnifying typical stress-strain curves of the BMC-GFRP from an earlier study [6.1] at the highest resolution possible: 0.00734% strain increments, i. The interpolations in Figure 6.1 show shortening fiber length increases initial tensile slope, $(d\sigma/d\varepsilon)_o$ 27% from 6.19 to 7.86 GPa as obtained by least squares best fit of the first 8 data points including 0; $\varepsilon = 0$ to 0.0514% extrapolated to 0 strain. The 3.2 mm and 0% glass samples had $(d\sigma/d\varepsilon)_o$ of 7.18 and 4.39 GPa, respectively. Although slopes were measured from the zero point, rather than tension and compression through the zero point the $(d\sigma/d\varepsilon)_o$ may be considered to strongly correspond to tensile elastic modulus. Linear correlation coefficient, R of 0.998, 0.999, 0.998, and 0.998 were obtained for 0.44, 3.2, 6.4 mm GFRP and 0% glass samples, respectively indicating highly linear stress-strain behavior at low strains.
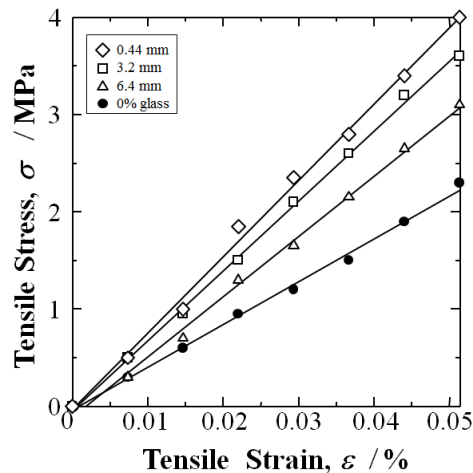

Fig. 6.1 Stress-strain curves from typical samples of ε from 0 to 0.0514% [6.1] of initial tensile modulus, $(d\sigma/d\varepsilon)_o$.

6.1.2 Effect of fiber length on tensile modulus (dσ/dε) against strain, ε

To obtain maximum moduli as a function of fiber length, Figure 6.2 shows tensile modulus (dσ/dε) as a function of ε, for the entire deformation process. Slopes (dσ/dε)$_{i+0.5}$ were taken between data points (σ_i, ε_i) and (σ_{i+1}, ε_{i+1}) in eq. (6.1):

$$(\mathrm{d}\sigma/\mathrm{d}\varepsilon)_{i+0.5} = (\sigma_{i+1} - \sigma_i)/(\varepsilon_{i+1} - \varepsilon_i) \qquad (6.1)$$

where integer, i at strain increments $\Delta\varepsilon = 0.00734\%$ goes from 0 to (n-1) (n is fracture point).
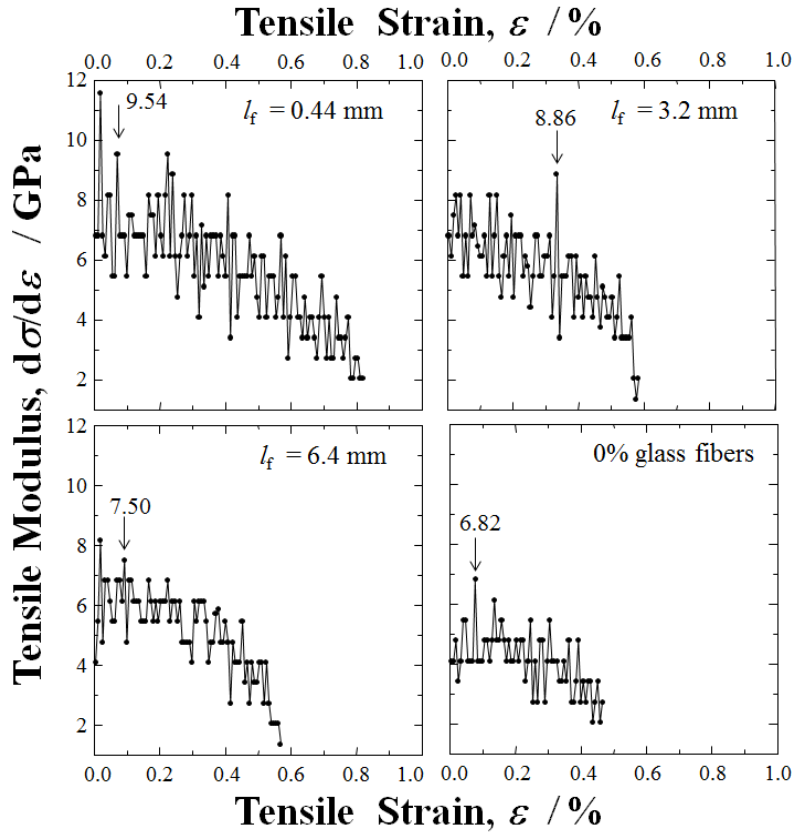
Fig. 6.2 Tensile modulus (dσ/dε), (GPa) vs. strain for fiber containing, and the matrix 0% glass composite. Both composites contain the CaCO$_3$ filler. (arrows indicate the (dσ/dε)$_{max}$).

At early strains before 0.25%, the BMC with l_f = 0.44 mm clearly exhibited higher (dσ/dε) values than that of the commercial 6.4 mm sample. Although the 0.44 mm sample had drops in modulus between 0.07% and 0.16% strain, there was a hardening returning to the maximum of 9.54 GPa at 0.22% strain. All in all, the 0.44 mm sample appears to have maintained the initial modulus values until higher strains superior to that of the 3.2 mm sample as well. The 0.44 mm sample exhibited (dσ/dε) maxima above 6 GPa up to ~0.60% strain, whereas the 3.2 mm sample exhibited (dσ/dε) maxima above 6 GPa up to ~0.45% strain. In addition, the 0.44 mm sample had more maxima over 8 GPa (11 maxima) than that of the 3.2 mm sample (6 maxima).

Fig. 6.2 shows the (dσ/dε)$_{max}$ appeared to exhibit a hierarchy increasing with

decreasing fiber length; with $(d\sigma/d\varepsilon)_{max}$ for the $l_f = 0.44$, 3.2 and 6.4 mm samples (Fig. 6.2, arrows) at 9.54, 8.86, and 7.50, GPa, respectively. It appears shortening the fibers from 6.4 to 0.44 mm increased the $(d\sigma/d\varepsilon)_{max}$ 27%. Moreover, there appears to be a hierarchy of $(d\sigma/d\varepsilon)_{max}$ data points above 8 GPa for the 0.44, 3.2 and 6.4 mm samples at 11, 6 and 1, respectively. Since the first maximum of the 0.44 mm sample occurred very early in the deformation process and then decreased, the $(d\sigma/d\varepsilon)_{max}$ was evaluated at the second maximum for preciseness. The lowest $(d\sigma/d\varepsilon)_{max}$ was found in the 0% glass matrix composite at 6.82 GPa.

In summary, shortening fibers from 6.4 to 0.44 mm raises $(d\sigma/d\varepsilon)_{max}$ 27% from 7.50 to 9.54 GPa. The 0.44 mm samples also have 18 and 40% improvements in $(d\sigma/d\varepsilon)_{max}$ over the 3.2 mm (8.86 GPa) and 0% glass samples (6.82 GPa). With the variation is data it is assumed $(d\sigma/d\varepsilon)_o$ and $(d\sigma/d\varepsilon)_{max}$ can be increased 5 to 25% by shortening fibers from commercial 6.4 mm to 0.44 mm.

6.1.3 Linear relation between tensile moduli $(d\sigma/d\varepsilon)_o$, and $(d\sigma/d\varepsilon)_{max}$ and fiber length, l_f
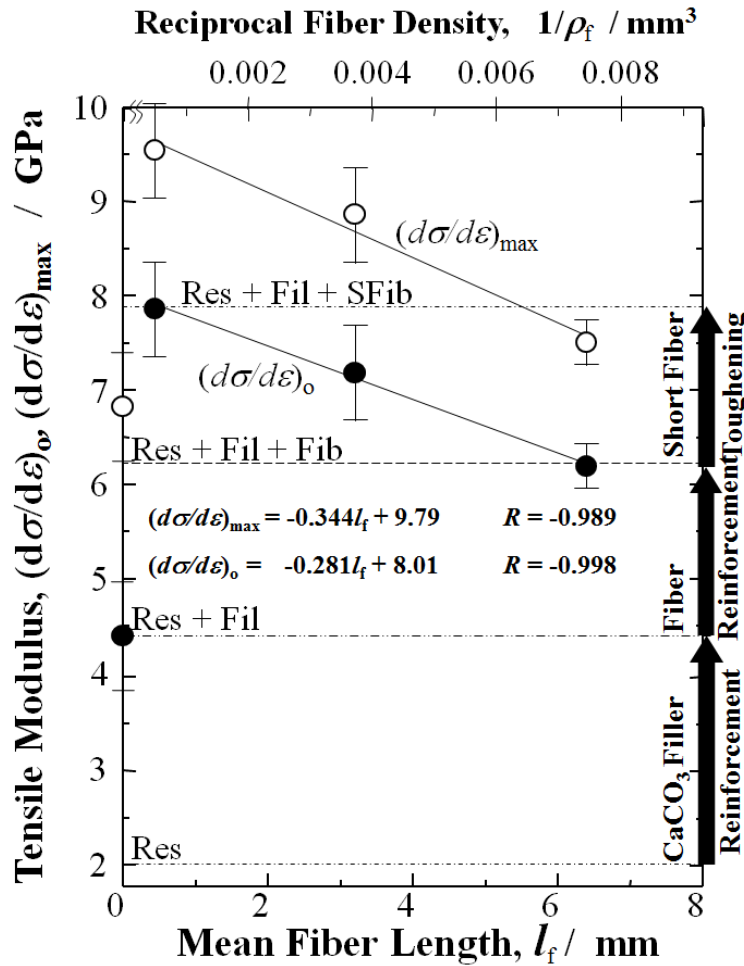
Fig. 6.3 Maximum $(d\sigma/d\varepsilon)_{max}$ and initial $(d\sigma/d\varepsilon)_o$ tensile moduli as a function of mean fiber length, l_f (mm) and reciprocal fiber density, $1/\rho_f$ (mm^3). Improvements are shown in $(d\sigma/d\varepsilon)_o$ by adding filler, fibers and shortening fibers. Bars are standard deviations.

Figure 6.3 summarizes the $(d\sigma/d\varepsilon)_o$, and $(d\sigma/d\varepsilon)_{max}$ with lines indicating $(d\sigma/d\varepsilon)_o$ strengthening by filler (Fil), fiber reinforcement (Fib) and the toughening by shortening fibers (SFib), respectively over polyester resin with tensile modulus = ~2 GPa. The $(d\sigma/d\varepsilon)_{max}$ is always higher than the $(d\sigma/d\varepsilon)_o$.

Interestingly, Fig. 6.3 shows a linear relation between tensile moduli $(d\sigma/d\varepsilon)_o$, and $(d\sigma/d\varepsilon)_{max}$ and l_f where r is fiber radius, $(7 \times 10^{-3}$ mm):

$$(d\sigma/d\varepsilon)_{max} = -0.344\ l_f + 9.79 \qquad R = -0.989 \qquad (6.2)$$

$$(d\sigma/d\varepsilon)_o = -0.281\ l_f + 8.01 \qquad R = -0.998 \qquad (6.3)$$

And fiber density is related to fiber length by eq. (6.4) [6.1]:

$$\rho_f = V_f/(\pi r^2\ l_f) \qquad (6.4)$$

This indicates modulus improves linearly with reciprocal fiber density, $1/\rho_f$ (mm^3) (Fig. 6.3) by the equations:

$$(d\sigma/d\varepsilon)_{max} = -295(1/\rho_f) + 9.79 \qquad R = -0.989 \qquad (6.5)$$

$$(d\sigma/d\varepsilon)_o = -240(1/\rho_f) + 8.01 \qquad R = -0.998 \qquad (6.6)$$

6.1.4 Scanning electron microscopy (SEM) and electron backscattering (EDX) of 0.44 mm samples
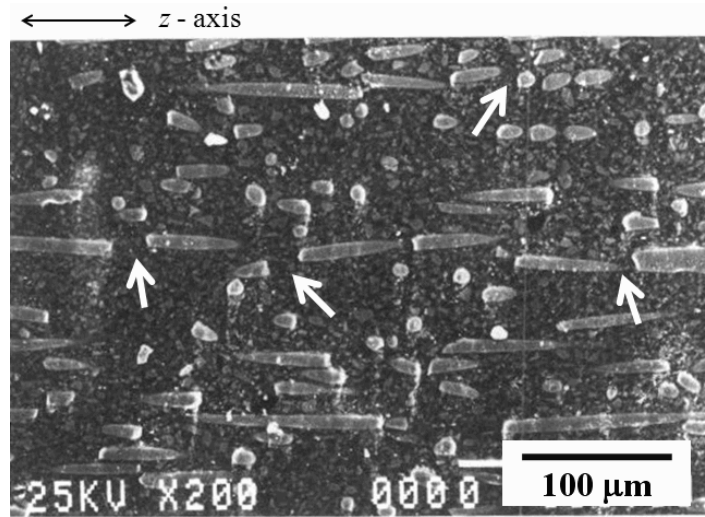
Fig. 6.4 Scanning electron micrograph of a 0.44 mm sample at zero strain with fibers oriented with the injection molding/tensile testing z-axis direction (black arrow) indicating spaces between fibers (white arrows).
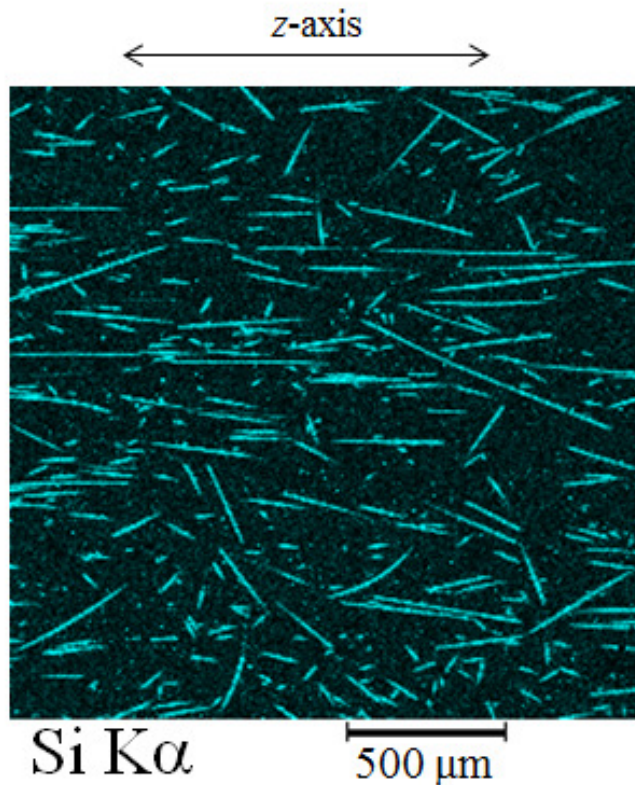
Fig. 6.5 EDX Si-Kα electron backscattering emissions scan of GFRP polished surface near the mold walls showing the mean 0.44 mm glass fibers oriented with the injection molding/tensile testing *z*-axis direction (arrow).

Figure 6.4 shows a photograph of a polished and Pt-sputtered 0.44 mm fiber length GFRP-BMC sample showing the dispersed fibers and considerable amount of spaces where fibers come in close proximity (white arrows) compared with SEM photographs of 6.4 mm samples in a previous study [6.1]. There are numerous spaces between fibers 10 to 50 μm in distance along the z-axis. The black arrow (top) is injection molding/tensile *z*-axis direction. Although fibers are generally aligned parallel to the injection mold flow *z*-axis (black arrow), some fibers appear to be at different angles within planes parallel to the molding/tensile direction. Fig. 6.4 shows the fibers are unbroken along the longitudinal direction, i.e., damage of the fibers by the additional mixing in the Banbury mixer results only in shortening the fibers along their lengths. The dispersion and size of the 1 to 7 μm $CaCO_3$ filler particles in the matrix appear unaffected by the additional mixing.

To obtain a view of the 0.44 mm sample at low magnification, an energy dispersive X-ray spectroscopy (EDX) Si-Kα scan was taken of a polished surface at the mold wall in Figure 6.5. Most fibers are in close proximity oriented at angles 0 to ~30 degrees from the molding/tensile direction (arrow), although a small portion are oriented >60 degrees in the lower portion.

6.2 Discussion
6.2.1 Fiber spacing
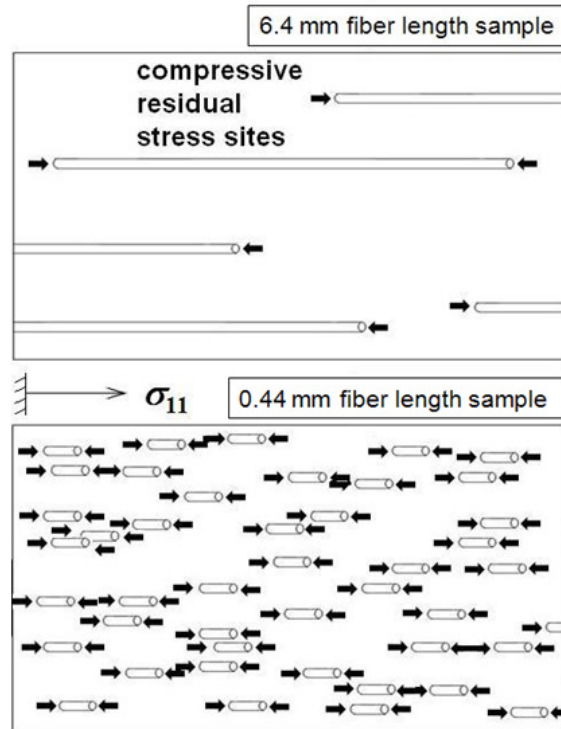
Fig. 6.6 Depiction of fibers aligned with molding/tensile testing direction. Fibers are scaled to relative lengths.

Figure 6.6 depicts fiber spacing for the ideal condition of fibers aligned with the molding/tensile direction. The arrows represent thermal compressive stresses of the matrix on the fibers from CTE difference in the molding/tensile direction. The proportionality is scaled to depict the 14.5 times increase in fiber density or number of spaces, S_f between fibers as l_f is shortened, $l_f = (1/S_f)$ from 6.4 to 0.44 mm. These compressive thermal residual stresses are contributors to the modulus increase in the 0.44 mm samples.

6.2.2 Fiber orientation
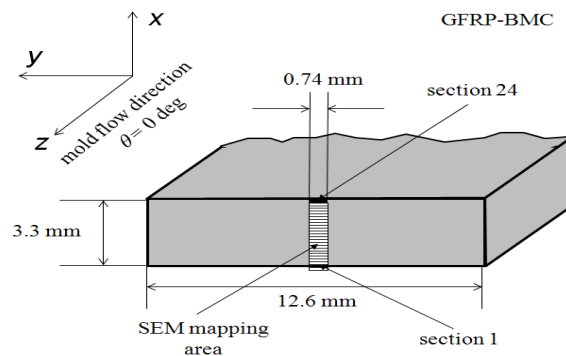
Fig. 6.7 Position of SEM mosaic taken across specimen thickness.
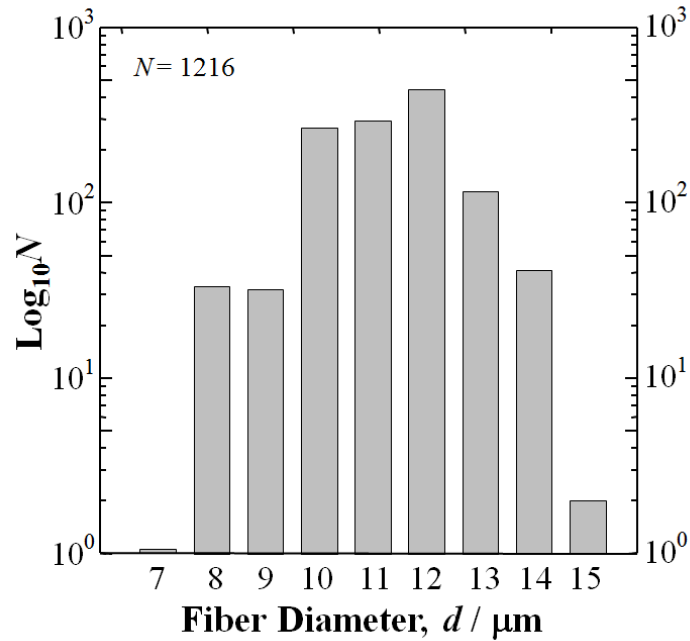
Fig. 6.8 Measured fiber diameter distribution.

Figure 6.7 shows the position of a mosaic of SEM photos taken across the 3.3 mm thickness of a 0.44 mm fiber length BMC sample normal to the tensile testing direction [6.2]. This was separated into 24 sections, each 0.01375 mm in thickness. Elliptical cross-sections were meticulously positioned over 1200 fibers using power point computer program and axes a and b were measured to obtain θ. Although nominal fiber diameter was 14 μm, the measurements showed average d=11.4 μm with standard deviation = +/-1.15 μm, thus 95% of the population was $9.1 < d < 13.7$ μm (Figure 6.8). The remaining ~2.6 μm was probably due to ~1.3 μm thick coupling agent coating around the pristine fibers prior to molding. The accuracy was +/-5.7% and +/-2.8% for ellipse short and long axes (a and b), respectively. The nominal fiber diameter of 14 μm will be used for calculations.
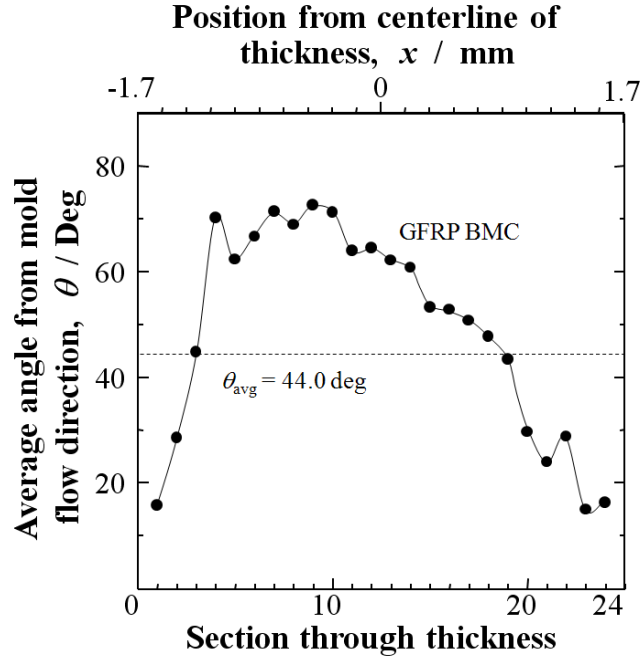
Fig. 6.9 Measured fiber orientation angle normal to the molding/tensile testing direction across the 3.3 mm thickness.

Fiber orientations, θ are calculated from eq. (2) and averaged for each section, j 1 through 24 in eq. (6.9):

$$\Sigma\theta_{o,j} = \Sigma_{ij}[N(\theta_{ij})(\theta_{ij})]/\Sigma_{ij}[N(\theta_{ij})] \qquad (6.7)$$

Hermans fiber orientation parameter, η_o which is the averaged over an area is then calculated from $\theta = \arccos(a/b)$ [6.2,6.3]. Thickness is separated into the 24 sections (Fig. 6.7) where average η_o for each section, j is [6.3]:

$$\eta_{o,j} = \Sigma_{ij}[N(\theta_{ij})\cos^2(\theta_{ij})]/\Sigma_{ij}[N(\theta_{ij})] \qquad (6.8)$$

$N(\theta_{ij})$ is number of fibers in each section, and i is fiber number within the section. The plot in Figure 6.9 shows the profile, a 3-layer [skin-core-skin] structure where in the "skins" fibers are highly aligned ($\theta = 0$ to ~20 deg; $\eta_o = 0.80\text{-}0.90$) with mold flow within a thin layer $\delta_f = 0.14$ to 0.27 mm (4-8% of thickness) from the mold walls. These "skins" surround a highly disoriented core whose fibers are ~30 to 90 deg from molding/tensile direction. Optical microscope observation showed the highly-oriented skins were found around most of the specimen cross-section perimeter. The SEM photomicrograph in Figure 6.10 shows fibers near the mold walls highly aligned with the molding/tensile direction as ellipses with low b/a ratios typical of sections 1, 23 and 24 in Fig. 6.9. On the other hand, Figure 6.11 shows fibers near the thickness center more perpendicular to the molding/tensile direction with high b/a ratios typical of sections 4 to 17. This flow pattern would resemble a 3-D elliptical paraboloid which is typical of the laminar creep flow of the highly viscous BMC paste during injection molding [6.2].
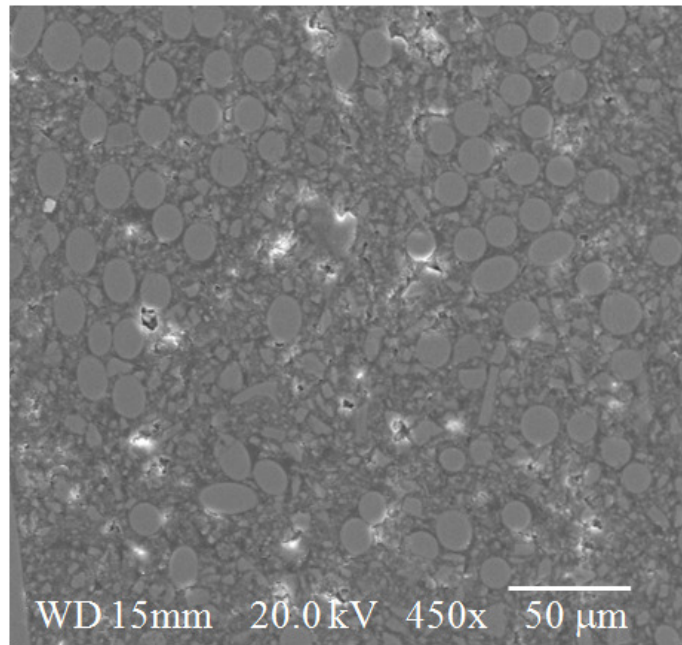
Fig. 6.10 SEM micrograph showing highly oriented fiber cross-sections near the mold wall. Molding/tensile z-direction is normal to the plane of the page.
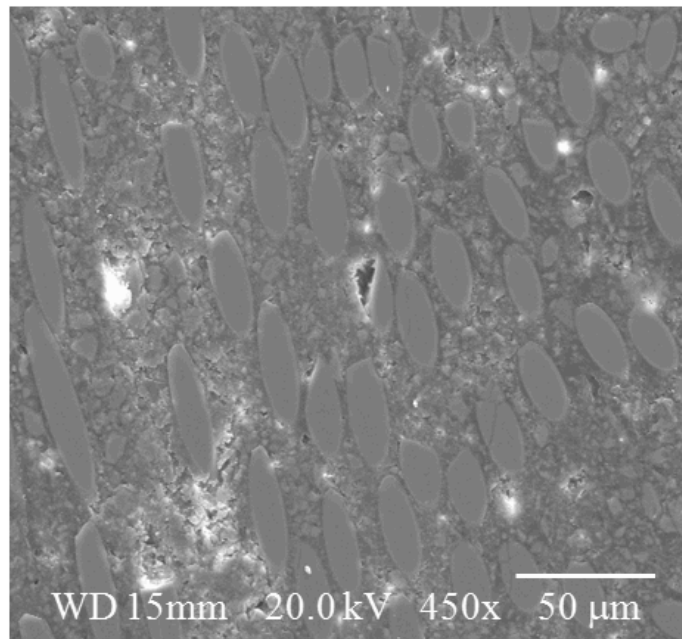

Fig. 6.11 SEM micrograph showing fibers oriented more perpendicular to the molding/tensile direction near the center of the thickness.

Figure 6.12 shows η_o across BMC specimen thickness (the inverse of θ) showing the 3-layer structure of the BMC. The dotted line shows the average fiber orientation parameter η_o calculated by eq. (6.8) is 0.481. Thomason's data of polyamide 6,6 is compared in Fig. 6.12 exhibiting 5-layer structure of [skin-shell-core-shell-skin]

95

averaged here by (32-51 mass% fibers, fiber lengths 0.48-0.72 mm) [6.3]. Although the polyamide 6,6 and the BMC have thin skins ~4% of thickness, the BMC skin is highly oriented while the polyamide 6,6 skins are highly disoriented. Since the 3-phase BMC including filler is higher viscosity, its fiber angle profile in more parabolic than the 2-phase glass fiber reinforced polyamide 6,6.
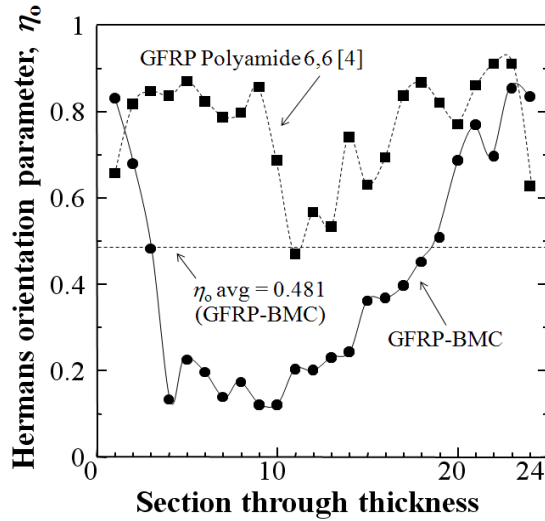
Fig. 6.12 Hermans fiber orientation parameter across BMC specimen thickness showing 3-layer structure of BMC compared to Thomason data of polyamide 6,6 exhibiting 5-layer structure averaged here by (32-51 mass% fibers, fiber lengths 0.48-0.72 mm) [6.1, 6.3].
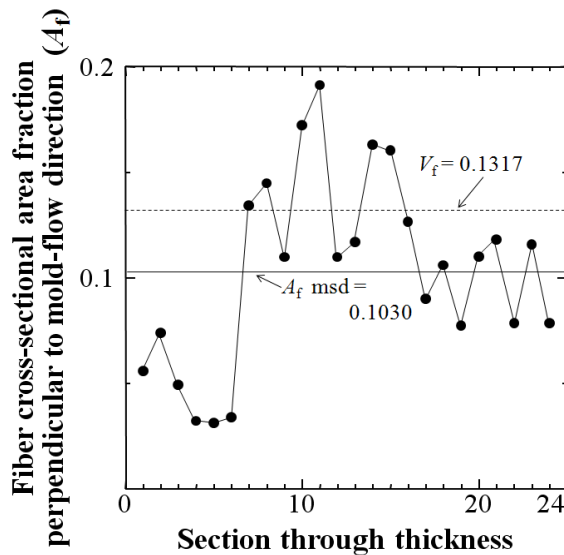
Fig. 6.13 Measured fiber cross-sectional area fraction, A_f perpendicular to molding/tensile direction across 0.44 mm fiber length 3.3 mm specimen thickness showing average (solid line); with volume fraction, V_f for comparison (dotted line).

Figure 6.13 shows measured fiber cross-sectional area fraction perpendicular to molding/tensile direction for each section, j of the BMC sample:

$$A_{f,j} = \Sigma_{ij}[N(A_{ij})(\pi a_{ij}b_{ij}/4)]/A_{c,j} \qquad (6.9)$$

Here, $N(A_{ij})$ is number of fibers in each section, $(\pi a_{ij}b_{ij}/4)$ is elliptical cross-sectional area, $A_{c,j}$ is total area of each composite section (all equal), and i is fiber number. Fig. 6.13 shows measured A_f ranges from 0.0311 in section 5, to 0.1911 in section 11. Average A_f (0.1030) of the cross-section is lower than V_f (0.1317) indicating again fibers are mostly aligned with molding/tensile direction. At higher injection speeds, melt and molding temperatures polymer composites exhibit a thicker core with a more square flow front meaning higher fiber planar density.

6.2.3 'Fiber spacing' model
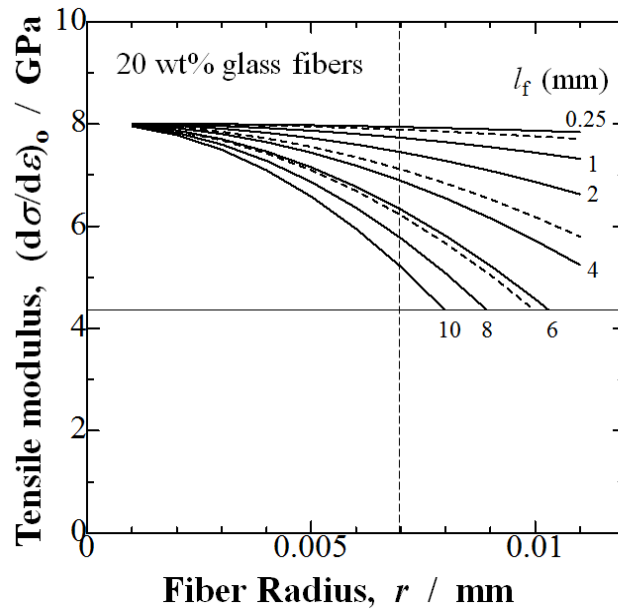
Fig. 6.14 'Fiber spacing' model for effect of fiber radius (mm) on tensile modulus (GPa) at different fiber lengths for 20 wt% fiber ($V_f = 0.1317$) BMC.

Since the difference in CTE between the matrix and the fibers generates compressive thermal residual stress sites between fibers in the molding/tensile direction raising he modulus, a 'fiber spacing' model is constructed. To build the model, the fiber density, ρ_f is set equal to the number of spaces between fibers, $(\rho_f = S_f)$ and eq. (6.5) becomes:
:

$$(d\sigma/d\varepsilon)_o = -240(1/S_f) +8.01 \qquad R = -0.998 \qquad (6.10)$$

And since $(1/S_f) = (\pi r^2 l_f/V_f)$, eq. (6.10) becomes:

$$(d\sigma/d\varepsilon)_o = -240(\pi r^2 l_f/V_f) + 8.01 \qquad (6.11)$$

Figure 6.14 shows the 'fiber spacing' model for effect of fiber radius, r on tensile modulus, $(d\sigma/d\varepsilon)_o$ at different fiber lengths for the 20 wt% fiber BMC (V_f = 0.1317). The vertical dotted line represents the fiber radius (0.007mm) of the experimental data. The solid horizontal line represents the experimental modulus of the 0% glass samples. The dotted curves represent the experimental fiber lengths tested: l_f = 0.44, 3.2 and 6.4 mm. At large r > 0.08 mm, shorter fiber lengths, l_f <~2 mm (low aspect ratio) are predicted to have higher moduli than longer fiber lengths above 8 mm. At high fiber radius decreasing the fiber length increases the modulus to a high degree. However, the upper limit of the modulus appears to be about 8 GPa and the shorter fibers below l_f = 2 mm are recommended regardless of radius. This is probably due to shorter fibers having higher fiber dispersion creating compressive stress sites.
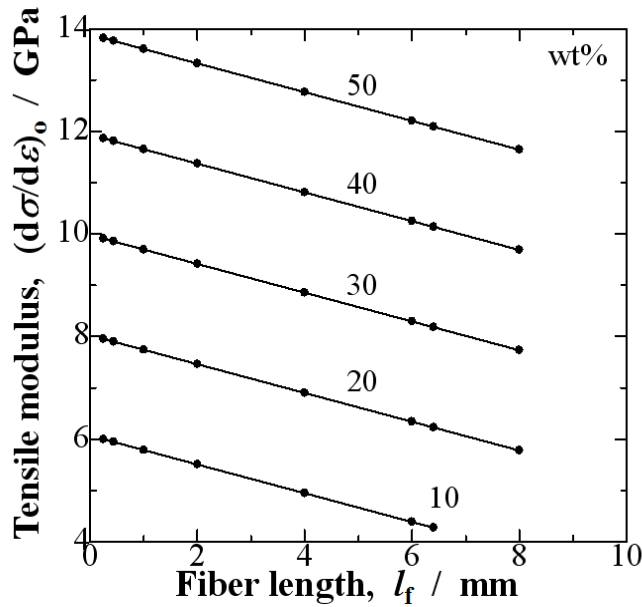
Fig. 6.15 'Fiber spacing' model for effect of fiber length (mm) on tensile modulus (GPa) for different fiber wt%. The linear regressions (solid lines) are those that do not dip below the matrix modulus of E_f = 4.39 GPa.

Figure 6.15 shows the 'fiber spacing' model for modulus $(d\sigma/d\varepsilon)_o$ vs. fiber length for different fiber weight percents (wt%). Since the increase in residual stress sites by CTE difference of the increased spaces between fibers is linear independent of volume fraction, the slope in eq. (13) is set equal to that of the experimental data -240($\pi r^2 l_f$ /0.1317) using V_f of 0.1317 (20 wt%). The y-intercept of the experimental data was 8.01 GPa and represents the maximum modulus possible therefore it is set using the 'rule of mixtures' [$\eta_o V_f E_f$ + (1- $V_f)E_m$] where E_f for E-glass fibers and E_m of the matrix measured for the 0% glass samples are 75 and 4.39 GPa, respectively. However the average orientation angle found (θ) is 44 degrees, therefore the corresponding Hermans fiber orientation parameter, η_o of 0.481 is factored in. A factor, f for modulus loss in the fibers by the mixing and injection molding process is also incorporated into the y-intercept. This is the ratio of the experimental maximum modulus over that calculated by the 'rule of mixtures' or [8.01/8.55].

98

Hence, the equation obtained is:

$$(d\sigma/d\varepsilon)_o = -240(\pi r^2 l_f/0.1317) + f\,[\eta_o V_f E_f + (1- V_f)E_m] \qquad (6.12)$$

yielding the plot in Fig. 6.15.

Interestingly, the 'fiber spacing' model agrees closely with data for the 2-phase glass fiber polyamide 6,6 for fiber lengths of 0.3 to 1.1 mm, diameters of 10-17 mm and wt% of 20-40%. For example $d = 10$ μm and $l_f \sim 1.0$ mm exhibited a tensile modulus of 8 GPa [6.3]; although behavior of the BMC is opposite: that modulus increases with decreasing fiber length.

In summary, the 'fiber spacing' model can possibly be used to design different types of highly-filled FRP composites. It may be possible to select fiber and matrix materials, fiber radius, length, and volume fraction of fibers.

6.3 Conclusions

1) By additional mixing of paste prior to injection molding shortening fibers from 6.4 mm commercial to 0.44 mm, initial $(d\sigma/d\varepsilon)_o$ and maximum $(d\sigma/d\varepsilon)_{max}$ tensile moduli were raised 5 to 25%. Up to now, this result has not been reported in the literature: most data for unfilled FRP reports increasing fiber length increases tensile modulus.

2) A novel 'fiber spacing' model is constructed which predicts effect of fiber length (l_f), diameter (d), fiber volume fraction (V_f), filled-matrix (E_m) and fiber (E_f) materials on tensile modulus $(d\sigma/d\varepsilon)_o$ to be useful in BMC composite design. The model is based on increased number of spaces, S_f between fibers as fiber length is shortened appearing to allow for action of an order of magnitude difference in coefficient of thermal expansion (CTE) difference between fibers and matrix increasing thermal compressive residual stress sites by the matrix on the fibers during shrink and cool-down.

3) The 'fiber spacing' model was found to fit well with the experimental data of the BMC and some data for 2-phase polymer systems in the literature of polyamide 6,6 for fiber diameters of 10 to 17 mm and fiber wt% of 20-40%, although behavior in the BMC is opposite: that modulus increases with decreasing fiber length..

4) In summary, the 'fiber spacing' model can possibly be used to design different types of highly-filled FRP composites.
.

REFERENCES

[6.1] Faudree M., Hiltner A., Baer E. and Collister J., J. Compos. Mater. 22 (1988) 1170-1195.

[6.2] Faudree M., Nishi Y. and Gruskiewicz M., Mater. Trans. **54** (2013) 1877-1883.

[6.3] Thomason J., Composites **A 39** (2008) 1732-1738.

Chapter 7

A novel 'fiber end crazing' model and tensile strength and strain enhancement in an injection-molded GFRP-BMC

[*Tensile Strength Enhancement by Shortening Glass Fibers with Sub-millimeter Length in Bulk Molding Polymer Compound*]

ABSTRACT

This chapter focuses on the novel and most important finding of this dissertation not previously reported in the literature that shortening fibers (rather than lengthening) in FRP from commercial 6.4 mm to submillimeter 0.44 mm significantly increased tensile strength, σ_f (~60%) and its strain, ε_f (~40%) of the highly-filled injection-molded GFRP-BMC. The mechanism is by the increased fiber end density, fiber end crazing sites are generated during deformation creating compressive stress sites halting cracks below the critical length reported for the polyester resin, $0.50 < 2a_c < 5.0$. This allows more microcracks to be tolerated increasing fracture strain. Moreover, the increased microcracking in the vicinity of the main crack tip acts to reduce the main crack tip stress concentration. Acoustic emission (AE) analysis detected microcracking was increased threefold. Log10 of total Energy per AE event, *E/N* appear to be the same independent of fiber length signifying many shorter cracks may occur at the same time compared to one large crack of the same surface area in the 6.4 mm samples. A 'fiber end crazing' model was constructed to describe the phenomena.

7.1 Results
7.1.1 Influence of fiber length on tensile stress-strain curves
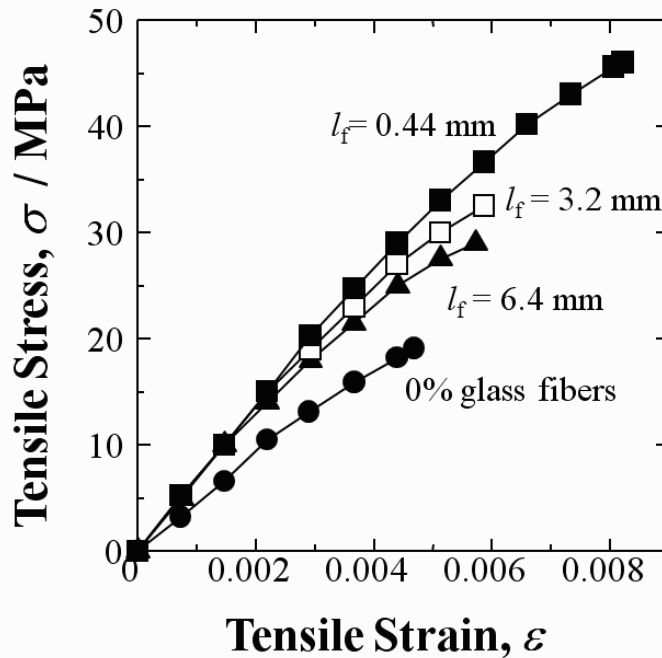
Fig. 7.1 Effect of fiber length, l_f (mm) on typical stress-strain curves with the 0% glass matrix composite of the BMC. Fiber reinforced samples contain 20 mass% E-glass fibers.

Figure 7.1 shows the stress-strain curves of GFRP for the different fiber lengths. The comparative plot is shown for typical runs representative of the four types of samples [7.1].

The trend follows that of several specimens tested and shows a significant

improvement in tensile properties where the masticated samples containing the shorter 0.44 mm length fibers had the highest fracture strain, stress and toughness followed by the 3.2 mm, 6.4 mm and 0% glass samples, respectively. With the 0.44 mm samples having a 5 to 25% rise in initial hardening moduli over the 6.4 mm, this represents a hierarchy of strength as mean fiber length is shortened: 0.44 mm > 3.2 mm > 6.4 mm, with the 0% glass samples having the lowest values.

7.1.2 Scanning electron microscopy of 0.44 mm fiber length samples
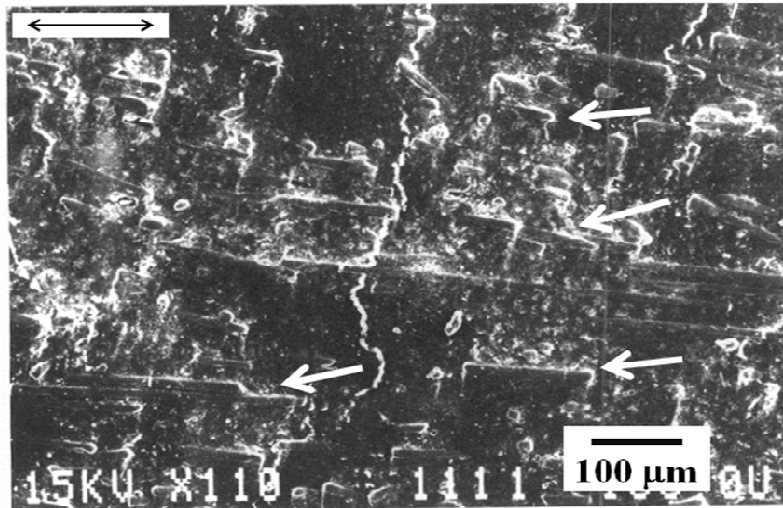
Fig. 7.2 Scanning electron micrograph of a polished surface of a shortened fiber 0.44 mm sample at low strain showing a considerable about of fiber end crazing in the form of whitening and incoherent interface along the fiber lengths (white arrows). Voiding and a small amount of microcracking are also observable in the matrix. The sample is undergoing flexural deformation (black arrow).

Figure 7.2 shows a scanning electron photomicrograph of polished and Pt-sputtered 0.44 mm fiber length BMC samples undergoing flexural deformation in the three-point bending apparatus at low strains in the SEM [7.2]. Fig. 7.2 shows a considerable amount of fiber end crazing in the form of whitening and incoherent interface propagating along the fiber lengths. Damage along the fibers is accompanied by voiding and a small amount of microcracking in the matrix. The microcrack in the bottom half of the photo is about 0.13 mm long. These matrix microcracks appear to originate independent of the fibers and are generally Mode I, perpendicular to the loading direction.
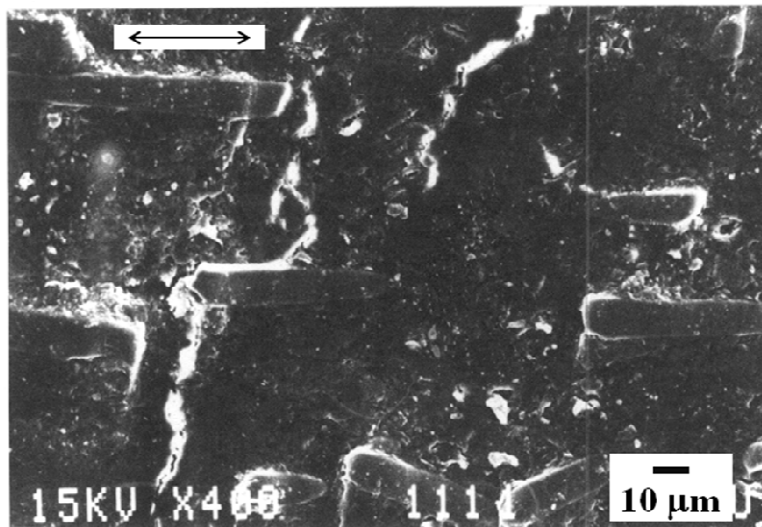
Fig. 7.3 Enlarged view from Fig. 7.2 showing fiber end crazing and crazing along the fiber lengths accompanied by short matrix cracks.

Figure 7.3 shows an enlarged view from Fig. 7.2 at higher magnification showing the crazing at the fiber ends and along their lengths more clearly. The small matrix microcracks and matrix voiding are also present.

Figure 7.4 illustrates damage occurring in the 0.44 mm fiber length BMC samples at high strains close to fracture showing larger crack formation occurring as matrix-filler separation and fiber pullout. Fiber ends can be seen projecting out of the matrix, indicating fiber pullout during large crack formation. SEM analysis did not find fiber fracture at high strains. The sample is undergoing flexural deformation in the three-point bending apparatus and was taken at a higher magnification.
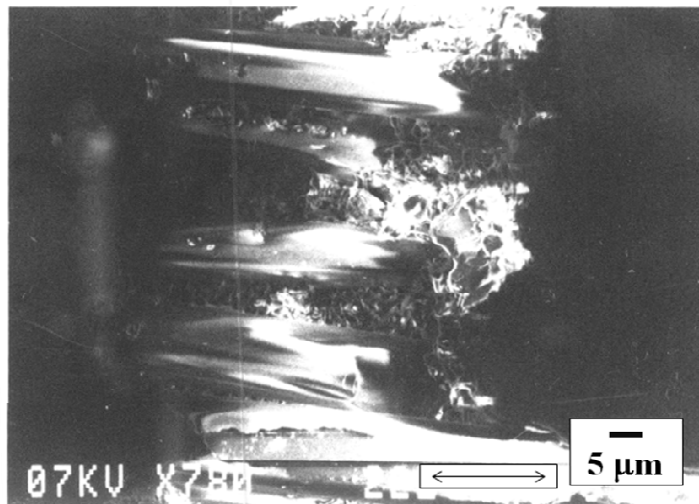
Fig. 7.4 Scanning electron micrograph of a 0.44 mm sample at high strain showing a large-scale crack with fiber pullout and matrix-filler separation. The sample was undergoing flexural deformation and was taken at a higher magnification.

7.2 Discussion

7.2.1 Influence of fiber length on tensile fracture strain, ε_f of BMC-GFRP
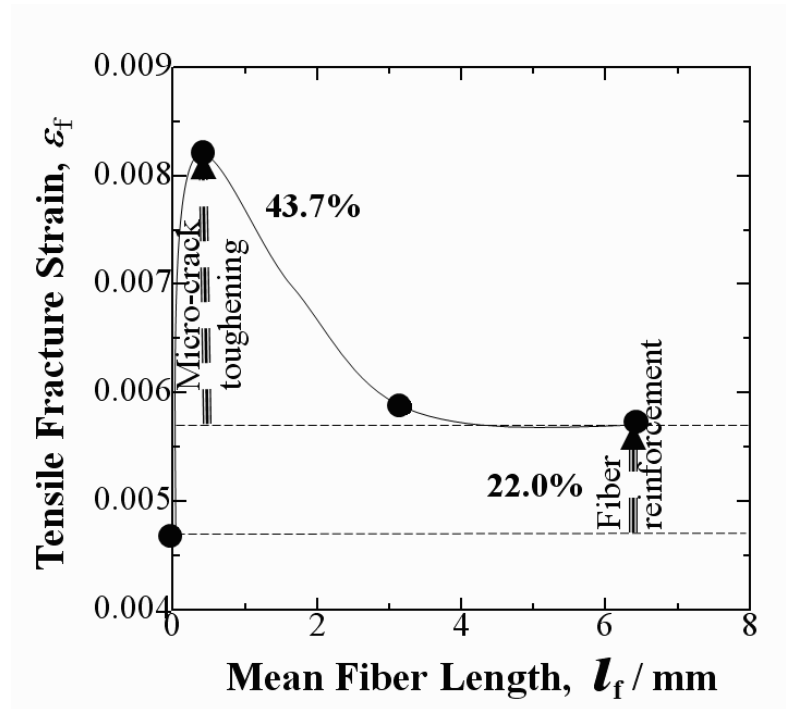
Fig. 7.5 Change in fracture strain, ε_f against mean fiber length, l_f (mm).

Figure 7.5 shows the influence of fiber length on tensile fracture strain of the BMC-GFRP in more detail. The left arrow indicates shortening the fibers from commercial 6.4 mm to sub-millimeter 0.44 mm improved the fracture strain 43.7% from $\varepsilon_f = 0.00572$ to 0.00822. Note this percent increase is higher than the addition of the 6.4 mm fibers themselves at 22%. Moreover, the sub-millimeter 0.44 mm fiber samples exhibited a 40.0% enhancement over the 3.2 mm samples (0.00587). The 0.44 mm fibers increased the ε_f 60% over the glass $CaCO_3$ filled resin which had the lowest strain at 0.00469. Note the hierarchy of fracture strain: 0.44 > 3.2 > 6.4 mm as mean fiber length is shortened.

7.2.2 Influence of fiber length on tensile fracture strength, σ_f
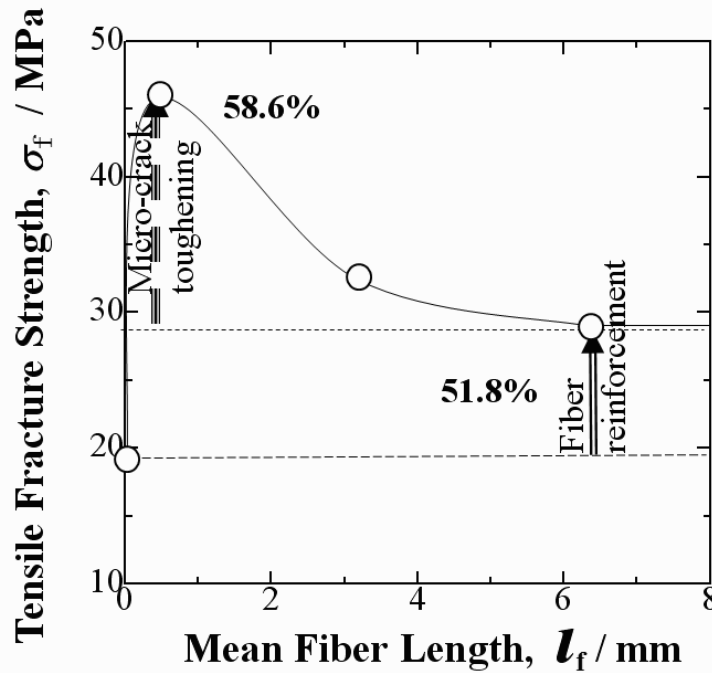
Fig. 7.6 Change in tensile strength (fracture stress), σ_f (MPa) against mean fiber length, l_f (mm).

Quantified in Figure 7.6 is the increase in tensile strength (fracture stress), σ_f (MPa) which resulted from the fracture strain increase. The left arrow indicates shortening the fibers from commercial 6.4 mm to sub-millimeter 0.44 mm improved the fracture stress as well, 58.6% from σ_f = 29.0 to 46.0 MPa. Note again this percent increase is higher than the addition of the 6.4 mm fibers themselves at 51.8%. The strength of the 3.2 mm samples (32.5 MPa) was closer to that of the 6.4 mm samples. Adding the 0.44 mm fibers improved the σ_f 110% over the 0% glass samples which exhibited the lowest value at 19.1 MPa. Fig. 7.6 shows a hierarchy of strength follows the hierarchy of fracture strain: 0.44 > 3.2 > 6.4 mm as fiber length is shortened.

7.2.3 Effect of fiber end density, ρ_E on increasing strength

In E-glass fiber reinforced polymer composites, it is well-documented that fiber ends are common sites for damage [7.3-7.6]. Tyson and Davies found by photoelastic experiments that interfacial shear stresses were higher than theories predict, most notably at the fiber ends [7.3]. Yuan et al. reported debonding at fiber ends was a dominant mechanism in E-glass fiber reinforced PVC [7.3,7.4].

Since matrix damage in the form of crazing and incoherent interface as whitening at fiber ends appears to be a dominant fracture mechanism in toughening the BMC, fiber end density, ρ_E (mm^{-3}) was calculated to quantify its effects on normalized tensile fracture strain, $\varepsilon_f/\varepsilon_{f,6.4}$ and tensile strength, $\sigma_f/\sigma_{f,6.4}$ to show improvement over commercial 6.4 mm samples.

One factor important for toughening is fiber volume fraction, V_f and was held constant at 20 mass% E-glass fibers. Therefore, the fiber end density is calculated from measuring the weight and volume of a given BMC sample to obtain V_f in eq. (7.1) [7.7]:

$$V_f = 0.2 \, m_c/(\rho_g V_c) = 0.1317 \qquad (7.1)$$

where m_c is the mass of the sample (Mg), ρ_g is E-glass fiber density (Mgm^{-3}), and V_c is the sample volume (m^3). ρ_g for E-glass was estimated to be 2.62 Mgm^{-3} [7.8], therefore V_f for the BMC was calculated to be 0.1317.

Total fiber length l_{tot} (mm) is expressed in eq. (7.2) [7.7]:

$$l_{tot} = V_g \, /\pi r^2 \qquad (7.2)$$

where V_g (mm^3) is the volume of glass fiber in 1 mm^3 of composite ($V_g = V_f \, V_c$ =0.1317 mm^3), and r is the fiber radius (7 x 10^{-3} mm). The fiber end density, ρ_E (mm^{-3}) therefore, is calculated in eq. (7.3):

$$\rho_E = 2 \, l_{tot}/l_f \qquad (7.3)$$

where l_f is average fiber length (mm). ρ_E is equal to 3.89 x 10^3, 0.535 x 10^3, and 0.267 x 10^3, mm^{-3} for l_f of 0.44 mm, 3.2 mm and 6.4 mm samples, respectively. Therefore, fiber end density is 13.5 times higher in the 0.44 mm samples than that of the commercial 6.4 mm samples.

Figures 7.7(a) and (b) show the effect of ρ_E on $\varepsilon_f/\varepsilon_{f,6.4}$ (a) and $\sigma_f/\sigma_{f,6.4}$ (b) exhibiting the marked increases in fracture strain and tensile strength with increasing fiber end density. Fig. 7.7(a) shows the trend in normalized fracture strain, $\varepsilon_f/\varepsilon_{f,6.4}$, with respect to the 6.4 mm commercial samples showing the high fiber end density is related to over 40% improvement in fracture strain from 1 to over 1.4. The linear regression obtained is shown [7.7].

$$\varepsilon_f/\varepsilon_{f,6.4} = 1.21\mathrm{x}10^{-4}\rho_E + 0.965 \qquad (7.4)$$

The low ρ_E values are close together therefore the coefficient of determination, R^2 is 1.000.
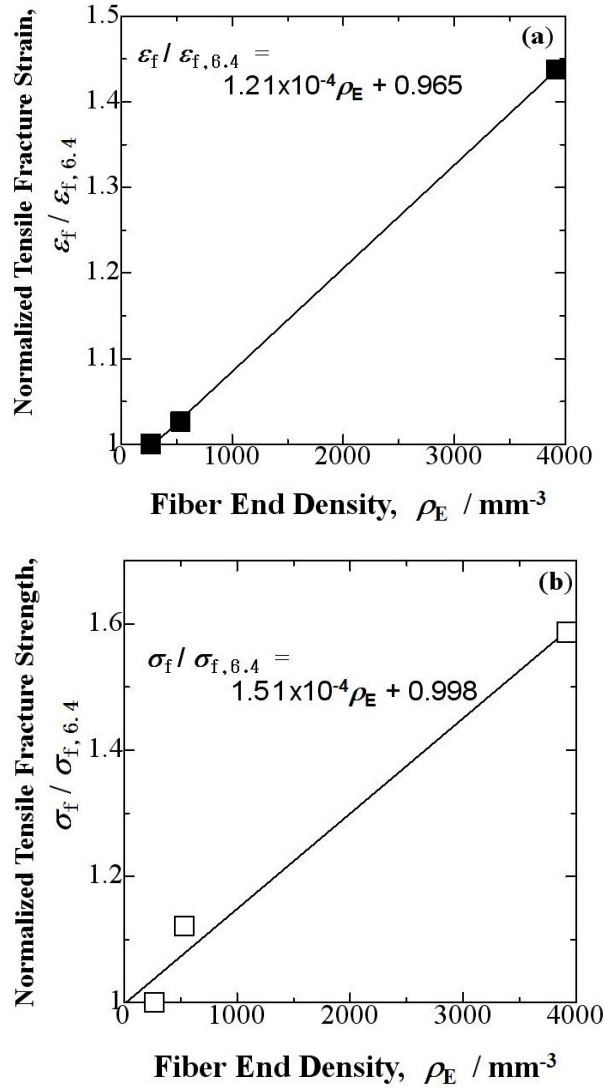
Fig. 7.7 Effect of fiber end density, ρ_E (mm^{-3}) on normalized tensile fracture strain, $\varepsilon_f/\varepsilon_{f,6.4}$ (a) and strength (fracture stress), $\sigma_f/\sigma_{f,6.4}$ (b). Values are normalized to show improvement over the commercial 6.4 mm samples.

Similarly, Fig. 7.7(b) illustrates the effect of fiber end density, ρ_E on normalized tensile strength (fracture stress), $\sigma_f /\sigma_{f,6.4}$. Fig. 7.7(b) shows the nearly 60% improvement from 1 to 1.58 and the linear regression is expressed in eq. (7.5) [7.7]:

$$\sigma_f/\sigma_{f,6.4} = 1.51 \times 10^{-4}\rho_E + 0.998 \qquad (7.5)$$

The low ρ_E values are close together therefore the coefficient of determination, R^2 is 0.983.
. The fourth point for the 0% glass samples was not included in the linear regression calculations. The tensile strength was mainly dominated by fracture strain in the BMC due to increase in microcracking.

7.2.4 Acoustic emission (AE) events as a function of fiber length
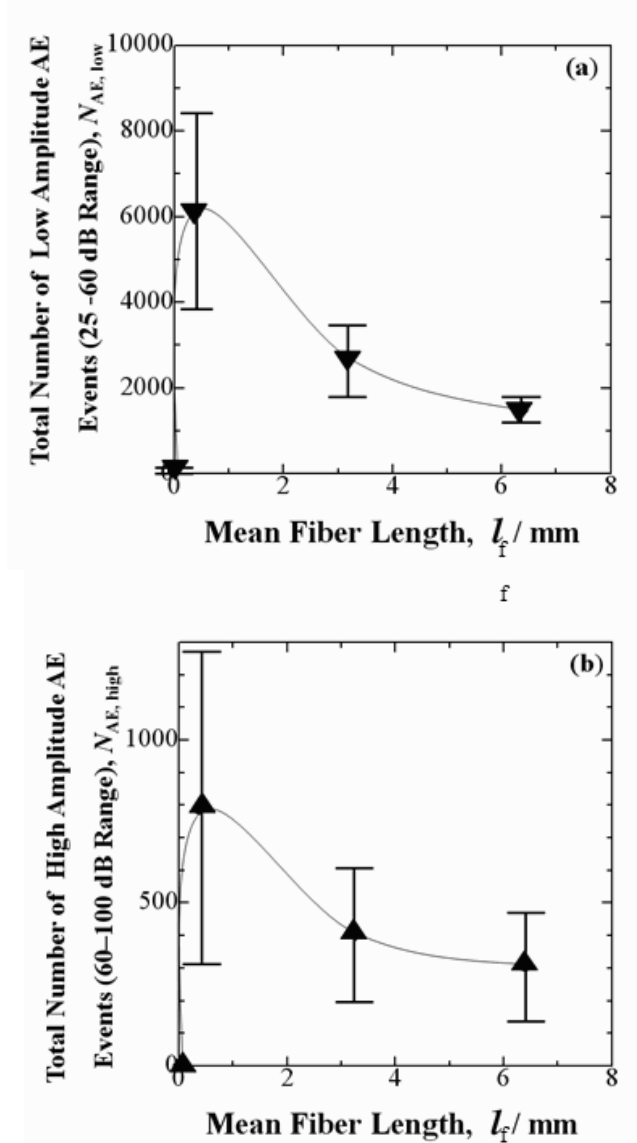
Fig. 7.8 Total number of AE events against mean fiber length, l_f (mm) at low (25–60 dB) (a), and high (60-100 dB) (b) amplitude ranges.

To assess amount of microcracking, acoustic emission (AE) was employed. Pioneered by Kaiser [7.9], AE has been a common tool in investigating damage processes in a wide variety of materials including metals [7.10,7.11] and composites [7.5,7.12].

From the tables reported in Faudree et al. [7.1] Figures 7.8 (a) and (b) compare the number of AE events, N_{AE}, emitted by the BMC during the entire tensile deformation as a function of fiber length, l_f (mm) for the low (25-60 dB) (a) and high (60-100 dB) (b) amplitude ranges more clearly. Bars are standard deviations. Note Figs. 7.8(a) and (b) have the same shape as those in Figs. 7.5 and 7.6, ε_f and σ_f vs. fiber length l_f, exhibiting a strong correlation between microcracking and toughening.

7.2.4.1 Low amplitude AE events

Fig. 7.8(a) shows AE events during the tensile tests in the low amplitude (25-60 dB) range, which have been correlated with small-scale damage such as microcracking and fiber end debonding [7.1,7.5,7.12] but in this case, fiber end crazing. For example, fiber reinforced composites used in dentistry under flexural loading emitted low amplitude AE 25-60 dB events corresponding to polymer matrix cracking [7.12], while Yuan et. al. reported E-glass reinforced PVC undergoing tension emitted AE in the same range, between about 25-60 dB corresponding to fiber-matrix debonding [7.5]. Results of Fig. 7.8 (a) follow the hierarchy in Figs. 7.1, 7.5 and 7.7, as fiber length is decreased, microcracking detected by AE increases along with fracture strain and tensile strength.

Fig. 7.8 (a) illustrates the 0.44 mm BMC samples had more than a threefold increase over the 6.4 mm samples in the 25 dB to 60 dB AE range, $N_{AE, low}$, from under 2,000 to over 6,000 events. This is evidence of the increased microcracking as fibers are shortened to 0.44 mm and supports the SEM results in Figs. 7.2 and 7.3 where low amplitude AE events are correlated with fiber end crazing.

Note Fig. 7.8(a) shows sample-to-sample standard deviations (bars) clearly demonstrate an increase with decreasing fiber length. This is probably due to a wider fiber length distribution in the 0.44 mm samples from the additional mixing where 95% of the population was 0.04 mm $< l_f <$ 0.85 mm (Section 2.7.1). This would increase sample-to-sample AE emission variance, hence, the microcracking rate variance. Note the bottom of the standard deviation bar in the 0.44 mm samples was higher than the top of the bar of the 3.2 mm samples. In the 0.44 mm samples 95% of the population was less than 0.85 mm, still significantly shorter than 3.2 mm, indicating the strong correlation.

7.2.4.2 High amplitude AE events

On the other hand, Fig. 7.8 (b) shows high amplitude AE events ranging from 60-100 dB, which correlate with the fracture energy of the main crack, the large-scale matrix-filler separation and fiber pullout just prior to fracture [7.1]. Fig. 7.8 (b) illustrates the 0.44 mm BMC samples emitted more than two times the high AE events as the 6.4 mm samples in the 60 dB to 100 dB AE range, $N_{AE, high}$: from under 400 to 800. Since average energy per 60-100 dB AE event (E/$N_{AE, high}$) was calculated to be approximately equal for all the fiber-containing samples, total fracture energy of the main crack was higher in the 0.44 mm samples indicating a more jagged pathway through the web of increased microcracking present.

7.2.5 Mechanism of fracture strain improvement by increased microcracking detected as low amplitude AE events
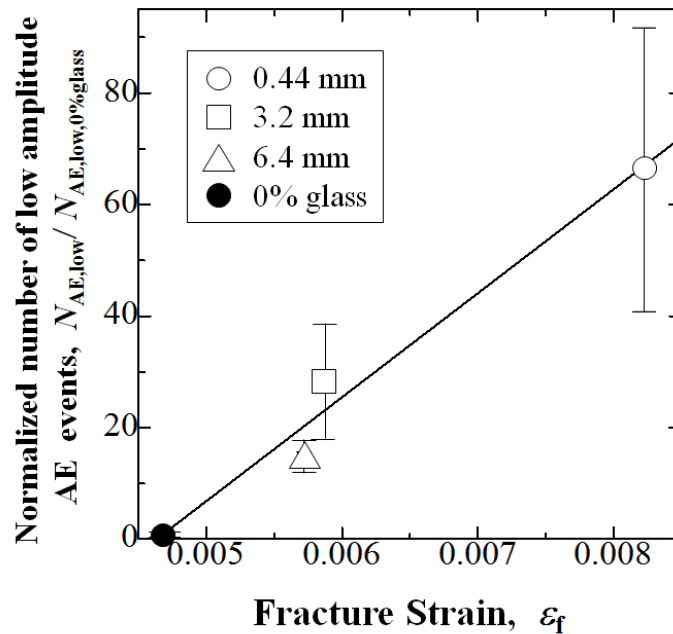

Fig. 7.9 Effect of fracture strain on normalized number of low amplitude (25-60 dB) AE events with respect to the 0% glass samples, for the 0.44, 3.2, 6.4 mm, and 0% glass samples, respectively.

Figure 7.9 illustrates the mechanism of fracture strain improvement by increased microcracking detected as low amplitude AE events. The normalized total number of 25-60 dB AE events with respect to the matrix composite containing 0% glass fibers, $N_{AE,low}/N_{AE,low,0\%glass}$ generated throughout the entire tensile deformation process was evaluated. The 0% glass samples were chosen as a basis to obtain effect of adding the fibers. The normalized low amplitude AE events increased with increasing fracture strain: 15, 28.6 and 66.5 times corresponding with the strains of 0.00572, 0.00587, and 0.00822, in the 6.4, 3.2 and 0.44 mm fiber length samples, respectively. This data shows the increased microcracking is the driving process to improve fracture strain.

7.2.6 'Stepwise microcracking' model
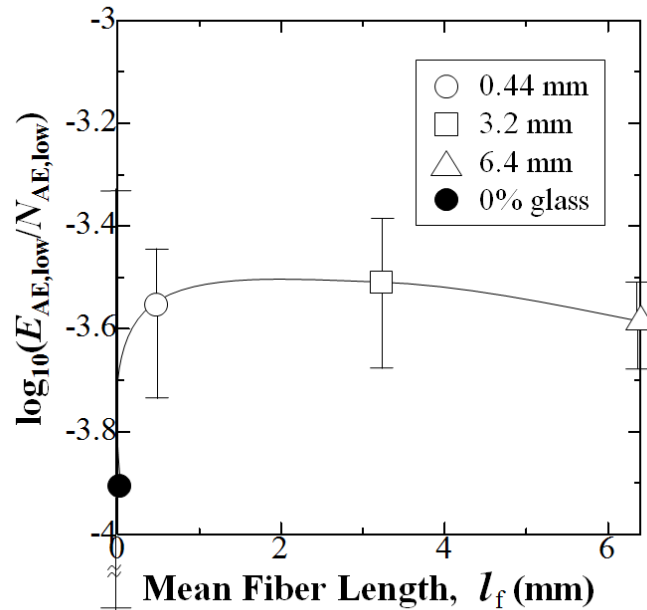
Fig. 7.10 Effect of mean fiber length and 0% glass samples on logarithm of acoustic energy per low amplitude (25-60 dB) AE event. Energy units are arbitrary. Error bars are logarithmic values calculated with respect to the energy standard deviations.

The plot of logarithm of AE energy per low amplitude (25-60 dB) event, $\log_{10}(E_{AE,low}/N_{AE,low})$ against fiber length in Figure 7.10 exhibits a relatively flat curve for the fiber-containing samples, $l_f = 6.4$, 3.2 and 0.44 mm indicating the sums of crack surface areas corresponding to each single low amplitude AE event are approximately equal in size independent of fiber length in the BMC. This would imply for a given AE event, total microcrack surface area generated would be about equal whether many smaller microcracks or one longer microcrack. Moreover, stress relaxation experiments of the BMC show crack propagation occurs in a discontinuous step-wise manner [7.1].
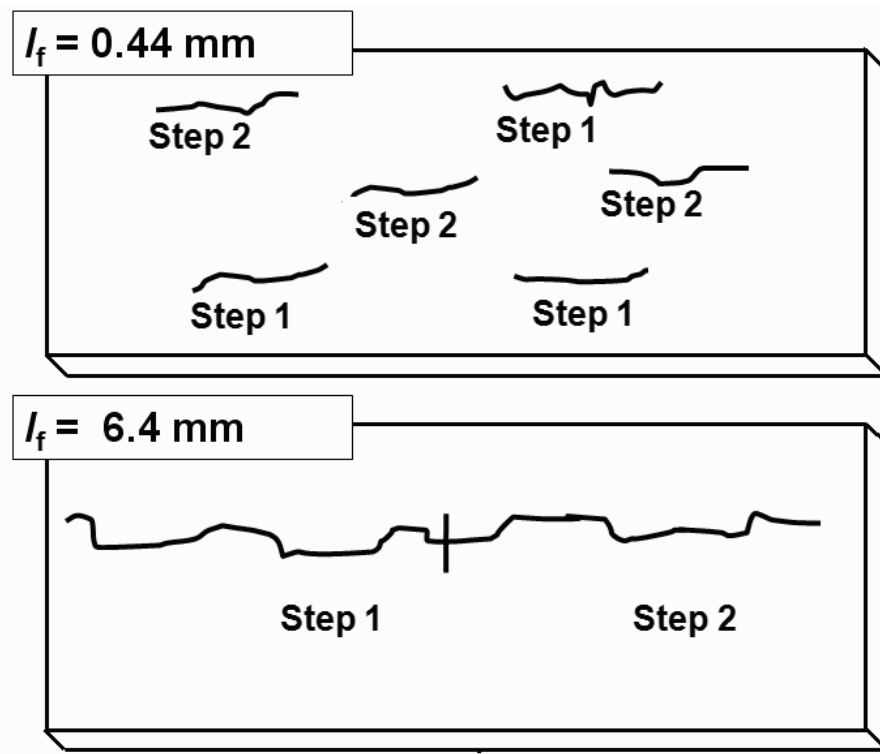
Fig. 7.11 Schematic 'stepwise microcracking' model showing the discontinuous stepwise crack propagation for two AE events in the 0.44 and 6.4 mm fiber length samples, respectively.

Therefore Figure 7.11 illustrates a 'stepwise microcracking' model of the dynamic process of crack formation occurring for two AE events, Step 1 and Step 2. In the shorter fiber 0.44 mm samples, many small cracks are simultaneously generated at different locations (3 x Step 1 ➜ 3 x Step 2), while in the 6.4 mm samples larger microcracks are formed above the critical (Step 1) ➜ (Step 2). In the model the sum of the crack sizes for each step are made identical to represent the approximately equal low amplitude AE energies generated per AE event.

This result suggests microcracks in the 0.44 mm samples are shorter by the higher fiber end density, ρ_E halting cracks when the approach compressive stress sites generated by fiber end crazing. The overall structure of the shorter fiber 0.44 mm BMC is like a net being stretched on a meso-scale to higher strain assisted by the higher fiber end density in the styrene-butadiene elastomeric additive in the BMC.

7.2.7 Linear relationship between number of low AE events and fiber end density
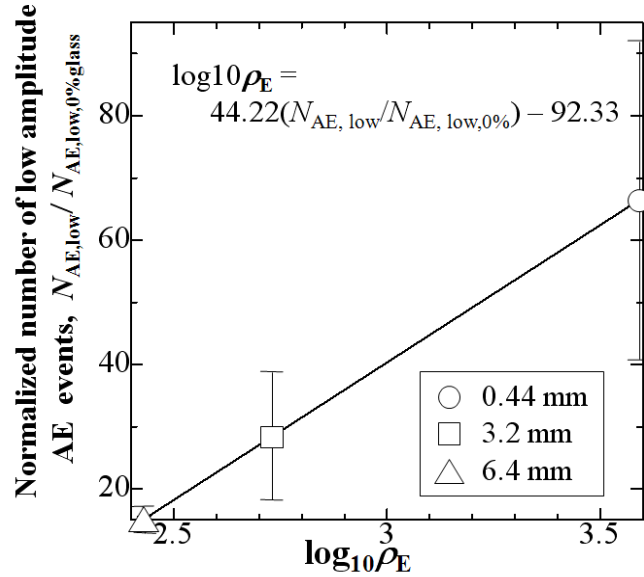
Fig. 7.12 Effect of logarithm of fiber end density per mm^3 of composite on normalized number of low amplitude (25-60 dB) AE events. Correlation coefficient, $R^2 = 0.99996$.

Since low amplitude AE events and fiber end density are closely related, Figure 7.12 shows the plot with normalized number of low amplitude AE events. The linear regression is obtained in eq. (7.6):

$$\log_{10}\rho_E = \quad 44.22(N_{AE,low}/ N_{AE,low,0\% \ glass}) - 92.33 \qquad (7.6)$$

where ρ_E is fiber end density per 1 mm^3 of composite (mm^{-3}), and $N_{AE,low}/ N_{AE,low,0\% \ glass}$ is number of low amplitude events normalized with the number of low amplitude events emitted by the 0% glass samples. A high correlation coefficient, R^2 of 0.99996 is obtained indicating the strong relationship between fiber end density and the microcracking mechanism.

7.2.8 'Fiber end crazing' model

'Fiber End Crazing' Model
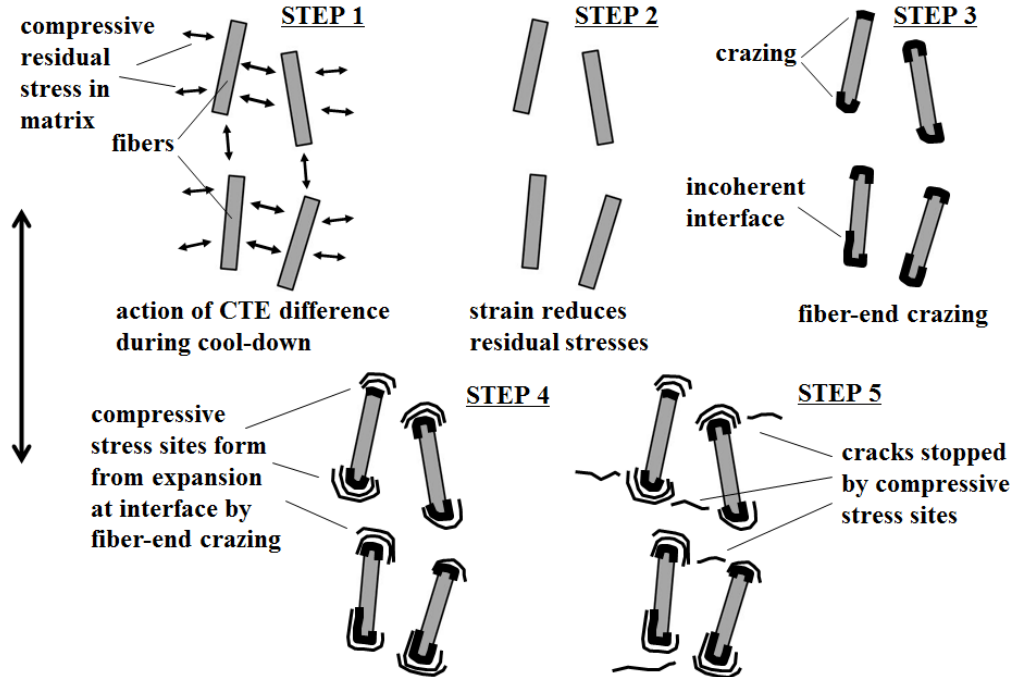
Fig. 7.13 'Fiber end crazing' model.

Fiber end crazing has been found to occur in GFRPs and polymers during deformation as covered in Chapter 1. To explain the increase in microcracking in the shorter 0.44 mm fiber highly-filled GFRP-BMC as detected by low AE events significantly increasing the tensile fracture stress and its strain, a novel "Fiber end crazing' model is constructed for the BMC in Figure 7.13 that has not been previously reported in the literature. SEM observations showed crazing at the fiber ends in the 0.44 mm samples appears to be the dominant mechanism for strengthening by generating compressive stress sites in the matrix halting microcracks below their critical length $2a_c$. Basic principles of fracture mechanics for toughening of materials can explain the enhancement described in Fig. 7.13 by 5 steps based on well-known phenomena.

Step 1: At low deformations CTE difference between matrix and composite dominate where the CTE of the cured polyester resin matrix (55 to 100 x $10^{-6}/°K$) is about an order of magnitude higher than that of E-glass fibers (5.4 x $10^{-6}/°K$). During part cool-down and shrink compressive thermal residual stresses are exerted by the matrix normal to the fibers and fiber ends having components in the tensile σ_{11} direction, raising the tensile modulus (Chapter 6).

Step 2: With increasing strain compressive thermal residual stress of the matrix on the fibers is reduced.

Step 3: Fiber end crazing occurs increasingly in the form of whitening and incoherent interface regions at the stress-concentrated fiber ends as observed by SEM (Figs. 7.2 and 7.3). Weak Van der Walls forces between and within the polymer macromolecules are overcome until the slack is taken out of the covalent bonds in the backbone polymer chain network. The stretched covalent bonds of the crosslinked net deter further widening of the craze region. Crazes

are typically fibrils bridging the craze region which scatter light, hence the white color.

Step 4: Compressive stress sites are formed in the matrix near the fiber ends from volume expansion at the interface by fiber end crazing. Crazing is different than cracking or debonding. While the separation generated between fiber and matrix during debonding cannot carry a load, crazes can carry a load absorbing a high degree of energy from an approaching microcrack.
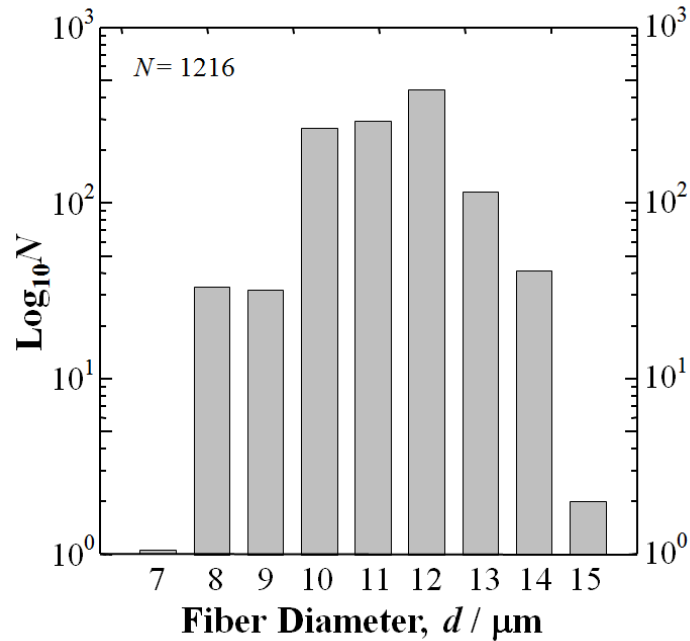

Fig. 7.14 Measured fiber diameter distribution (see Chapter 6).

Step 5: Cracks initiate at or near fiber ends grow normal to the applied stress in Mole I fashion, and terminate at or near the next fiber due to expansive strain fields near the fiber ends from the fiber end crazing adding to the compressive stress from CTE difference around the fibers. A large amount of energy is absorbed through the fiber end crazing and microcracking, maintaining crack length below the critical $2a_c$ increasing tensile strength and strain. Steps 1 through 5 can occur simultaneously in localized regions.

The crazing appears since the E-glass fibers in the BMC are coated with a strong coupling agent where the matrix and fiber do not separate easily. Since measured fiber diameter of over 1,200 fiber cross sections by SEM (Figure 7.14), d=11.6 mm is smaller than the nominal fiber d=14 mm, the remaining 1.2 mm coating around the fibers appears well absorbed in the matrix and contributes to the crazing sites.
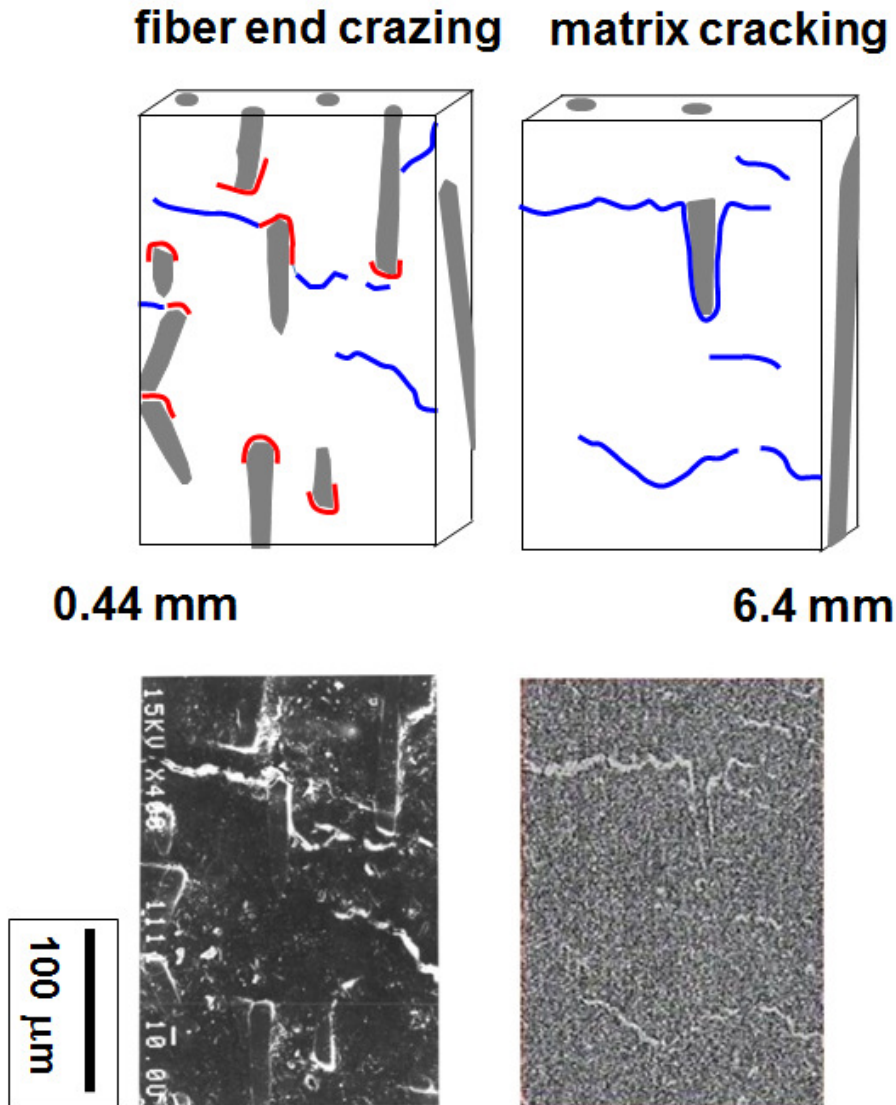
Fig. 7.15 Schematic of dominating damage mechanisms comparing the 0.44 and 6.4 mm samples drawn identical to typical SEM photos.

Figure 7.15 is a schematic drawn identical to SEM illustrating the fiber end crazing mechanism comparing the 0.44 mm with the 6.4 mm commercial composite. In the 0.44 mm samples, SEM observation shows fiber end crazing appears as the dominant damage mechanism. Microcracks appear to be halted and relaxed at fiber end sites. On the other hand, SEM photos of the 6.4 mm fiber length samples show matrix cracking as the dominant mechanism [7.13]. Since generally, in both cases there appears Mode I crack growth the higher density of fiber ends by fiber end crazing keeps cracks below the critical $2a_c$ in the sub-millimeter fiber samples absorbing more energy, increasing the tensile properties.

7.2.9   3-dimensional schematic of 'fiber end crazing' model
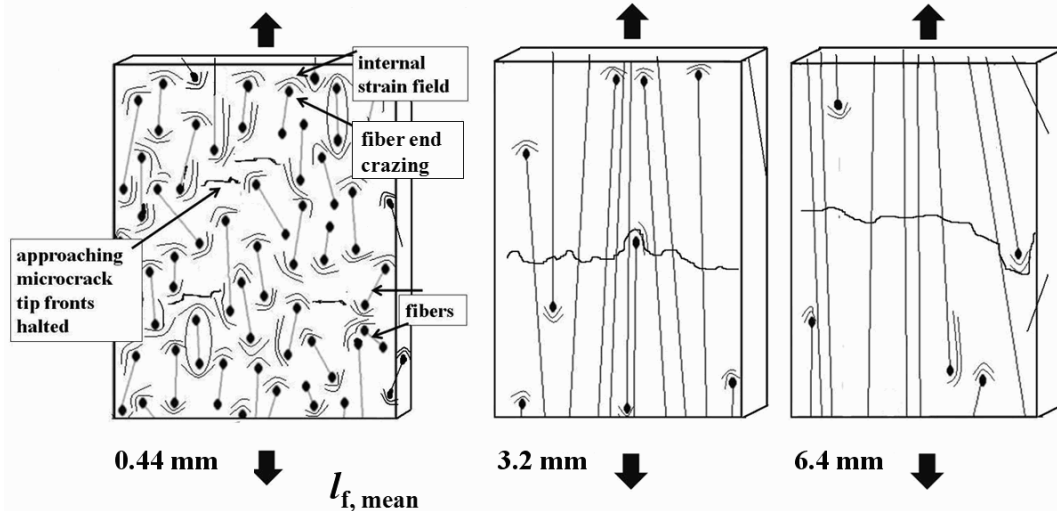
Fig. 7.16   Three-dimensional schematic showing higher fiber end density, ρ_E(mm^{-3}) in the 0.44 mm samples initiating compressive stress sites, which absorb energy approaching crack tip fronts halting the cracks.

Figure 7.16 illustrates a three-dimensional schematic of crazing at fiber ends imparting an internal strain field in the matrix surrounding each fiber resulting in volume expansion into compressive stress sites which absorb energy from an approaching microcrack tip front in the nearby vicinity halting the crack's advance. In the higher fiber end density 0.44 mm samples, the mean distance cracks can propagate is shorter keeping stress below the critical. On the other hand, in the 3.2 and 6.4 mm samples, cracks propagate longer distances without encountering a compressive site going around fibers reaching above the critical length $2a_c$. The graph in Figure 7.17 depicts crack propagation being reduced from increased micro-compressive stress sites in the matrix. This is approximating Mode I crack propagation occurs in general [7.14]. The principle of physics when a medium in which another medium is dispersed still retains its properties although it is affected by the dispersed medium interacting with it. When shortening the dispersed medium of E-glass fibers in an unsaturated polyester/styrene butadiene GFRP-BMC composite the matrix fracture toughness K_{IC} value and its critical crack length, $2a_c$ appear to be maintained.
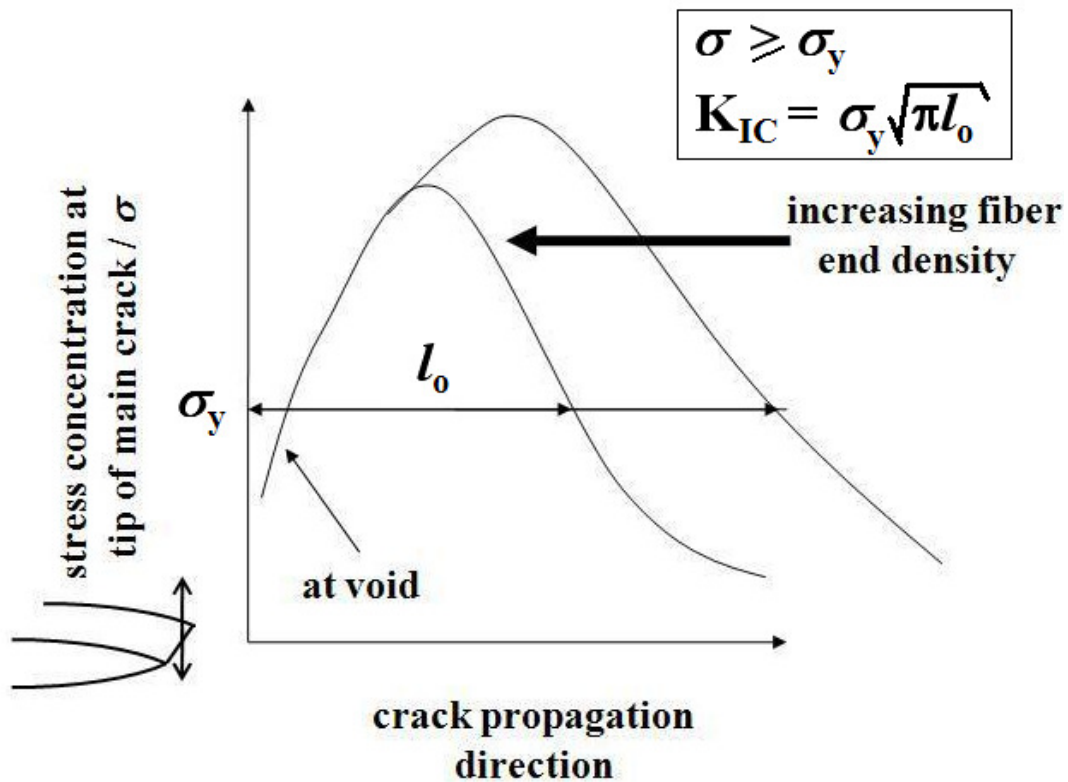
Fig. 7.17 Schematic of crack propagation length, l_o being reduced from increased micro-compressive stress sites in the matrix [7.14].

.

Microcracks would have to twist and turn to get around the relaxed areas but twisting and turning tend to close the crack [7.14]. In addition, the average distance between stress relaxation sites is decreased below the minimum $2a_c = 0.50$ mm for polyester resin in the shorter fiber environment, more cracks are stopped, thus more microcracks can be tolerated increasing the fracture strain. In addition, the increased microcracking in the vicinity of the main crack tip acts to lessen the main crack tip stress concentration. All of these serve to prevent crack propagation resulting in enhancement of fracture strain and stress markedly in the BMC-GFRP.

7.3 Conclusions

(1) This chapter focused on the novel and most important finding of this dissertation not previously reported in the literature that shortening fibers (rather than lengthening) in FRP from commercial 6.4 mm to submillimeter 0.44 mm significantly increased tensile strength, σ_f (58.6%) and its strain, ε_f (43.7%) in a highly-filled injection-molded GFRP-BMC.

(2) A novel "fiber end crazing' model was constructed that has not been previously reported in the literature. It is based on SEM observations that showed crazing at the fiber ends in the 0.44 mm samples appearing as whitening and coherent interface. The crazing appears to be the dominant mechanism for strengthening by generating compressive stress sites in the matrix halting microcracks below their critical length $2a_c$.

(3) The critical crack length range for thermoset polymers was calculated to be approximately $0.50 < 2a_c < 5.0$ mm from reported K_{IC} results in the literature. The probability of a microcrack propagating above 0.44 mm before it encounters a matrix compressive site, therefore is reduced.

(4) Fracture stresses and strains showed a strong relationship with fiber end density.

(5) Acoustic emission (AE) along with scanning electron microscopy (SEM) results showed the dominant damage mechanisms were increased density of small cracks, mainly fiber end crazing in the 0.44 mm samples and microcracking at and around fibers in the 6.4 mm samples.

(6) The number of low amplitude AE events (25-60 dB) showed a positive correlation with fiber end density.

(7) The improvement in the fiber-containing samples can be explained by increased internal strain fields surrounding each fiber end and along the length upon deformation from fiber end crazing resulting in localized volume expansion sites in the matrix, making compressive stress sites, which absorb energy from an approaching crack tip front in the nearby vicinity halting its advance. As a result, more microcracks can be tolerated. Moreover, increased microcracking in the vicinity of the main crack tip acts to reduce the main crack tip stress concentration.

(8) The relationship between logarithm of fiber end density, ρ_E (mm^{-3}) and log10 of normalized number of low amplitude AE events in the 25-60 dB range ($N_{AE,low}/N_{AE,low,0\% glass}$) exhibited a high linear correlation of 0.99996.

REFERENCES

[7.1] Faudree M., Hiltner A. and Baer E. and Collister J., J. of Compos. Mater., **22 (**1988**)** 1170-1195.

[7.2] Sato N., Kurauchi T., Sato S. and Kamigaito O., J. J. Mater. Sci. Lett. **2** (1983) 188.

[7.3] Tyson W. and Davies G., Br. J. Appl. Phys. **16** (1965) 199-206.

[7.4] Yuan J., Hiltner A. and Baer E., J. Mater. Sci. **20** (1985) 4377-4386.

[7.5] Yuan J., Hiltner A. and Baer E., Polym. Compos. **7** (1986) 26-35.

[7.6] Rahrig D., Gianelos J., Yuan J., Baer E. and Hiltner A., Proc. SPI RP/C 40th Annual Conference, 21F (1985).

[7.7] Faudree M. and Nishi Y., Mater. Trans. **51** (2010) 2304-2310.

[7.8] Bauccio M., Ed.: *ASM Engineered Materials, Reference Book, 2nd Edition* (Materials Park, Ohio: ASM International) (1994) 97.

[7.9] Kaiser J., Archiv. F. Eisenhuettewesen, **24 (**1953) 43.

[7.10] Sedlak P., Hirose Y., Khan S., Enoki M., and Sikula J., Ultrasonics, **49 (**2009) 254-262.

[7.11] Rossoll A., Otto C., Moser B., Weber L., Wanner A., and Mortensen A., Scripta Mater. **59** (2008) 842-845.

[7.12] Alander P., Lassila L., Tezvergil A., and Vallittu P., Dental Mater. **20** (2004) 305-312.

[7.13] K. Seol A, Krawitz A., Richardson J., Weisbrook C., Mater. Sci. and Eng. **A 398** (2005) 2846-2851.

[7.14] Kishi T., Ceramics **27** (1992) 311-315.

Chapter 8

Characterization of velocity profile to assess flowability of shortened 0.44 mm fiber SGFRP-BMC paste

[*Characterization of Velocity Profile of Highly-Filled GFRP-BMC through Rectangular Duct-Shaped Specimen during Injection Molding from SEM Fiber Orientation Mapping*]

ABSTRACT

To investigate the feasibility of processing using the short-fiber 0.44 mm GFRP-BMC paste for possible industrial use, velocity profile and rheological parameters in the injection-molded sample has been investigated by means of fiber orientation mapping by SEM. There is an extensive body of research and texts on numerical simulation to obtain rheological properties of injection molded resins and composites, however to our knowledge there is no or little research on estimating velocity profile from fiber orientation mapping of GFRP-BMCs (glass fiber reinforced polymer bulk molding compounds). This study reports a simple analysis of specific laminar creep flow properties of highly-filled short-fiber GFRP-BMC through a dogbone specimen as a rectangular duct during injection molding from SEM fiber orientation mapping which is found to exhibit a 3-layer [skin-core-skin] structure resembling classical laminar flow through a conduit. Therefore, to characterize the BMC with extremely low Reynolds number ~2 x 10^{-4}, velocity profile, primary and secondary boundary layers were estimated from Hermans fiber orientation parameter across gauge section thickness. The fiber mapping could possibly be used as an additional evaluation to obtain a rough or better estimation of actual flow patterns and velocities to later simulate or optimize entire molding process by computer simulation. Moreover, this method shows good mold flow conditions for processing the shortened 0.44 mm fiber length BMC paste in industry.

8.1. Results
8.1.1 Mapping position across sample thickness and fiber orientation angles

Figures 6.7, 2.18 and 2.19 along with eq. (12) are shown for convenience to depict the basis of this study fiber orientation mapping across specimen thickness obtaining velocity profile and rheological parameters. Fig. 6.7 shows position of mapping of SEM photomicrographs across the 3.3 mm thickness for GFRP-BMC specimen perpendicular to mold flow direction z-axis. This was sectioned into 24 areas from 1 to 24 to obtain effect of position across thickness.
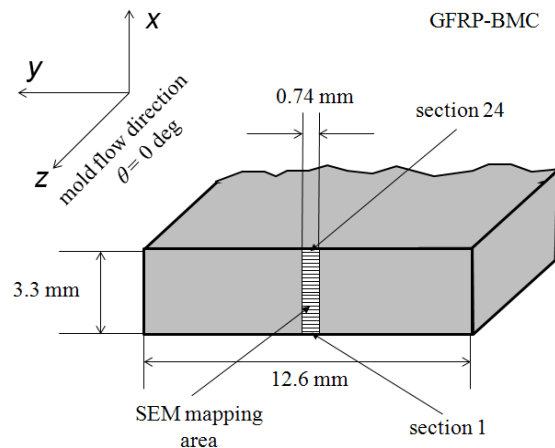
Fig. 6.7 Position of SEM mapping site on cross-section normal to the mold flow direction of GFRP-BMC sample in gauge length (from Chapter 6).

Figures 2.18 and 2.19 show fiber orientation with respect to the tensile/molding direction calculated by eq. (8.1) [8.1]:

$$\theta = \arccos(a/b) \tag{2.12}$$

8.1.2 Mold-flow pattern from fiber orientation angle, θ with respect to mold flow direction across specimen thickness
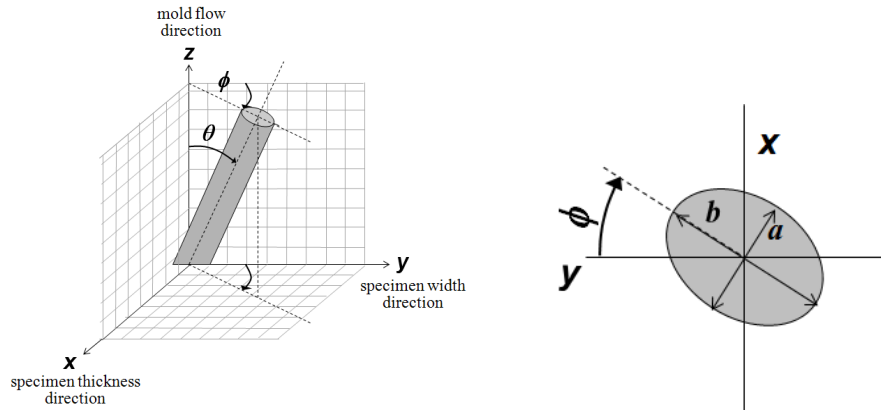
Figs. 2.18 and 2.19 Fiber orientation in spherical coordinates as a function of θ and ϕ: angles (deg) with respect to the molding direction z-axis and width direction y-axis of sample, respectively (from Chapter 2).

Figure 8.1 shows the fiber cross-section mapping with respect to the tensile/molding direction, which to our knowledge is the first time GFRP-BMC composites fiber orientation map is illustrated in the literature. Since the BMC is opaque and has low contrast between fiber and matrix, Fig. 8.1 is the mosaic of SEM photomicrographs put together where θ are measured by sizing and positioning ellipses over the fiber cross sections using power point computer program. Mold flow direction is normal to the plane of the page. Across the 3.3 mm thickness fibers appear to have a fountain configuration, the center fibers appearing to have been pushed out perpendicular with respect to the flow at highest velocity decreasing near or to zero near the mold walls. Fiber density distribution is inhomogeneous. There are fiber-rich areas in most sections while notably sections 4-6 have low fiber density. Some fibers appear to have been bent in sections 6-8 or broken during the mixing and the injection molding process.

8.1.3 Fiber orientation angle, ϕ with respect to width direction

Figure 8.2 shows average measured angle, ϕ (deg) with respect to y-axis, parallel to specimen width for each section through thickness, th [8.2]. Standard deviations (deg, in brackets) show variations in ϕ are wide due to the fountain flow nature of the BMC paste. Interestingly, the average ϕ do not deviate much from the width direction, showing the shorter dimension (th = 3.3 mm) controls, or squeezes the flow patterns. Note these standard deviations in angle ϕ do not designate the preciseness of the ellipse measurement, they merely show variation in flow. Ellipse measurements are quite accurate to +/-650 nm and are described in the introduction yielding +/-5.7% and +/-2.8% for ellipse short and long axes (a and b), respectively.
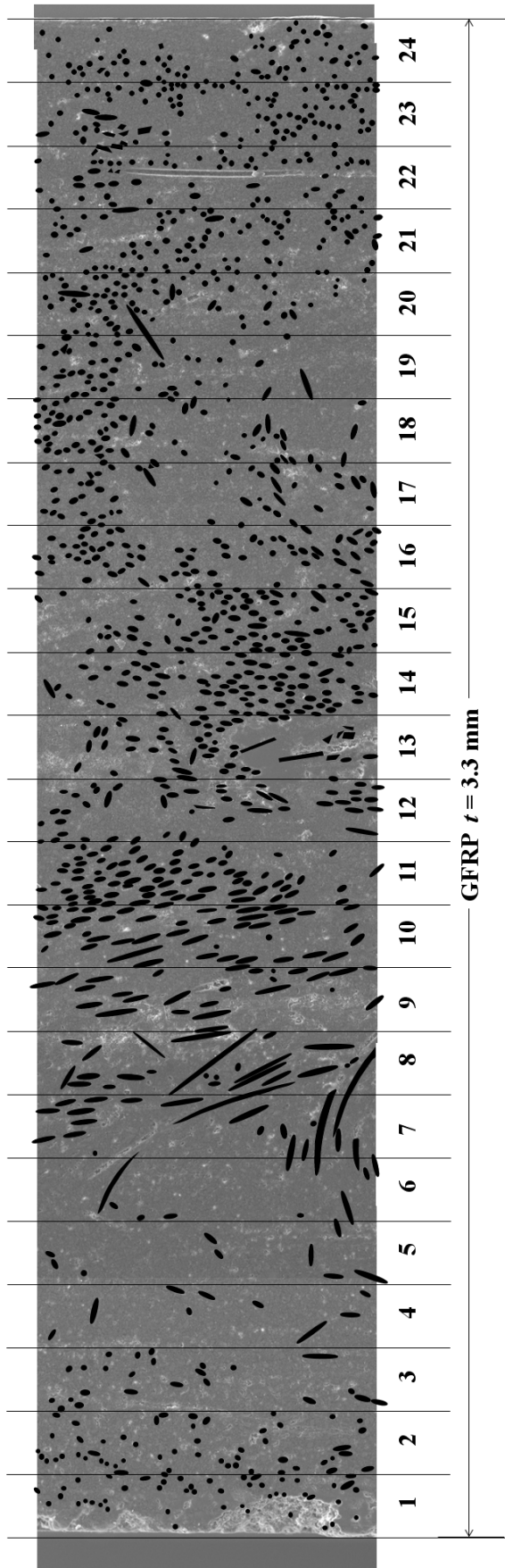
Fig. 8.1 Mapping of cross-section of GFRP-BMC across specimen thickness. Tensile/molding direction is normal to the plane of the page.
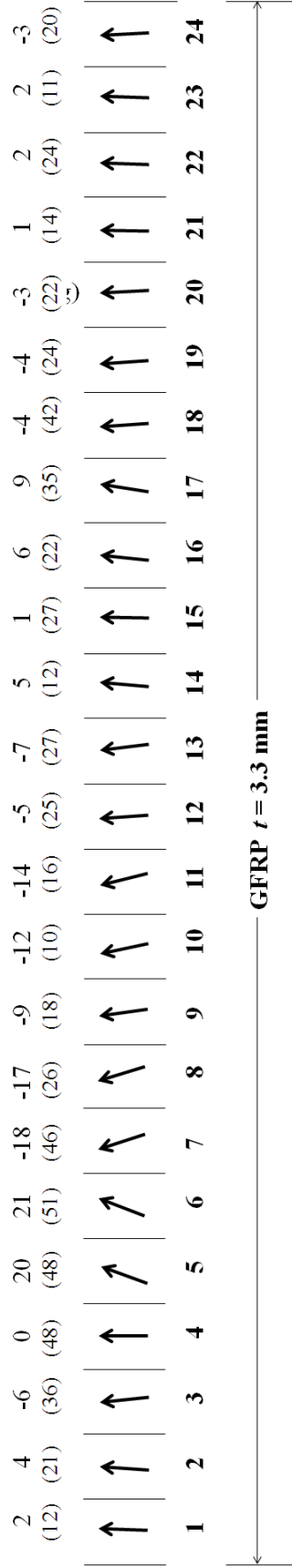
Fig. 8.2 Measured angle, ϕ (deg) with respect to y-axis, parallel with specimen width for each section through thickness. Standard deviations are in brackets

8.1.4 Measurement of fiber angles, θ and ϕ by SEM

   Figure 8.3 shows an SEM micrograph at higher magnification near the mold wall where many fibers are highly oriented to the mold flow direction. The three marked fibers (lines) to the left have ratio of ellipse long and short axes b/a = 1.18, 1.26 and 1.21, hence θ =32.0, 37.2 and 34.6 deg, from mold flow direction respectively, while angle with respect to y-axis width direction, ϕ = 4, -5 and -10 deg. The three marked fibers to the right have b/a = 1.016, 1.030 and 1.052, thus θ = 10.4, 13.9 and 18.1 deg, while their ϕ = -1, 2 and 0 deg, respectively.
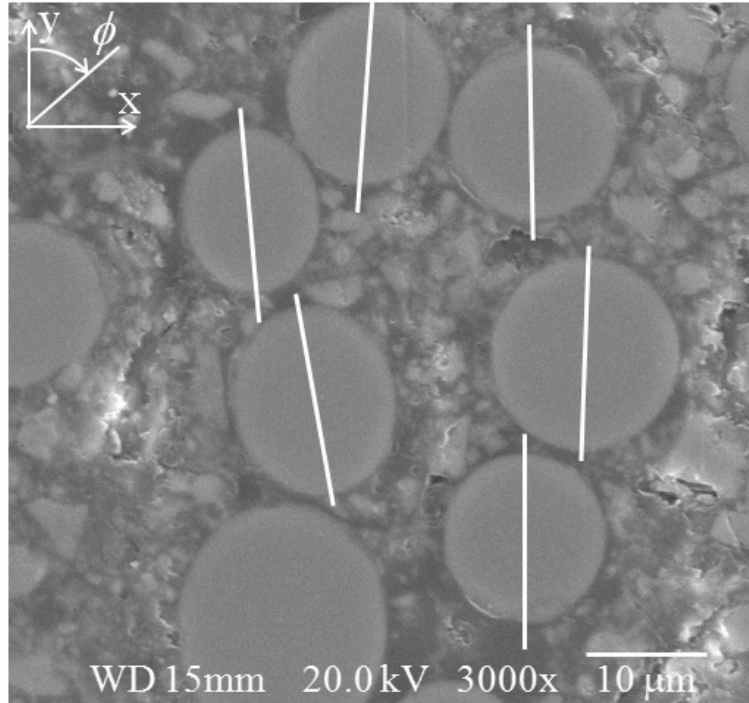
Fig. 8.3 SEM micrograph showing highly oriented fiber cross-sections near the mold wall. Mold flow z-direction is normal to the plane of the page.

   Figure 8.4 shows an area near the center of the specimen thickness where fibers are oriented more perpendicular to the mold flow direction with marked fibers from left to right having b/a = 5.24, 10.81 and 5.80, respectively, hence θ = 79.0, 84.7 and 80.1 deg, with ϕ = -13, -17 and -18 deg.
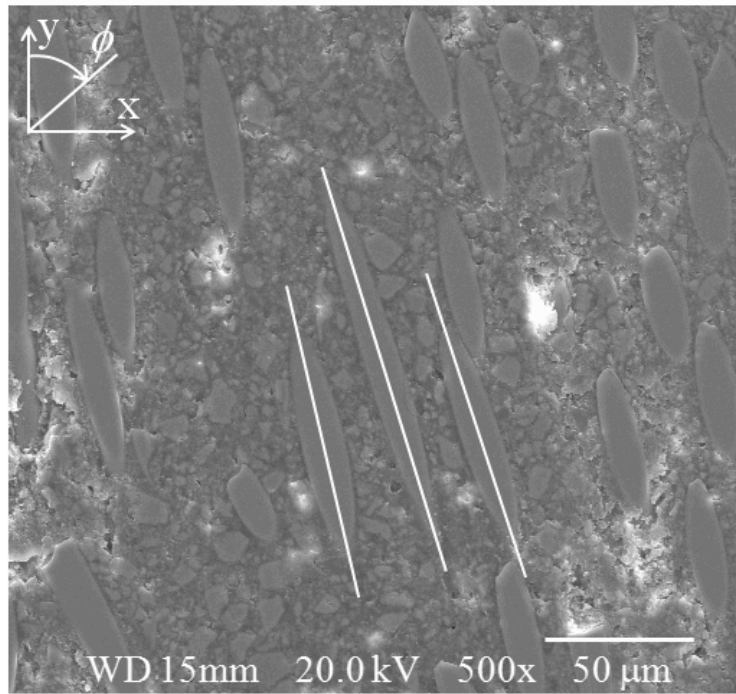
Fig. 8.4 SEM micrograph showing fibers oriented more perpendicular to the mold flow direction near the center of the thickness.

8.2 Discussion
8.2.1 Velocity calculation in specimen
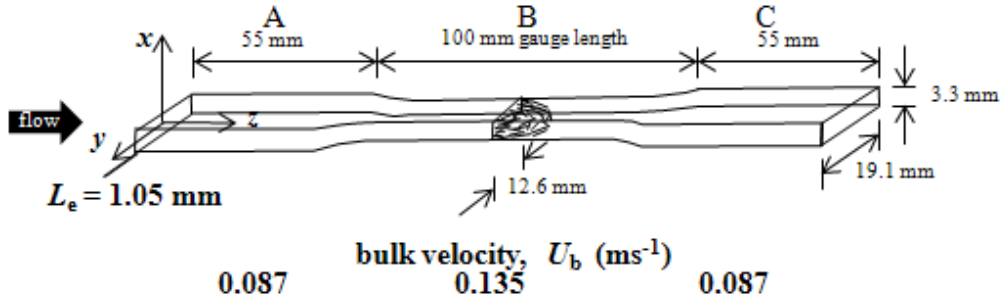
Fig. 8.5 Schematic of laminar creep flow of GFRP-BMC paste through specimen during injection molding illustrating 3-D elliptical paraboloid wavefront in gauge length.

Figure 8.5 shows flow through the ASTM D-638 dogbone specimen. Flow is from sections A ➔ B ➔ C. For simplicity, velocities were calculated ignoring the taper and possible backflow in 'C' section. Hence, time to fill the 100 mm gauge length cavity B-section, t_B is in eq. (8.1) calculated as:

$$t_B = t_s(V_B/V_{tot}) \qquad (8.1)$$

where t_B, t_s , V_B and V_{tot} are: time to fill B-section (0.741s), total shot time (2.0 s), B-section volume (4165 mm^3) and total specimen volume (11,245 mm^3), respectively. This yields B-section bulk velocity, $U_{B = }U_b$ (ms^{-1}):

$$U_b = L_B/t_B \qquad (8.2)$$

where L_B is 100 mm gauge length, therefore U_b = 0.135 ms^{-1}. Velocities of wider sections A and C were 0.0874 ms^{-1}.

8.2.2 Reynolds number and laminar creep flow

To characterize the flow pattern in relation to other fluids, pipe sizes and geometries the dimensionless Reynolds number is useful:

$$Re = \rho U_b D_H/\eta_b \qquad (8.3)$$

When ρ is density of paste (kgm^{-3}) assumed to be equal to that of the solid finished part (1725 kg/m^3), U_b is bulk velocity (ms^{-1}), D_H is hydraulic diameter, and η_b is bulk viscosity (5.0x10^3 Pas) of the non-Newtonian paste, the estimated Reynolds number is 2.44 x 10^{-4} in the gauge length and 1.73 x 10^{-4} in wider sections 'A' and 'C' characteristic of viscous laminar creep flow [8.3].

8.2.3 Velocity profile, primary ($\delta_{0.99Uc}$), and secondary (δ_f) boundary layers

The assumption made here is fiber orientation at a location through the thickness correlates with velocity at that location setting no-slip boundary velocity of zero at

mold walls. Total bulk velocity, U_b is set at the 0.135 ms-1 since time to fill the mold is ~2s. The fiber orientation at a point is actually dependent on the history of velocity gradients the fibers experience up to the point measured, however, those near the core center tend to be more perpendicular to the molding direction indicating an approximately parabolic wavefront pushing the fibers more perpendicular to the wavefront. To get velocity profile from θ, for each section 1 to 24 in Figs. 6.7 (Chapter 6) and 8.1, Hermans fiber orientation parameter, $\eta_o = [\cos^2(\theta)]$ is employed where θ are obtained from eq. (2.12) as in Figs. 8.3 and 8.4. The average orientation parameter for each section from 1-24, can be calculated in eq.(8.4) [8.1, 8.2]:

$$\eta_{o,j} = \Sigma_{ij}[N(\theta_{ij})\cos^2(\theta_{ij})]/\Sigma_{ij}[N(\theta_{ij})] \qquad (8.4)$$

where $N(\theta_{ij})$ is number of fibers in each section, and i and j are fiber, and section number, respectively. Hence, velocity for each section, v_j is estimated from U_b. To fit data to inverted parabola, orientation parameter is inverted $(1-\eta_{o,j})_{avg}$ in eq.(8.5):

$$v_j = [U_b/(\Sigma_j[N(\eta_{o,j})(1-\eta_{o,j})]/24)](1-\eta_{o,j}) \qquad (8.5)$$

where $(1-\eta_o)_{avg} = (\Sigma_j[N(\eta_{o,j})(1-\eta_{o,j})]/24)$. Figure 8.6 shows the velocity profile obtained normalized for $U_b = 0.135$ ms^{-1}; showing centerline mean ($U_c = 0.180$ ms^{-1}) and maximum velocities, ($U_{max} = 0.202$ ms^{-1}), respectively.
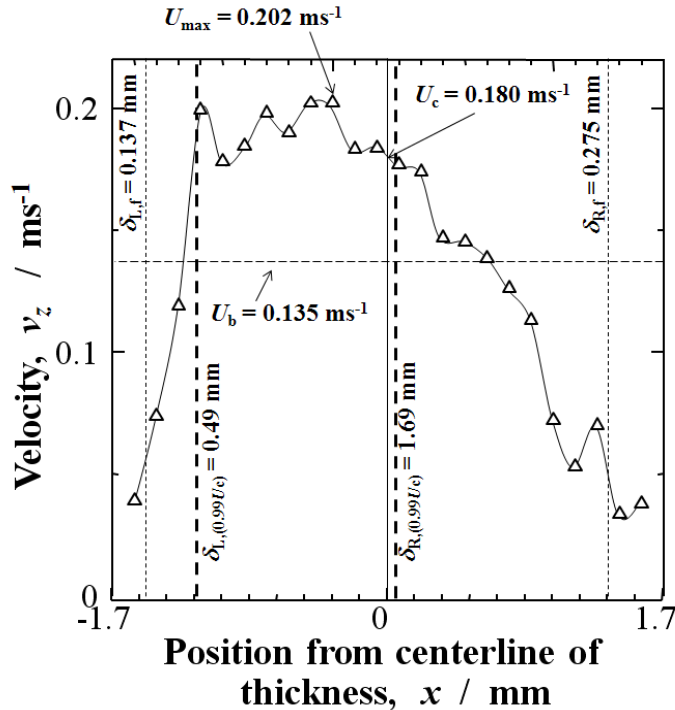
Fig. 8.6 Calculated velocity profile of GFRP-BMC flowing through gauge section of mold showing primary ($\delta_{0.99Uc}$), and secondary (δ_f) boundary layers for left (L) and right (R) specimen walls, respectively.

Assigning primary boundary layer as that of flow, past research indicates it would be quite thick since as Re number decreases boundary layer thickness increases due to the large viscous displacement effect [8.3].

To estimate δ for the GFRP-BMC flowing through the rectangular duct therefore, we follow the tradition of taking the points on the experimental curve of Fig. 8.6 that are 99% of the centerline velocity, $0.99U_c$ [8.4]. Graphical interpolation for designated left and right sides yields $\delta_{0.99Uc,(L)}$ and $\delta_{0.99Uc,(R)}$ = 0.49 and 1.61 mm ($\delta_{0.99Uc,(avg)}$ = 1.05 mm), respectively encompassing ~67% of the thickness. This is characteristic of the laminar creep flow of the highly viscous BMC.

In addition, we define a secondary boundary layer, δ_f for fiber reinforced composites as the distance from the mold walls in which fibers remain highly oriented with the flow, agreeing with other composite systems [8.5,8.6]. This is done simply from the "skins" in Fig. 8.6 as: $\delta_{f,(L)}$ and $\delta_{f,(R)}$ = 0.14 and 0.27 mm, respectively, hence $\delta_{f,(avg)}$ = 0.20 mm. Here fibers are θ = 0 to 20 deg with respect to the mold flow direction. This is apparent in the mosaic of Fig. 8.1.

8.2.4 Parabolic velocity profile fit from experimental values
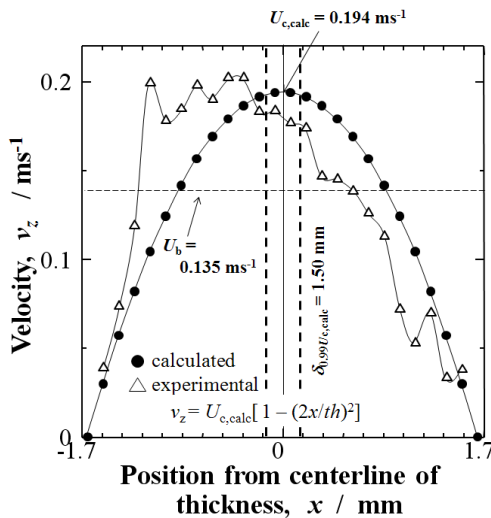
Fig. 8.7 Parabolic profile fit across the 3.3 mm specimen thickness.

Fig. 8.8 Measured fiber density, $\rho_{f(A)}$ perpendicular to molding direction across specimen thickness. Average, $\rho_{f(A),avg}$ (solid line); and that calculated from the E-glass fiber volume fraction (V_f), $\rho_{f(A),calc}$ (dotted line) are indicated.

To solve for the Navier-Stokes equations, the experimental data is fit to a parabolic velocity profile in which the sum of velocities, v_i must equal that from the experimental data. Figure 8.7 shows the parabolic plot of eq.(8.6):

$$v_z = U_{c,calc}[1 - (2x/th)^2] \qquad (8.6)$$

where iteration yields calculated centerline velocity ($U_{c,calc}$) of 0.194 ms^{-1}. Although the positions of the experimental maximum velocities are higher and lower than the calculated parabolic fit on left and right sides respectively of Fig. 8.7, the parabola appears to be a decent approximation of the 3-layer flow.

8.2.5 Effect of fiber density gradients on velocity profile

The difference between the experimental and calculated velocity profiles can be

explained by Figure 8.8 where higher velocities above that of the parabolic fit are accompanied by lower fiber densities, $\rho_{f(A)}$ below the average ($\rho_{f(A),avg}$) of 498 mm^{-2} (solid line) in sections 3 to 10. The low ρ_f appears to allow the paste to flow faster through the mold causing the sparse fibers to be pushed out at higher angles perpendicular to the flow as shown in the Fig. 8.1 exhibiting a fountain configuration. On the other hand, on the right side of Fig. 8.8 lower velocities are accompanied by higher $\rho_{f(A)}$ above $\rho_{f(A),avg}$ in sections 12 to 23 causing higher resistance to flow and lower velocities than the parabolic fit.

For the parabolic fit, boundary conditions $v_z = 0$, are set at mold walls $x = +/-th$. Fig. 8.7 shows calculated primary boundary layers $\delta_{0.99Uc,calc}$ are 1.50 mm (3.00 mm total) extending throughout most of the thickness.

8.2.6 Approximating effective viscosity, η_{eff} at mold walls by steady-state Navier-Stokes equation
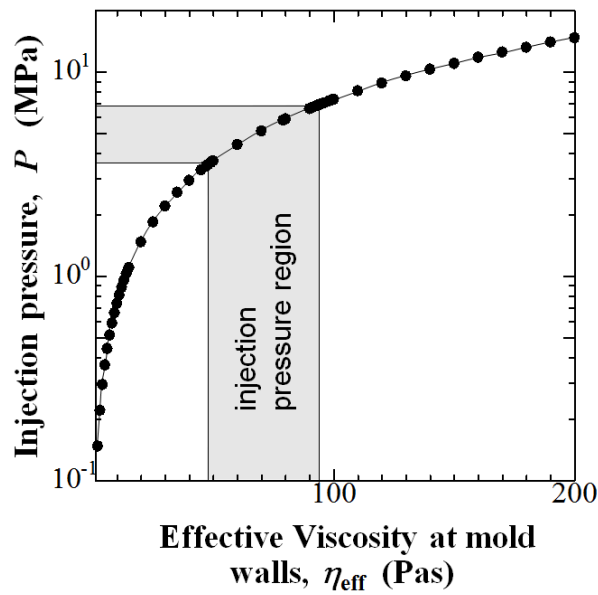
Fig. 8.9 Effective viscosity at mold walls calculated for injection pressure from the Navier-Stokes equation.

Picturing the BMC paste as forming a thin melt layer with lower viscosity within δ_f at the mold walls assisting to push the ultra-high viscosity core into the mold; it seems logical effective viscosity, η_{eff} at the mold walls can be estimated from injection pressure, δP using the Navier-Stokes equation. For flow along the z-axis [8.3]:

$$\rho g_z - \delta P/\delta z + \eta(\delta^2 v_z/\delta x^2 + \delta^2 v_z/\delta y^2 + \delta^2 v_z/\delta z^2) = \rho(dv_z/dt) \qquad (8.7)$$

where the terms are: gravitational, pressure, viscous, and acceleration forces per unit volume. Although the paste is a non-Newtonian shear thinning fluid [8.7] and there are temperature gradients, this is beyond the scope of this study and seems to be taken into account in the frozen fiber orientation. Since the density of the thick BMC paste is approximately equal to that of the molded product because it contains 67.1 mass% hard components of glass fiber (20 mass%) and CaCO$_3$ filler (47.1 mass%) and only ~28 mass% polymer, the Navier-Stokes equations are simplified as an incompressible

Newtonian fluid with negligible gravitational effects eq.(8.7):

$$\delta P/\delta z = \eta(\delta^2 v_z/\delta x^2 + \delta^2 v_z/\delta y^2) \qquad (8.8)$$

where the velocity profile for laminar flow is approximated as the 3-D elliptical paraboloid:

$$v_z = U_{c,calc}[1 - (2x/th)^2 - (2y/w)^2] \qquad (8.9)$$

where $U_{c,calc}$ is 0.194 ms^{-1}. Substituting eq. (8.9) into eq. (8.8) 2nd order implicit differentiation yields:

$$\delta P/\delta z = 8\eta U_{c,calc}[(1/th)^2 + (1/w)^2] \qquad (8.10)$$

The pressure drop across the three sections, 'A', 'B' and 'C' therefore is the sum:

$$(\delta P/\delta z)_{tot} = \Sigma_k(\delta P/\delta z)_k \quad (k \text{ goes from A to C}) \qquad (8.11)$$

Rearranging, we obtain effective viscosity, η_{eff} as a function of injection pressure in eq. (8.12):

$$\eta_{eff} = (\delta P/\delta z)_{tot}/8\{2U_{c,A}[(1/th_A)^2+(1/w_A)^2] + U_{c,B}[(1/th_B)^2+(1/w_B)^2]\} \qquad (8.12)$$

where $U_{c,A} = U_{c,C} = 0.126$ ms^{-1}, $U_{c,B} = 0.194$ ms^{-1}, and δz = total specimen length, L (0.220 m). The plot in Figure 8.9 shows the relation yielding effective viscosity range at mold walls estimated as $47.6 < \eta_{eff} < 93.9$ Pas ($\eta_{eff,(avg)} = 70.8$ Pas) that must be overcome by the $3.5 < \delta P < 6.9$ MPa injection pressures. Exceeding the polyester melt viscosity of ~2 Pas, this seems a decent approximation since additives of shrinkage control, cross-linking, thickening, and mold release agents, with pigment and filler all play a role in increasing viscosity above the polymer melt.

8.2.7 Comparison of effective viscosity, η_{eff} calculation with experimental viscosity measurements
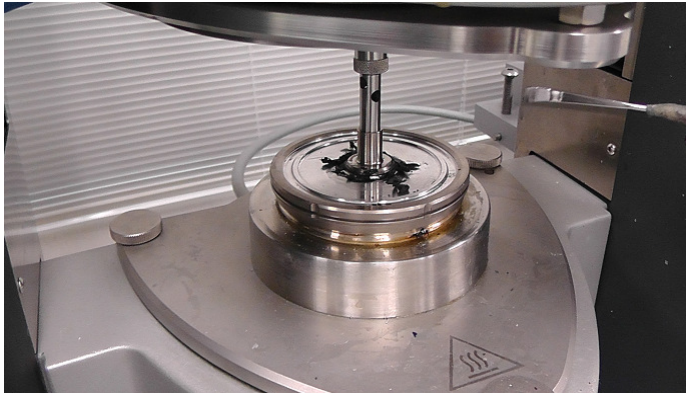
Fig. 8.10 BMC paste sample without the E-glass fibers or CaCO$_3$ filler in parallel plate viscometer holder. The paste is black due to the pigment.

133

Figure 8.10 shows the parallel plate viscometer with the BMC paste without the E-glass fibers or $CaCO_3$ filler. Viscosity measurements of the paste without the E-glass fibers or $CaCO_3$ filler appeared to agree remarkably with the calculation of viscosity of paste at the mold walls by the Navier-Stokes calculation (Figure 8.11, solid lines). This is picturing the BMC paste as forming a thin melt layer with lower viscosity within δ_f at the mold walls assisting to push the fiber and filler-containing ultra-high viscosity core into the mold. The experimental hysteresis curves at temperatures of 20, 60 and 100°C all fall within the calculated viscosity (η_{eff}) range of 48 to 94 Pas (solid lines). The paste displayed shear-thinning behavior where viscosity decreased with increasing shear rate. There is hysteresis where viscosity was reduced as the shear rate was ramped down again. Hysteresis was probably brought about by despite the paste having no glass fibers or $CaCO_3$ filler, other solid particles present along with the polymers such as carbon black pigment, calcium stearate, aluminum silicate and magnesium oxide were reduced by the continued friction of the parallel plate rheometer disc movement during the shear rate ramp down cycle. This behavior is known as thixotropic displaying a decrease in viscosity with time.
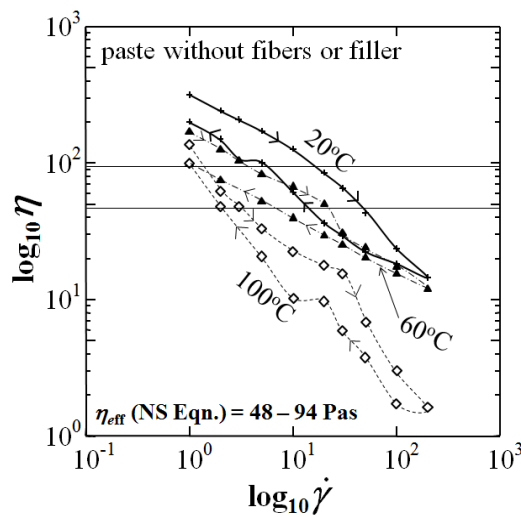
Fig. 8.11 Experimental viscosity measurement data of the BMC paste without fibers or filler compared with calculation of viscosity range of melt at mold walls, η_{eff} (Fig. 8.9) by Navier-Stokes equation (solid lines).
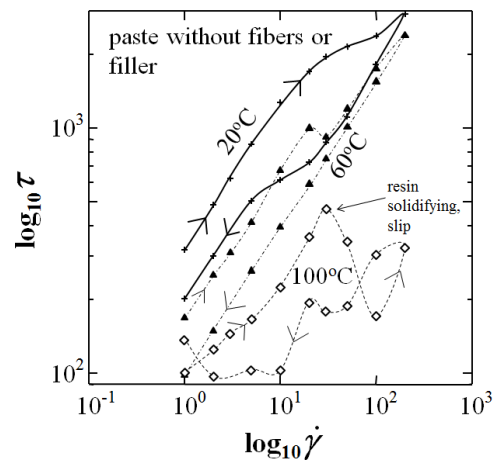
Fig. 8.12 Experimental values of logarithm of shear stress, τ (Pa) vs. shear rate, $\dot{\gamma}$ (s⁻¹) of the BMC paste without glass fibers or filler

Fig. 8.12 shows the corresponding logarithm of shear stress, τ (Pa) vs. shear rate, $\dot{\gamma}$ (s⁻¹) of the BMC paste without fibers or filler. The 20 and 60°C curves show good contact between the parallel plates and paste as evidenced by the increase in τ with $\dot{\gamma}$ indicating reliable data. At 100°C the shear stress decreased above $\dot{\gamma} = 30$s⁻¹ during the increasing $\dot{\gamma}$ cycle probably due to solidification that had occurred in the resin, hence higher temperatures 140° and 170°C were not tested. Nevertheless, the viscosities of the increasing $\dot{\gamma}$ at low shear rate in Fig. 8.12 fell within the calculated Navier-Stokes range (box) in Fig. 8.11.

8.2.8 Viscosity measurements of GFRP [paste + fibers + filler]
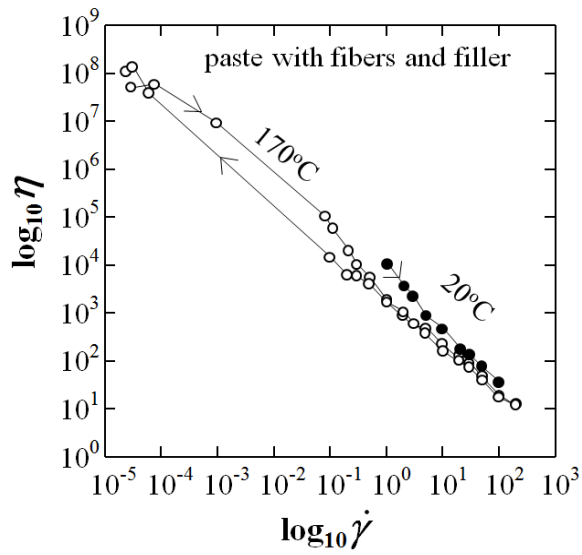
Fig. 8.13 Experimental values of logarithm of viscosity, η (Pas) vs. shear rate, $\dot{\gamma}$ (s^{-1}) of the BMC-GFRP paste with glass fibers and filler.
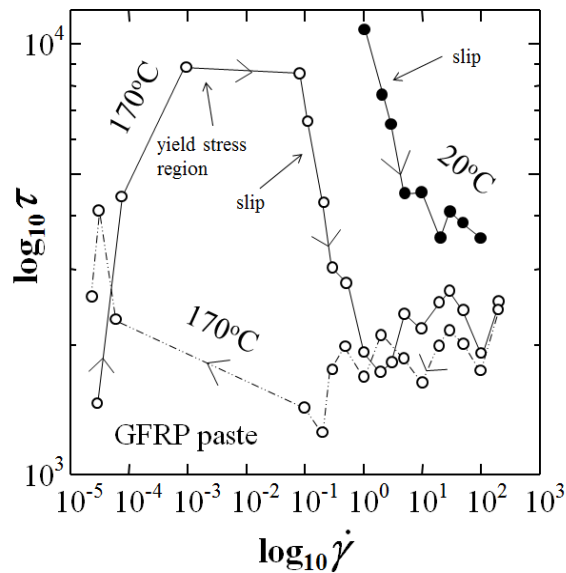
Fig. 8.14 Experimental values of logarithm of viscosity, η (Pas) vs. shear rate, $\dot{\gamma}$ (s^{-1}) of the BMC-GFRP paste with glass fibers and filler. There was apparently slip between the metal disc and the GFRP paste indicated by the decreasing τ.

Fig. 8.13 shows experimental values of logarithm of viscosity, η (Pas) vs. shear rate, $\dot{\gamma}$ (s^{-1}) of the BMC paste with glass fibers and filler showed nearly equal values at 20° and 170°C, but there was slip observed at both temperatures between the metal disc and the GFRP samples due to glass fiber and high filler content. Slip was observed as a flat, buffed surface. The sample at 170°C (above the molding temperature at 163°C) was solidified probably due to crosslinking. Fig. 8.14 shows the 170°C sample exhibited a yield point at $\log_{10} \dot{\gamma} = 10^{-3}$ and was observed to solidify at some point ($\log_{10} \dot{\gamma} > \sim 10^{-1}$) at 170°C. It is recommended to use parallel plate viscometer with serrated plates for the GFRP paste containing fibers and filler, however the Navier-Stokes calculation agreed well with the viscosity values for the paste without fibers or filler.

8.2.8 Hydraulic Head Pressure Loss and Entrance Length

Since the present definitions of hydraulic head pressure loss, P_{loss}, and entrance length, L_e are functions of the friction factor, f [8.8] which depends primarily on the flow conditions at the duct walls, $\eta_{eff} = 70.8$ Pas is used. P_{loss} of the paste entering section 'A' at the gate can be calculated by the Darcy-Weisbach equation valid for duct flows of any cross section for laminar and turbulent flow [8.3]:

$$P_{loss} = f(L/D_H)(\rho U_b^2/2) \tag{8.13}$$

where ρ is density of the paste. Friction coefficient for laminar flow calculated by $f=64/Re$ [8.3, 8.9, 8.10] is 5420 hence, P_{loss} is 1.32 MPa. Thus, P_{loss} is calculated to be 19-38% of the 3.50–6.90 MPa injection mold pressure.

In addition, entrance length at which the boundary layer stabilizes, L_e for laminar flow is [8.3, 8.9, 8.10]:

$$L_e/D_H = 0.06Re \tag{8.14}$$

Using this equation with $\eta_{eff} = 70.8$ Pas, L_e is calculated to be only 0.0054 mm for entering either sections 'A' or 'B' (Fig. 8.5), (0.002-0.005% of length) indicating primary boundary layer, $\delta_{0.99Uc}$ and flow is approximately constant and stable throughout the entire 210 mm length. This calculation indicates a steady-state flow condition of the fibers probably contributing to the excellent flow characteristics of BMCs that make them well-suited for injection-molded parts requiring precise dimensions and detail.

8.3 Conclusions

1) To investigate the feasibility of processing using the short-fiber 0.44 mm GFRP-BMC paste in the factory, velocity profile and rheological parameters in the injection-molded sample has been investigated by means of fiber orientation mapping by SEM. A smooth laminar parabolic flow was observed indicating the shortened 0.44 mm fiber paste can be beneficial to industry.

2) Experimental viscosity data of the BMC paste without fibers or filler using a parallel plate viscometer agreed with calculated value of viscosity of melt layer at mold walls from the Navier-Stokes equation.

3) Velocity profile of highly-filled GFRP-BMC exhibited laminar creep flow through rectangular duct-shaped specimen during injection molding from SEM fiber orientation mapping. Primary and secondary boundary layer values for flow and fiber orientation, respectively were obtained. To our knowledge there is no or little research on estimating velocity profile from fiber orientation mapping of GFRP-BMCs.

4) The fiber mapping could possibly be used as an additional evaluation to obtain a rough or better estimation of actual flow patterns and velocities to later simulate or optimize entire molding process by computer simulation.

REFERENCES

[8.1] Thomason J., Composites **A 39** (2008) 1732-1738.

[8.2] Faudree M. and Nishi Y., Mater. Trans. **54** (2013) 1877-1883.

[8.3] Hieberand C. and Shen S., J. Non-Newtonian Fluid Mech. **7** (1982) 1–32.

[8.4] Anselmet F., Ternat F., Amielh M., Boiron O., Boyer P. and Pietri L., C.R.Mecanique **337** (2009) 573-584.

[8.5] Akay M. and Barkley D., J .Mater. Sci. **26** (1991) 2731-2742.

[8.6] VerWeyst B., Tucker C. III, Foss P. and O'Gara J., Intl. Polym. Proc. **4** (1999) 409-420.

[8.7] Martys N., George W., Chun B. and Lootens D., Rheol. Acta. **49** (2010) 1059-1069.

[8.8] du Plessis J., and Collins M., N and O Rheo. **9** (1992) 11-16.

[8.9] Schlichting H., *Boundary Layer Theory*, 7th Edition (New York: McGraw-Hill, 1979).

[8.10] White F., *Viscous Fluid Flow*, 2nd Edition (New York: McGraw-Hill, 1991).

Chapter 9 Conclusions

In summary, a new strengthening method in short glass fiber reinforced polymer composites has been developed. In discontinuous short-fiber reinforced polymer composites GFRPs and CFRPs (glass and carbon fiber reinforced polymer) composites most data for unfilled FRP reports increasing fiber length increases tensile properties. However, in a highly-filled GFRP-BMC (bulk molding compound) it has been found that decreasing fiber length to sub-millimeter can significantly increase fracture strength, strain and impact strength. Novel 'fiber end crazing' and 'fiber spacing' models for increasing tensile fracture stress and modulus as fiber length is decreased are constructed. The 'fiber end crazing' model is based on crazing in the form of whitening observed at fiber ends and incoherent interface during tensile deformation halting microcracks increasing fracture stress and its strain ~60 and ~40%, respectively. The 'fiber spacing' model is constructed for early strains on the basis that the increased spacing between fibers acts as thermal residual compressive stress sites by difference in coefficient of thermal expansion (CTE) between fiber and matrix increasing the tensile modulus. The 3-phase BMC (polymer-fiber-filler) behaves much like some ceramics or metal-matrix composites (MMCs) where strength is remarkably increased by decreasing particle size. To make this dissertation well-rounded additional successful strengthening methods including increasing texture angle and applying low-voltage electron beam irradiation to the SGFRP-BMC are also presented.

Summary

Chapter 1 gives a brief history, background, and definitions for improving mechanical properties of highly-filled GFRP-BMCs. Included is an overview of enhance mechanical properties of composite materials: particle size, homogeneous low-voltage electron beam irradiation (HLEBI), and effect of texture angle and how they apply to the 3-phase BMC.

Chapter 2 covers the experimental procedure. To obtain shortened fiber samples, the BMC paste was mixed for an additional 30 min prior to molding.

Chapter 3 focuses on compression molded samples, increasing solidification texture angle from 7.5 to 68 deg increased statistically lowest Charpy impact value a_s at lowest fracture probability (P_f = 0) a remarkable 101%. Charpy impact values (a_{uc}) at mid-fracture probability, (P_f = 0.50) were increased 35 to 50%.

Chapter 4 focuses on applying 0.86 MGy homogeneous low voltage electron beam irradiation (HLEBI) to the typically weak center of the compression molded panels apparently enhances the Charpy impact values (a_{uc}) 5 to 25%. Applying 0.30 MGy HLEBI to the outer diagonal texture angles of 45 deg increased the a_s at lowest fracture probability (P_f = 0) a remarkable 64%. Electron spin resonance (ESR) revealed an increase in unpaired electrons, which were probably dangling bonds producing compressive stress sites.

Chapter 5 focuses on shortening fibers by 30 min extended mix from commercial nominal 6 mm to sub-millimeter in the compression molded panels apparently enhances the Charpy impact strength (a_{uc}) ~30% at all texture angles in the mother panels.

Chapter 6 focuses on injection molded specimens shortening fibers to sub-millimeter increased tensile modulus 5 to 25% in the highly-filled injection-molded GFRP-BMC. Up to now, this result has not been reported in the literature: most data for unfilled FRP reports increasing fiber length increases tensile modulus by 'shear lag' mechanism. A novel 'fiber spacing' model is constructed which predicts effect of fiber length (l_f), diameter (d), fiber volume fraction (V_f), filled-matrix (E_m) and fiber (E_f) materials on tensile modulus ($d\sigma/d\varepsilon$)$_o$ to be useful in BMC composite design. The model is based on increased number of spaces, S_f between fibers as fiber length is shortened appearing to allow for action of an order of magnitude difference in coefficient of thermal expansion (CTE) difference between fibers and matrix increasing thermal compressive residual

stress sites by the matrix on the fibers during shrink and cool-down.

Chapter 7 focuses on the most important finding of this dissertation for injection molded specimens that shortening fibers (rather than lengthening) in FRP from commercial 6.4 mm to submillimeter 0.44 mm significantly increased tensile strength, σ_f (~60%) and its strain, ε_f (~40%) of the highly-filled injection-molded GFRP-BMC. Up to now, this result has not been reported in the literature: most data for unfilled FRP reports increasing fiber length increases fracture stress. A novel "fiber end crazing' model is constructed that has not been previously reported in the literature. It is based on SEM observations that showed crazing at the fiber ends appearing as whitening and coherent interface in the 0.44 mm samples. The crazing appears to be the dominant mechanism for strengthening by generating compressive stress sites in the matrix halting microcracks below their critical length $2a_c$.

Chapter 8 focuses on investigating the feasibility of processing using the short-fiber 0.44 mm GFRP-BMC paste in the factory. Velocity profile and rheological parameters in the injection-molded sample has been explored by means of fiber orientation mapping by SEM agreeing closely with Navier-Stokes calculations and viscosity measurement data illustrating feasibility by the smooth flow of the BMC paste.

Acknowledgements

学位論文要旨 : **Development of a New Strengthening Method in Short Glass Fiber Reinforced Polymer Composites** /短繊維強化高分子複合体の強靭化に関する研究

Michael C. Faudree

　世界市場で流通しており、E ガラスの短繊維、熱硬化性ポリエステル/スチレン-ブタジエン、そして炭酸カルシウム充填材を含む 3 相で構成する、射出圧縮成形したガラス繊維強化高分子(GFRP)バルク成型コンパウンド(BMCs)複合材料（GFRP-BMC）の強靭化を研究し、短尺繊維分散強化機構を見出した。

　本研究の最初の成果は集合組織短繊維配向角度の増加にともない GFRP-BMC の衝撃値が改良されることを見出し、第三章に記述した。次に、均一な低エネルギー電子線照射(HLEBI)処理が、GFRP-BMC の衝撃値をさらに向上させることを見出し、第四章に記述した。三番目は、添加する繊維の長さを、サブミリメートルまでの短尺化することにより、GFRP-BMC の衝撃値、引張変形抵抗率(弾性係数)、破壊強度(引張強度)と、破壊歪の向上を見出したことであり、第五、六、七章で記述した。これは、破壊靭性値から計算出来る臨界クラック長より短い 0.44mm 長さの極短尺繊維の分散と、各繊維端で発生する圧縮応力の増加により説明でき、高分子複合材料において初めて公表された、本研究の最大の成果である、短尺繊維分散強化機構を提案した。四番目は射出成型した混合流体の数値シミュレーションを行った。GFRP-BMCの極短尺繊維配向集合組織のSEM断面画像は、3 層(表皮-心-表皮)構造を示し、この計算と実験結果に良い相関関係を見出し、機械的性質の再現性を高めるための製造条件に関する基礎的知見を得て、第八章に記述した。

　第一章は序論で、研究背景から始め、寸法精度、難燃性、高絶縁性、耐食性、色彩安定性に合わせて成分配合を最適化した GFRP-BMC に関する概観を紹介し、本研究の目的を述べた。

　第二章は、GFRP-BMC 試料の作製と評価方法、それらの条件を中心に述べた。試料の作製は、精密な寸法と円滑な表面仕上げで大量生産に用いられている射出圧縮成形を用いた。

　第三章は、試料切り出し前のマザーパネル中央部は、配向角度がランダム分布の凝固組織であり、外縁部よりパネル中央のシャルピー衝撃値(a_{uc})は著しく低い。そこで、短繊維の配向角度が異なる4種類の集合組織に分類したところ、GFRP-BMC試料の配向角度が高いと衝撃値を高めることを見出した。さらに、これを三母数ワイブル関数で計算し、下限衝撃値(a_s)を求めた。Fig.1 に示すように、短繊維配向角度が 17.5°の試料に比較し、配向角度 68°の試料は、101%向上した。その結果、短繊維の配向角度が高い集合組織試料は、衝撃破壊抵抗が高いことを見出した。なお、70℃ と-79℃ での衝撃値を調べたら、室温より高く、航空機体材料として実用的であることも見出した。

　第四章は電子線照射(HLEBI)によるGFRP-BMC試料の衝撃値の向上について述べた。マザーパネル中央部は、外縁部より衝撃値が著しく低いが、中央部にHLEBI処理すると、5から25%程、a_{uc}を高めることを見出した。さらに、Fig.2に示すように、0.3MGy照射した45°配向集合組織試料のa_sは、未照射試料よりも約64%向上することを見出した。ESRの結果からHLEBIが高分子中の共有結合を切断することで、高分子内にダングリングボンドを伴う終端原子を生成させ、圧縮サイトが形成することが主な強化機構である。さらに、高い衝撃値の試料では、単純な破壊から、2次マイクロクラックの増殖や、主クラック付近の複雑な破壊機構への変換も、衝撃値向上の効果となる。

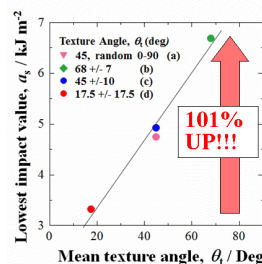　第五章は、繊維の短尺化もGFRP-BMCの衝撃値(a_{uc})向上させることを述べた(Fig.3参照)。

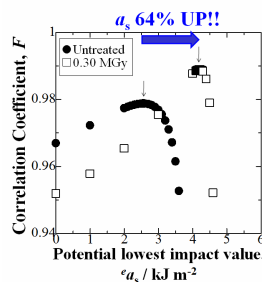**Fig.1 Changes in the lowest impact value (a_s) against mean texture angle.**

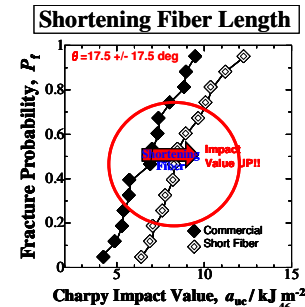**Fig.2 Changes in correlation coefficient against the potential lowest impact value.**

Fig.3 Changes in the Charpy impact value (a_{uc}) against fracture probability.

第六章において GFRP-BMC の弾性率の機構を説明した。この複合材料の弾性率は、ポリエステル単独で2GPa、$CaCO_3$ 微粉末添加複合化で 4.5GPa まで向上し、市場化している 6.4 mm 長さの繊維による強化で 6.5GPa まで増加する。さらに、繊維長を 0.44 mm まで短尺化すると 8 GPa まで付加的に向上することを見出した。Fig. 4 の応力―歪曲線から弾性率の指標となる変形抵抗率を求めた。この繊維長さの短尺化は、GFRP-BMC の初期変形抵抗率を 27%、最大変形抵抗率を 22%向上させた(Fig.5 参照)。これは、母材のポリエステル樹脂の熱膨張係数(CTE)が、E ガラスのそれより約 1 桁大きい為、成型凝固冷却時に繊維間隙の母材中に圧縮残留応力が生じ、母材分子密度が増大する。さらに、繊維短尺化による繊維/母材界面の面積増加が積算され、変形抵抗率向上が説明できる。

第七章は、繊維長さの短尺化により、GFRP-BMC の引張破壊強度(σ_f;Fig.6 参照)と、引張破壊歪(ε_f;Fig.7 参照)の増加を見出した。0.44 mm 長の極短尺繊維を用いた GFRP-BMC の σ_f と ε_f は、6.4mm 長の繊維試料と比べても、約 60 と 40%程度高めた。この短尺化は繊維端密度を高め、変形の際に繊維端における繊維/母材界面近傍における crazing 密度が増加する。crazing 領域はクラック伝播を抑制する圧縮場を保持する微小塑性変形と、臨界クラック長さ($0.50 < 2a_c < 5.0$ mm)以下の微小クラックを内在する(Fig.8 参照)。さらに、主クラック先端近傍で応力集中を抑制するマイクロクラックが SEM 観察や超音波吸収(Fig.9参照)の測定結果を用いて考察した。これらが破壊エネルギーを吸収することにより、マイクロクラックタフニング機構を発現する。臨界クラック長さ、繊維端の圧縮応力領域、マイクロクラックタフニング、繊維の引抜き緩和効果の全てがクラック伝播を抑制し、GFRP-BMCの破壊歪の増加に寄与する可能性が高い。さらに、前章の変形抵抗率の増大も考慮すると、引張破壊強度向上や第五章の衝撃値向上も説明できる。

第八章は、極短尺繊維、熱硬化性ポリエステル/スチレン-ブタジエン、炭酸カルシウム充填材の混合流体の射出成型時の数値シュミレーションを行った。繊維集合組織の SEM 断面画像は、表皮-心-表皮の三層構造を示すが、この実験と計算結果に良い相関を見出した。
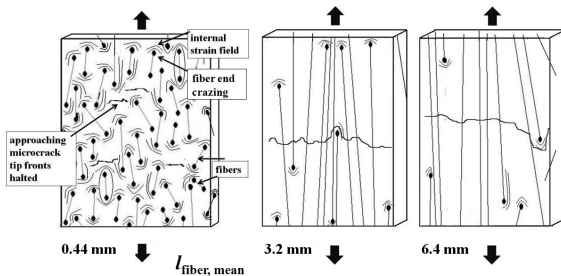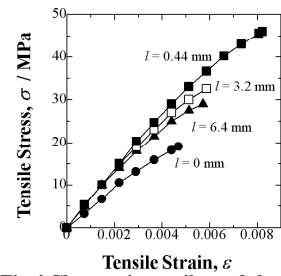
第九章は総括である。

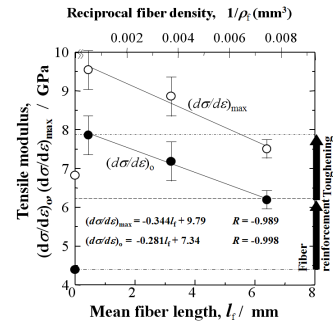Fig.4 Changes in tensile modulus against mean fiber length.

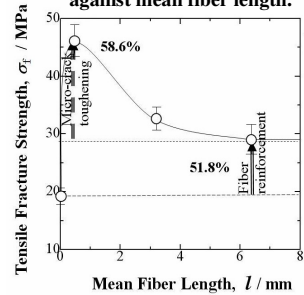Fig.5 Changes in tensile modulus against mean fiber length.

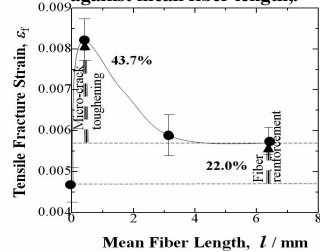Fig. 6 Change in tensile strength against mean fiber length,.

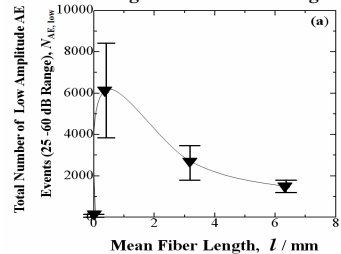Fig. 7 Change in fracture strain against mean fiber length.

Fig. 9 Number of AE events in the low amplitude range from 25-60 dB, emitted by the BMC during the entire tensile

Fig.8 Three-dimensional schematic showing higher fiber end density, ρ_{EE}(mm^{-3}) in the 0.44 mm samples initiating compressive stress sites, which absorb energy approaching crack tip fronts halting the cracks.